POLITECNICO DI TORINO
Repository ISTITUZIONALE

Two-particle differential transverse momentum and number density correlations in p- Pb collisions at 5.02 TeV and Pb-Pb collisions at 2.76 TeV at the CERN Large Hadron Collider

Original
Two-particle differential transverse momentum and number density correlations in p- Pb collisions at 5.02 TeV and Pb-Pb collisions at 2.76 TeV at the CERN Large Hadron Collider / Acharya, S., Adamova, D., Adolfson, J., Aggarwal, M., Rinella, G., Agnello, M., Agrawal, N., Bufalino, S., Catalano, F., Concas, M., Grosa, F., Fecchio, P., Ravasenga, I.. - In: PHYSICAL REVIEW C. - ISSN 2469-9985. - STAMPA. - 100:4(2019), p. 044903. [10.1103/PhysRevC.100.044903]

Availability:
This version is available at: 11583/2847964 since: 2020-10-08T19:34:53Z

Publisher:
American Physical Society

Published
DOI:10.1103/PhysRevC.100.044903

Terms of use:

This article is made available under terms and conditions as specified in the corresponding bibliographic description in the repository

Publisher copyright

(Article begins on next page)

25 November 2026

Two-particle differential transverse momentum and number density correlations in *p*-Pb collisions at 5.02 TeV and Pb-Pb collisions at 2.76 TeV at the CERN Large Hadron Collider

S. Acharya *et al.**
(ALICE Collaboration)

(Received 23 May 2018; revised manuscript received 15 January 2019; published 10 October 2019)

We present measurements of two-particle differential number correlation functions R_2 and transverse momentum correlation functions P_2, obtained from *p*-Pb collisions at 5.02 TeV and Pb-Pb collisions at 2.76 TeV. The results are obtained by using charged particles in the pseudorapidity range $|\eta| < 1.0$ and transverse momentum range $0.2 < p_{\mathrm{T}} < 2.0$ GeV/c as a function of pair separation in pseudorapidity, $|\Delta\eta|$, azimuthal angle $\Delta\varphi$, and for several charged-particle multiplicity classes. Measurements are carried out for like-sign and unlike-sign charged-particle pairs separately and combined to obtain charge-independent and charge-dependent correlation functions. We study the evolution of the width of the near-side peak of these correlation functions with collision centrality. Additionally, we study Fourier decompositions of the correlators in $\Delta\varphi$ as a function of pair separation $|\Delta\eta|$. Significant differences in the dependence of their harmonic coefficients on multiplicity classes are found. These differences can be exploited, in theoretical models, to obtain further insight into charged-particle production and transport in heavy-ion collisions. Moreover, an upper limit of nonflow contributions to flow coefficients v_n measured in Pb-Pb collisions based on the relative strength of Fourier coefficients measured in *p*-Pb interactions is estimated.

DOI: 10.1103/PhysRevC.100.044903

I. INTRODUCTION

Measurements carried out at the Relativistic Heavy Ion Collider (RHIC) and the Large Hadron Collider (LHC) during the last decade indicate that a strongly interacting quark-gluon plasma (sQGP) is produced in heavy nuclei collisions at high beam energies [1–4]. In particular, observations of strong elliptic flow and theoretical studies based on relativistic hydrodynamics indicate that this matter behaves as a very low specific shear viscosity (shear viscosity over entropy-density ratio) fluid [5–8]. Additionally, the observed suppression of high-transverse-momentum (p_{T}) single-hadron production as well as dihadron correlations, in heavy-ion collisions, compared with elementary *pp* interactions, showed that the produced matter is rather opaque [9–19]. Furthermore, studies of two- and multiparticle correlation functions unravelled several unanticipated correlation features [11,20–26], including a near-side correlation peak (i.e., the prominent and relatively narrow peak centered at $\Delta\varphi = 0$, $|\Delta\eta| = 0$ observed in two-particle correlation functions) broadening, the appearance of a near-side elongated ridge in relative pseudorapidity, as well as a strong suppression or modification of the away-side correlation peak relative to the one observed in *pp* collisions [10,27,28]. Extensive studies were carried out, both at RHIC and LHC energies, to fully characterize and understand the underlying causes of these features. Significant progress was achieved with the realization that fluctuations in the initial spatial configuration of colliding nuclei can greatly influence the measured correlations, most particularly the development of odd and higher harmonics in the azimuthal particle distributions (anisotropic flow) [29]. However, a quantitative assessment of the magnitude and impact of nonflow effects on measured correlations requires further investigations. Nonflow effects may arise from resonance decays or low-multiplicity hadronization processes associated with mini-jets, string fragmentation, or color tube breakup [30–34]. However, it remains unclear how these different particle-production mechanisms influence the shape and strength of correlation functions and what their relative contributions might be. It is also unclear how the surrounding environment associated with these processes can alter two- and multiparticle correlation functions. In an effort to shed light on some of these questions, we consider additional observables and types of correlation functions.

In this work, we present measurements of R_2, a differential two-particle number correlation function and a differential transverse-momentum correlation function, defined below, and identified as P_2 [35]. The two correlation functions are studied in *p*-Pb collisions at $\sqrt{s_{\mathrm{NN}}} = 5.02$ TeV and Pb-Pb collisions at $\sqrt{s_{\mathrm{NN}}} = 2.76$ TeV as a function of charged-particle pair relative pseudorapidity $\Delta\eta$ and relative azimuthal angle $\Delta\varphi$, as well as produced charged-particle multiplicity (corresponding to collision centrality in Pb-Pb). The observable P_2 features an explicit dependence on the transverse momentum of the produced particles that provides sensitivity to the correlation "hardness," i.e., how low- and high-momentum

*Full author list given at the end of the article.

Published by the American Physical Society under the terms of the Creative Commons Attribution 4.0 International license. Further distribution of this work must maintain attribution to the author(s) and the published article's title, journal citation, and DOI.

 ©2019 CERN, for the ALICE Collaboration

particles contribute to the correlation dynamics. Combined measurements of number and transverse momentum correlations provide further insight into mechanisms of particle production and transport in nucleus-nucleus collisions. The measurements presented in this work thus provide additional quantitative constraints on existing models of collision dynamics used towards the characterization of the matter produced in high-energy nucleus-nucleus collisions.

The R_2 and P_2 correlation functions are first reported independently for like-sign (LS) and unlike-sign (US) particles given that they feature distinct dependencies on particle-production mechanisms. In particular, US pair correlations are expected to be rather sensitive to neutral resonances decays. The US and LS correlations are then combined to obtain charge-independent (CI) and charge-dependent (CD) correlation functions, defined in Sec. II. At high collisional energy, one expects energy-momentum conservation to play a similar role in US and LS correlations. The CD correlations obtained by subtracting LS from US correlations are then largely driven by charge conservation. Comparison of LS, US, CI, and CD correlations thus enables a detailed characterization of the particle-production and -transport processes involved in heavy-ion collisions. The study of CD correlations, in particular, shall then provide strong constraints on particle-production models.

To obtain a detailed characterization of the R_2 and P_2 correlation functions, their shape is studied as a function of collision centrality and pair separation in pseudorapidity. The width of the correlation functions, most particularly their charge-dependent components $R_2^{(\mathrm{CD})}$ and $P_2^{(\mathrm{CD})}$, are sensitive to charged-particle creation mechanisms and time of origin [36–39], momentum conservation [40–42], as well as transport phenomena such as radial flow [43–45] and diffusion processes [46–49]. We report the longitudinal (pseudorapidity) and azimuthal widths of the near-side peaks of the R_2 and P_2 correlators as a function of charged-particle multiplicity and longitudinal (pseudorapidity) pair separation. Fourier decompositions are studied as a function of pseudorapidity pair separation to obtain a detailed characterization of flow and nonflow contributions to these correlation functions.

This paper is organized as follows: Section II presents the definition of the observables R_2 and P_2 and briefly discusses their properties. In Sec. III, the experimental setup and experimental methods used to acquire and analyze the data are discussed, while the methodology used to measure the R_2 and P_2 observables is described in Sec. IV. Systematic effects are considered in Sec. V. Measurements of the R_2 and P_2 correlation functions are reported in Sec. VI. Results are discussed in Sec. VII and summarized in Sec. VIII.

II. OBSERVABLES DEFINITION

Single-and two-particle invariant cross sections integrated over the p_{T} range of interest are represented as

$$\rho_1(\eta,\varphi) = \frac{1}{\sigma_1}\frac{d^2\sigma_1}{d\eta d\varphi},$$
$$\rho_2(\eta_1,\varphi_1,\eta_2,\varphi_2) = \frac{1}{\sigma_2}\frac{d^4\sigma_2}{d\eta_1 d\varphi_1 d\eta_2 d\varphi_2}, \tag{1}$$

where ρ_1 and ρ_2 represent single- and two-particle densities, σ_1 and σ_2 represent single- and two-particle cross sections, and η and φ represent the pseudorapidity and azimuthal angle of produced particles.

Two-particle correlations are determined based on normalized cumulants defined according to

$$R_2(\varphi_1,\eta_1,\varphi_2,\eta_2) = \frac{\rho_2(\varphi_1,\eta_1,\varphi_2,\eta_2)}{\rho_1(\varphi_1,\eta_1)\rho_1(\varphi_2,\eta_2)} - 1. \tag{2}$$

Given that the primary interest lies in the correlation strength as a function of pair separation, one integrates over all coordinates taking into account experimental acceptance to obtain the correlation functions $R_2(\Delta\varphi,\Delta\eta)$ according to

$$R_2(\Delta\varphi,\Delta\eta) = \frac{1}{\Omega(\Delta\eta)}\int d\varphi_1 d\varphi_2 d\bar{\varphi}\,\delta(\Delta\varphi-\varphi_1+\varphi_2)\delta(\bar{\varphi} - 0.5(\varphi_1+\varphi_2))\int d\eta_1 d\eta_2 d\bar{\eta}\,\delta(\Delta\eta-\eta_1+\eta_2)\delta(\bar{\eta}-0.5(\eta_1+\eta_2))R_2(\varphi_1,\eta_1,\varphi_2,\eta_2), \tag{3}$$

where the azimuthal angles φ_1 and φ_2 are measured in the range $[0,2\pi]$ whereas the pseudorapidities η_1, η_2 are measured in the range $[-1,1]$. The factor $\Omega(\Delta\eta)$ represents the width of the acceptance in $\bar{\eta} = (\eta_1+\eta_2)/2$ at a given $\Delta\eta = \eta_1-\eta_2$. The azimuthal-angle difference, $\Delta\varphi = \varphi_1-\varphi_2$, is shifted to fall within the range $[-\pi/2, 3\pi/2]$. The integration is carried out across all values of $\bar{\varphi} = (\varphi_1+\varphi_2)/2$.

Different observables can be defined which are sensitive to the correlation between the transverse momentum of produced particles. Integral correlations expressed in terms of inclusive and event-wise averages of the product $\Delta p_{\mathrm{T},i}\Delta p_{\mathrm{T},j}$ (where $\Delta p_{\mathrm{T},i} = p_{\mathrm{T},i} - \langle p_{\mathrm{T}}\rangle$) of particle pairs $i \neq j$ have been reported [35,50–54]. A generalization to differential correlation functions with dependencies on the relative azimuthal angles and pseudorapidities of particles is straightforward when expressed in terms of inclusive averages denoted $\langle \Delta p_{\mathrm{T}}\Delta p_{\mathrm{T}}\rangle$ [35]. In this study, measurements of transverse momentum correlations are reported in terms of a dimensionless correlation function P_2 defined as a ratio of the differential correlator $\langle \Delta p_{\mathrm{T}}\Delta p_{\mathrm{T}}\rangle$ to the square of the average transverse momentum:

$$P_2(\Delta\eta,\Delta\varphi) = \frac{\langle \Delta p_{\mathrm{T}}\Delta p_{\mathrm{T}}\rangle(\Delta\eta,\Delta\varphi)}{\langle p_{\mathrm{T}}\rangle^2} = \frac{1}{\langle p_{\mathrm{T}}\rangle^2}\frac{\int_{p_{\mathrm{T,min}}}^{p_{\mathrm{T,max}}}\rho_2(\mathbf{p}_1,\mathbf{p}_2)\Delta p_{\mathrm{T},1}\Delta p_{\mathrm{T},2}\,dp_{\mathrm{T},1}dp_{\mathrm{T},2}}{\int_{p_{\mathrm{T,min}}}^{p_{\mathrm{T,max}}}\rho_2(\mathbf{p}_1,\mathbf{p}_2)\,dp_{\mathrm{T},1}dp_{\mathrm{T},2}}, \tag{4}$$

where $\langle p_{\mathrm{T}}\rangle = \int \rho_1 p_{\mathrm{T}} dp_{\mathrm{T}} / \int \rho_1 dp_{\mathrm{T}}$ is the inclusive average momentum of produced particles in an event ensemble. Technically, in this analysis, integrals of the numerator and denominator of the above expression are first evaluated in four-dimensional space as functions of η_1, φ_1, η_2, and φ_2. The ratio is calculated and subsequently averaged over all coordinates, similarly as for R_2, as discussed above. For the sake of simplicity, the inclusive momentum $\langle p_{\mathrm{T}}\rangle$ is considered independent of the particle's pseudorapidity. This approximation is justified by the limited pseudorapidity range of this analysis

and by prior observations of the approximate invariance of $\langle p_{\mathrm{T}} \rangle$ in the central rapidity ($\eta \approx 0$) region [55].

By construction, P_2 is a measure of two-particle transverse momentum correlations: it is positive whenever particle pairs emitted at specific azimuthal angle and pseudorapidity differences are more likely to both have transverse momenta higher (or lower) than the p_{T} average, and negative when a high-p_{T} particle ($p_{\mathrm{T}} > \langle p_{\mathrm{T}} \rangle$) is more likely to be accompanied by a low-p_{T} particle ($p_{\mathrm{T}} < \langle p_{\mathrm{T}} \rangle$). For instance, particles emitted within a jet typically have higher p_{T} than the inclusive average. Jet particles therefore contribute a large positive value to P_2. Hanbury-Brown–Twiss (HBT) correlations, determined by pairs of identical particles with $p_{\mathrm{T},1} \approx p_{\mathrm{T},2}$ likewise contribute positively to this correlator. However, bulk correlations involving a mix of low- and high-momentum correlated particles can contribute both positively and negatively.

The R_2 and P_2 correlation functions reported in this work are determined for unidentified charged-particle pairs in the range $0.2 < p_{\mathrm{T}} < 2.0$ GeV/c and are considered as untriggered correlation functions. Differential correlation functions offer multiple advantages over integral correlations because they provide more detailed information on the particle correlation structure and kinematical dependencies. They can also be corrected for instrumental effects more reliably than measurements of integral correlations. Such corrections for instrumental effects on R_2 and P_2 correlation functions are discussed in Sec. IV.

The LS and US correlation functions are additionally combined to obtain charge-independent (CI) and charge-dependent (CD) correlation functions defined according to

$$O^{(\mathrm{CI})} = \tfrac{1}{2}(O^{(\mathrm{US})} + O^{(\mathrm{LS})}) = \tfrac{1}{4}(O^{(+,-)} + O^{(-,+)} + O^{(+,+)} + O^{(-,-)}), \quad (5)$$

$$O^{(\mathrm{CD})} = \tfrac{1}{2}(O^{(\mathrm{US})} - O^{(\mathrm{LS})}) = \tfrac{1}{4}(O^{(+,-)} + O^{(-,+)} - O^{(+,+)} - O^{(-,-)}), \quad (6)$$

where O represents either of the observables R_2 and P_2.

Charge-independent correlators $O^{(\mathrm{CI})}$ measure the average correlation strength between all charged particles, whereas charge-dependent correlators $O^{(\mathrm{CD})}$ are sensitive to the difference between correlations of US particles and those of LS particles. At high collision energies, such as those achieved at the LHC, negatively and positively charged particles are produced in approximately equal quantities and are found to have very similar p_{T} spectra [56]. The impact of energy-momentum conservation on particle correlations is thus expected to be essentially the same for US and LS pairs. The $O^{(\mathrm{CD})}$ correlators consequently suppress the influence of energy-momentum conservation and provide particular sensitivity to unlike-sign charge pair creation and transport processes. The charge-dependent correlation function $R_2^{(\mathrm{CD})}$, in particular, should in fact feature similar sensitivity to charge pair $(+,-)$ creation as the charge balance function B defined according to

$$B(\Delta\eta) = \frac{1}{2}\left(\frac{\rho_2^{(+,-)} - \rho_2^{(+,+)}}{\rho_1^{(+)}} + \frac{\rho_2^{(-,+)} - \rho_2^{(-,-)}}{\rho_1^{(-)}}\right) \quad (7)$$

and proposed by Pratt *et al.* to investigate the evolution of quark production in heavy-ion collisions [36,37,57]. Several measurements and theoretical studies of the balance function have already been reported. The STAR experiment has measured balance functions in Au-Au, d-Au, and pp collisions at $\sqrt{s_{\mathrm{NN}}} = 130$ and 200 GeV [58–61]. More recently, the ALICE collaboration reported observations of a narrowing of the balance function with increasing produced charged-particle multiplicity (N_{ch}) in Pb-Pb collisions at $\sqrt{s_{\mathrm{NN}}} = 2.76$ TeV, as well as in p-Pb collisions at $\sqrt{s_{\mathrm{NN}}} = 5.02$ TeV, and pp collisions at $\sqrt{s_{\mathrm{NN}}} = 7$ TeV [62,63]. Measurements in Au-Au and Pb-Pb are in qualitative agreement with the scenario, proposed by Pratt *et al.* [36,37,57], of two-stage quark production in high-energy central heavy-ion collisions but observations of a narrowing of the balance function with increasing N_{ch} in p-Pb and pp put this simple interpretation into question. At RHIC, and even more at LHC energies, the number of positively and negatively charged particles produced in the range $|\eta| < 1.0$ are nearly equal. Hence, the observable R_2 and the balance function are thus related according to

$$R_2^{(\mathrm{CD})}(\Delta\eta) = \frac{B(\Delta\eta)}{\rho_1^{(+)} + \rho_1^{(-)}}. \quad (8)$$

This implies that the narrowing of the balance function observed in most-central collisions, relative to peripheral collisions, is matched by a reduction of the width of the charge-dependent correlation function $R_2^{(\mathrm{CD})}$. Additionally, given that the observables R_2 and P_2 are both dependent on integrals of the two-particle density $\rho_2(\vec{p}_1, \vec{p}_2)$, one might expect a similar longitudinal narrowing of P_2 with collision centrality. However, the explicit dependence of P_2s on the product $\Delta p_{\mathrm{T}} \Delta p_{\mathrm{T}}$ implies it might have a different sensitivity to the collision system's radial expansion (radial flow) relative to that of R_2. A comparison of the centrality dependence of the longitudinal widths of the R_2 and P_2 correlations may then provide additional insight into the system's evolution and particle production dynamics, as well as put new constraints on models designed to interpret the observed narrowing of the balance function and the near-side ridge [64].

III. ALICE DETECTOR AND DATA ANALYSIS

The analysis and results reported in this paper are based on data acquired with the ALICE detector [65] during the $\sqrt{s_{\mathrm{NN}}} = 2.76$ TeV Pb-Pb run in 2010 and the $\sqrt{s_{\mathrm{NN}}} = 5.02$ TeV p-Pb run in 2013. The reported correlation functions are measured for charged particles detected within the inner tracking system (ITS) [66] and the time projection chamber (TPC) [67]. The ITS and TPC are housed within a large solenoidal magnet producing a uniform longitudinal magnetic field of 0.5 T. Together they provide charged-particle track reconstruction and momentum determination with full coverage in azimuth and in the pseudorapidity range $|\eta| < 1.0$. Data were acquired with a minimum bias (MB) trigger primarily based on the V0 detector, which also served for Pb-Pb collision centrality and p-Pb multiplicity class selection. This detector consists of subsystems V0A and V0C which cover the pseudorapidity ranges $2.8 < \eta < 5.1$ and $-3.7 < \eta < -1.7$, respectively. Detailed descriptions of the

ALICE detector, its subsystems, and triggers, as well as their respective performance, were reported elsewhere [65,66,68–72].

The primary vertex of a collision is reconstructed based on charged-particle tracks measured with the ITS and TPC detectors. Events were included in this analysis if at least one accepted charged-particle track contributed to the primary vertex reconstruction and if they featured only one primary vertex. The primary vertex was furthermore required to be within ± 10 cm from the nominal interaction point along the beam direction to ensure a uniform η acceptance within the TPC. The fraction of pile-up events in the analysis sample is found to be negligible after applying dedicated pile-up-removal criteria [72]. Event filtering based on primary vertex selection criteria yielded samples of approximately 14×10^6 Pb-Pb events and 81×10^6 p-Pb events.

The centrality of Pb-Pb collisions is estimated from the total signal amplitude measured by the V0 detectors using a standard ALICE procedure [73,74]. Nine collision centrality classes corresponding to 0%–5% (most-central collisions), 5%–10%, 10%–20%, 20%–30%, up to 70%–80% fractions of the total cross section were used in the analysis. The most-peripheral collisions, with a fractional cross section >80%, are not included in this analysis to avoid issues encountered with limited collision vertex reconstruction and trigger efficiencies. The p-Pb data are similarly analyzed in terms of multiplicity classes. An ALICE analysis reported in Ref. [75] showed that in p-Pb collisions, the produced charged-particle multiplicity is only loosely related to the collision impact parameter. So while it is appropriate to analyze the data in terms of multiplicity classes based on their fractional cross sections, these classes cannot be considered a direct indicator of the impact parameter in those collisions. They are representative, nonetheless, of qualitative changes in the particle production. Our analysis goal is thus to identify and document changes and trends in the shape and strength of the R_2 and P_2 correlators as a function of these multiplicity classes.

The analysis was restricted to primary particles, i.e., particles produced by strong interactions. Contamination from secondary charged particles [i.e., particles originating from weak decays such as neutral kaons (K_S^0) and lambdas (Λ^0), conversions and secondary hadronic interactions in the detector material] is suppressed with track-selection criteria based on charged-tracks' distance of closest approach (DCA) to the primary interaction vertex of the collision. Only "bulk" charged-particle tracks measured in the transverse momentum range $0.2 < p_{\mathrm{T}} < 2.0$ GeV/c were selected. Particles in this momentum range constitute the dominant fraction of the produced particles and are believed to be primarily the product of nonperturbative interactions. They thus constitute the main focus of this work towards the characterization of the systems produced in p-Pb and Pb-Pb collisions.

To suppress contamination from spurious and incorrectly reconstructed tracks, charged-particle tracks were included in the analysis only if they consisted of at least 70 out of a maximum of 159 reconstructed TPC space points and featured a momentum fit with a χ^2 value per degree of freedom smaller than four. Additionally, tracks identified as candidate daughter tracks of reconstructed secondary weak-decay topologies were also rejected. The DCA of extrapolated trajectories to the primary vertex position was restricted to less than 3.2 cm along the beam direction and less than 2.4 cm in the transverse plane. These selection criteria are broad and chosen to provide a high reconstruction efficiency. As such, they are susceptible to some contamination of the primary track sample from secondary particles, such as charged hadrons produced by weak decays of K_S^0 mesons and Λ^0 baryons. One verified, however, with the applications of more stringent DCA requirements, that such secondary decays have a relatively small impact on the measured correlation functions. These and other systematic effects are discussed in Sec. V. In addition, contamination of the primary track sample by electrons originating from γ conversions and π^0-Dalitz decays is suppressed based on measurements of the track's specific ionization energy loss (dE/dx) carried out with the TPC. Average energy losses are evaluated based on the truncated average method described in Ref. [76]. The pion, kaon, proton, and electron specific energy-loss dependence on momentum is used to reject tracks compatible with an electron hypothesis. Tracks with a dE/dx within 3σ of the expectation value for electrons and outside of 3σ away of the expectation values for pions, kaons and protons, were excluded from the analysis. Further rejection of electrons produced by γ conversions was accomplished by imposing a minimum invariant-mass value of 0.05 GeV/c^2 on all charged-particle pairs considered for inclusion in the analysis. Variations of these selection criteria, discussed in Sec. V, were studied to quantify systematic effects resulting from hadron losses and contamination by secondaries.

The above criteria lead to a reconstruction efficiency of about 80% for primary particles and contamination from secondaries of about 5% at $p_{\mathrm{T}} = 1$ GeV/c [77]. No filters were used to suppress like-sign (LS) particle correlations resulting from HBT effects, which produce a strong and narrow peak centered at $\Delta\eta, \Delta\varphi = 0$ in LS correlation functions.

IV. ANALYSIS METHODOLOGY

A. Two-particle correlations

The correlation functions R_2 and P_2 are nominally independent of detection efficiencies, bin by bin in $\Delta\eta$ and $\Delta\varphi$, provided they are invariant during the data-accumulation period and independent of event characteristics and conditions [35,78]. However, particle detection efficiencies are found to exhibit a small dependence on the position of the primary vertex, v_z. This creates extraneous structures in the correlation observables R_2 and P_2 at $\Delta\eta \approx 0$ and near $|\Delta\eta| \approx 2$. Studies of these effects [50,79] showed they can be properly suppressed by measuring the single- and two-particle yields in narrow bins of v_z and calculating R_2 and P_2 as averages of correlations measured in each v_z bin. In this work, it is found that distortions can be reasonably well suppressed by using 0.5-cm-wide v_z bins. Given the fiducial v_z range of $|v_z| <$ 10 cm, this suggests the analysis would have to be carried out in $40 v_z$ bins and thus 40 sets of histograms. Instead, one uses a weight technique in which single- and two-particle histograms are incremented with v_z-dependent weights precalculated to equalize the detection response across the entire fiducial

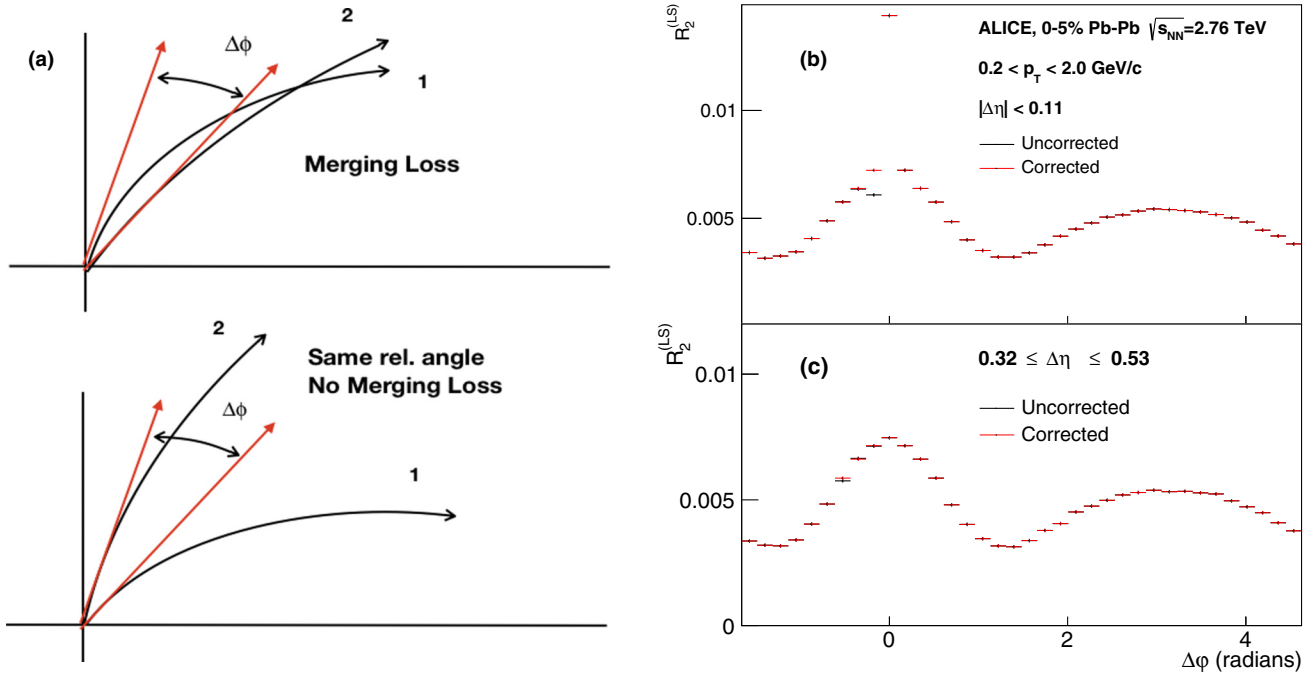

FIG. 1. (a) Schematic illustration of cowboy (top) and sailor (bottom) track topologies for like-sign pairs. (b) Projection of the correlator $R_2^{(--)}$ onto $\Delta\varphi$ for LS pairs in the range $|\Delta\eta| < 0.11$ and (c) in the range $0.32 \leqslant \Delta\eta < 0.53$.

acceptance [50]. Weights $w_{\pm}(\eta, \varphi, p_{\mathrm{T}}, v_z)$, are calculated independently for positively and negatively charged particles, positive and negative magnetic-field polarities, as the inverse of raw (i.e., uncorrected) particle yields, $N^{\pm}(\eta, \varphi, p_{\mathrm{T}}, v_z)$, determined as a function of pseudorapidity η, azimuthal angle φ, transverse momentum p_{T}, and the vertex position v_z of the events. The analysis reported in this work was carried out with weights calculated in 40 bins in v_z in the range $|v_z| < 10$ cm, 72 bins in φ (full azimuthal coverage), 20 bins in η in the range $|\eta| < 1.0$, and 18 bins in p_{T} in the range $0.2 < p_{\mathrm{T}} < 2.0$ GeV/c. The analysis proceeded in two stages: In the first stage, all events were processed to determine weights according to

$$w_{\pm}(\eta, \varphi, p_{\mathrm{T}}, v_z) = \frac{N^{\pm}_{\mathrm{avg}}(p_{\mathrm{T}})}{N^{\pm}(\eta, \varphi, p_{\mathrm{T}}, v_z)}, \tag{9}$$

where $N^{\pm}_{\mathrm{avg}}$ represents a p_{T}-dependent average of particle yields measured at all φ, η, and z. Calculated weights were then used in the second stage to analyze all events and obtain raw number densities $\rho_1(\eta, \varphi)$ and $\rho_2(\eta_1, \varphi_1, \eta_2, \varphi_2)$, as well as p_{T}-dependent quantities. Single-particle histograms, pair histograms, and p_{T} histograms were incremented with weights $w_{\pm}(\eta, \varphi, p_{\mathrm{T}}, v_z)$, $w_{\pm}(\eta_1, \varphi_1, p_{\mathrm{T},1}, v_z)w_{\pm}(\eta_2, \varphi_2, p_{\mathrm{T},2}, v_z)$, and $p_{T,1}p_{T,2}w_{\pm}(\eta_1, \varphi_1, p_{\mathrm{T},1}, v_z)w_{\pm}(\eta_2, \varphi_2, p_{\mathrm{T},2}, v_z)$, respectively. These histograms were used to calculate the correlators according to Eqs. (2)–(4).

The correlators R_2 and P_2 were measured for the particle pair charge combinations $(+, -)$, $(-, +)$, $(+, +)$, and $(-, -)$ separately. For a symmetric collision system such as Pb-Pb, correlations between particles are symmetric under independent reflections $\Delta\eta \to -\Delta\eta$ and $\Delta\varphi \to -\Delta\varphi$. The measured pair yields were first checked for detector effects. They are indeed symmetric under reflections $\Delta\eta \to -\Delta\eta$ and $\Delta\varphi \to -\Delta\varphi$. The correlation functions R_2 and P_2 measured in Pb-Pb collisions are thus fully symmetrized in $\Delta\eta$ and $\Delta\varphi$. In the case of the p-Pb collision system, the lack of reflection symmetry $z \to -z$ implies that only $\Delta\varphi$ symmetry is expected. In principle, the pair correlations, much like the single-particle yields, could then feature a nonsymmetric and arbitrarily complex dependence on $\Delta\eta$. In practice, one finds that the forward ($\Delta\eta > 0$) and backward ($\Delta\eta < 0$) correlation yields are equal within the statistical and systematic uncertainties of the measurement, owing, most likely, to the narrow η range of the detector acceptance relative to the very wide rapidity span of particles produced at LHC energies. The correlation functions R_2 and P_2 reported for p-Pb collisions are thus also fully symmetrized in $\Delta\eta$ and $\Delta\varphi$. Additionally, one observes that the correlation functions of $(+, +)$ and $(-, -)$ pairs are equal within statistical uncertainties. One thus does not report them independently. Overall, given the symmetry of $(+, -)$ and $(-, +)$ correlations and the observed equality of $(+, +)$ and $(-, -)$ correlations, one averages the former to obtain unlike-sign (US) and the latter to obtain like-sign (LS) R_2 and P_2 correlation functions that are fully symmetrized for both collision systems. The weight-correction procedure works very well for single-particle losses but does not address pair losses, most particularly those associated with track crossing and merging topologies for pairs with $\Delta\eta \approx 0$. We exploit the expected $\Delta\varphi$ symmetry of the correlation functions by using lossless "sailor" pair topologies to correct for losses observed with "cowboy" topologies [80]. For like-sign pairs, the two topologies are distinguished, for a given magnetic-field polarity, as schematically illustrated in Fig. 1(a), by counting

pairs based on a momentum-ordering technique: pairs featuring $p_{\mathrm{T},2} > p_{\mathrm{T},1}$ and $\Delta\varphi_{21} = \varphi_2 - \varphi_1 > 0$ are counted at $\Delta\varphi > 0$ as a pair incurring no losses, whereas pairs at $p_{\mathrm{T},2} > p_{\mathrm{T},1}$ and $\Delta\varphi_{21} = \varphi_2 - \varphi_1 < 0$ are counted at $\Delta\varphi < 0$ as a pair incurring losses. In the $\Delta\eta < 0.2$ range where such losses occur, it is thus sufficient to use pairs with $\Delta\varphi > 0$ to correct the yield of pairs with $\Delta\varphi < 0$. Projections of $R_2^{(--)}$, displayed in Fig. 1, show that losses associated with cowboy topologies are strongest at $|\Delta\eta| < 0.11$ and negligible at $|\Delta\eta| > 0.32$. A similar technique based on charge ordering is used for unlike-sign tracks. Unfortunately, this technique does not enable full efficiency correction for track pairs with $|\Delta\eta| < 0.3$ and $|\Delta\varphi| \approx 0$ radians. The 3×3 bin region centered at $\Delta\eta = \Delta\varphi = 0$ is thus undercorrected. The two-dimensional correlators reported in this work are then plotted without those bins. Note, however, that the calculation of the near-side peak widths, discussed in this work, do include the central 3×3 bins and the potentially incomplete efficiency loss correction is treated as source of systematic error.

The azimuthal dependence, $\Delta\varphi$, of the correlation function was studied by performing a Fourier decomposition in several narrow ranges of $\Delta\eta$. The Fourier decompositions were carried out by using projections of the $R_2^{(\mathrm{CI})}$ and $P_2^{(\mathrm{CI})}$ distributions onto $\Delta\varphi$ from a number of $\Delta\eta$ ranges. Given that the $R_2^{(\mathrm{CI})}$ and $P_2^{(\mathrm{CI})}$ distributions reported in this work are symmetric by construction, the decompositions are limited to cosine terms exclusively and are further limited to include terms of orders $n = 1$ to $n = 6$:

$$f(\Delta\varphi) = b_o(\Delta\eta) + 2\sum_{n=1}^{6} b_n(\Delta\eta)\cos(n\Delta\varphi), \tag{10}$$

in which b_0 and b_n are $\Delta\eta$-dependent fit coefficients. One finds that the inclusion of $n > 6$ terms does not significantly improve the fits of the $\Delta\varphi$ projections and that these higher-order coefficients are not significant. Although the inclusion of $n = 5,\ 6$ terms does improve the fits, these coefficients typically have sizable uncertainties and are thus not explicitly reported in this work.

In the case of R_2 and P_2 measured in Pb-Pb distributions, one anticipates that, at large $|\Delta\eta|$, the Fourier coefficients b_n are predominantly driven by flow effects determined by the collision system geometry. It is then useful to compare the Fourier coefficients v_n obtained with Eq. (10) to flow coefficients obtained with the scalar-product method [81,82] briefly described in Sec. IV B. One thus defines and reports, in the following, the harmonic coefficients $v_n[R_2]$ and $v_n[P_2]$ calculated from the coefficients b_n obtained from fits of projections of $R_2(\Delta\varphi)$ and $P_2(\Delta\varphi)$, respectively, according to

$$v_n[O] = \mathrm{sgn}(b_n)\sqrt{\frac{|b_n|}{1+b_0}}, \tag{11}$$

where O represents either of R_2 or P_2. The $\mathrm{sgn}(b_n)$ and the absolute value are used to account for the fact that the Fourier decomposition fits yield negative coefficients in some cases, particularly in p-Pb collisions and for high orders $n > 4$. Flow-like behavior, with sizable v_2 and v_3 coefficients, has been observed in p-Pb collisions [83]. However, as discussed in Sec. VI E, Fourier decompositions carried out in this work produce negative values for coefficients b_1, b_3, and b_4 at large-$|\Delta\eta|$ pair separations. Results of decompositions of R_2 or P_2 measured in p-Pb collisions are thus reported exclusively in terms of the coefficients b_n.

B. Measurements of v_n coefficients with the scalar-product method

The scalar-product (SP) method [81,82,84–87], a two-particle correlation method, is used to extract the v_n coefficients according to

$$v_n\{\mathrm{SP}\} = \frac{\left\langle \mathbf{u}_{n,k}\frac{\mathbf{Q}_n^*}{M}\right\rangle}{\sqrt{\left\langle \frac{\mathbf{Q}_n^a}{M^a}\frac{\mathbf{Q}_n^{b*}}{M^b}\right\rangle}}, \tag{12}$$

where $\mathbf{u}_{n,k} = \exp(in\varphi_k)$ is the unit vector of the particle of interest (POI) k, $\mathbf{Q}_n$ is the event flow vector, M is the event multiplicity, and n is the harmonic number. The full event is divided into two independent subevents a and b composed of tracks from different pseudorapidity intervals with flow vectors $\mathbf{Q}_n^a$ and $\mathbf{Q}_n^b$ and multiplicities M^a and M^b. The angle brackets denote averages over all selected particles and events. The notation Q^* represents the complex conjugate of Q.

The x and y components of the flow vector $\mathbf{Q}_n$ are

$$Q_{n,x} = \sum_l \cos(n\varphi_l), \tag{13}$$

$$Q_{n,y} = \sum_l \sin(n\varphi_l), \tag{14}$$

where the sum is carried over all reference particles (RPs) l in the relevant (sub-)event.

Unidentified charged particles from a certain p_{T} interval are taken as POIs and correlated with RPs from the full p_{T} range. The subevents a and b are defined within the pseudorapidity range $-1.0 < \eta < -0.1$ and $0.1 < \eta < 1.0$, which results in a pseudorapidity gap of $|\Delta\eta| > 0.2$ that reduces nonflow contributions. To further suppress nonflow effects, a pseudorapidity gap of $|\Delta\eta| > 0.9$ is also employed by selecting a and b within $-1.0 < \eta < -0.45$ and $0.45 < \eta < 1.0$. The POIs are taken from a and the RPs from b and vice versa. Nonuniformities in the detector azimuthal acceptance influence the v_n coefficients at a level of less than 0.1%.

V. SYSTEMATIC UNCERTAINTIES

Sources of systematic effects were investigated to assess their impact on the two-dimensional correlation functions, their projections onto the $\Delta\eta$ and $\Delta\varphi$ axes, the width of the near-side peak of the CI and CD correlation functions, and the coefficients extracted from the $\Delta\eta$-dependent Fourier decompositions of $\Delta\varphi$ projections of the CD correlations, as well as on the flow coefficients extracted with the scalar-product method. Systematic effects are considered significant if the maximum span of variations obtained by varying a given parameter (or condition) exceeded the statistical uncertainties of the observable considered or if variations were observed

TABLE I. Maximum systematic uncertainties of the correlation widths, $\langle\Delta\eta\rangle$. Values marked with a dash are too small to be measurable. Total uncertainties are obtained as sums in quadrature of individual contributions.

Category	Correlation function	Pb-Pb	p-Pb
	R_2	1.6%	–
Magnetic field	P_2	1.9%	–
	R_2	0.3%	–
Centrality determination	P_2	0.7%	–
	R_2	1.9%	2.8%
z-vertex binning	P_2	2.8%	3.6%
	R_2	2.4%	2.9%
Track selection	P_2	3.4%	3.9%
	R_2	0.4%	0.6%
Electron rejection	P_2	0.9%	0.8%
	R_2	0.14%	–
Tracking efficiency	P_2	0.26%	–
	R_2	3%	3%
$\Delta\eta = 0$, $\Delta\varphi = 0$ bin	P_2	3%	3%
	R_2	4.6%	5.8%
Total	P_2	5.1%	6.1%

TABLE II. Systematic uncertainties on v_n from R_2, P_2, and SP in Pb-Pb collisions. Values marked with a dash are too small to be measurable or not applicable. Total uncertainties are obtained as sums in quadrature of individual contributions.

Category	Method	v_2	v_3	v_4
	R_2	1.1%	0.6%	1.4%
Magnetic field	P_2	1.4%	0.9%	1.6%
	SP	–	–	–
	R_2	0.7%	0.7%	1.1%
Centrality determination	P_2	0.5%	0.8%	1.6%
	SP	1.0%	1.0%	1.0%
	R_2	1.6%	2.0%	3.2%
Vertex-Z binning	P_2	1.9%	2.8%	3.7%
	SP	–	–	–
	R_2	3.5%	3.2%	5.3%
Track selection	P_2	4.9%	4.9%	6.2%
	SP	2.2%	2.2%	2.2%
	R_2	0.6%	0.3%	0.8%
Electron rejection	P_2	1.0%	0.8%	1.3%
	SP	–	–	–
	R_2	0.4%	0.2%	0.7%
Efficiency effect	P_2	1.2%	0.9%	1.6%
	SP	3.0%	4.0%	4.0%
	R_2	3.0%	6.0%	8.0%
$\Delta\varphi$ binning	P_2	7.0%	11.0%	13.0%
	SP	–	–	–
	R_2	–	–	–
No. of TPC clusters	P_2	–	–	–
	SP	2.0%	2.0%	5.0%
	R_2	–	–	–
Comparison to Monte Carlo	P_2	–	–	–
	SP	3.0%	4.0%	5.0%
	R_2	5.1%	7.2%	10.3%
Total	P_2	9%	12.5%	15.0%
	SP	5.3%	6.5%	8.5%

for the same data sample. Contributions of sources yielding significant deviations were found to be uncorrelated and thus added in quadrature to obtain the total systematic uncertainties reported in Tables I–III and all plots presented in this paper.

We first consider systematic effects on the overall amplitude of the correlation functions. The R_2 and P_2 correlators were determined with Pb-Pb data samples collected with positive- and negative-magnetic-field configurations. Peak correlator amplitude differences obtained with the two field configurations were typically small for US and LS correlators and had maximum values of 1.4% and 1.9% for R_2 and P_2 correlators, respectively. These values were adopted as systematic uncertainties associated with distortions of the solenoidal magnetic field, the TPC electric field, and corrections for space-charge effects. Given that the amplitude and shape of the correlators is dependent on the produced-particle multiplicity, systematic effects associated with the collision and multiplicity selection were assessed by repeating the Pb-Pb and p-Pb analyses with alternative multiplicity estimators. In the case of Pb-Pb collisions, the SPD track multiplicity was used as an alternative centrality estimator, and it was found that the amplitude of the R_2 and P_2 correlation functions changed from the default analysis by at most 1.6% and 1.9%, respectively. In the case of p-Pb collisions, correlation amplitudes observed when using the V0-A and V0-C detectors for the definition of multiplicity classes were compared and one did not find statistically significant differences [88]. No systematic uncertainty is thus assigned to this contribution in p-Pb collision measurements.

Minor contributions to the systematic uncertainties arise from the selection of the v_z-vertex fiducial range. Globally, correlation functions obtained with the nominal range of $|v_z| < 10$ cm, used in this analysis, exhibit amplitude differences smaller than 1% relative to those obtained with a more restrictive vertex-position range of $|v_z| < 6$ cm. Additionally, it is found that increasing the vertex bin width (used in the correction weight calculation) by a factor of two yielded correlation amplitude changes of at most 4% relative to the nominal bin size reported in this work.

Systematic uncertainties also arise from the charged-particle track definition and track quality selection criteria. These uncertainties were examined by repeating the correlation analyses using track-selection criteria distinct from the nominal criteria described in Sec. III. The varied track quality criteria included the minimal number of TPC space points per track, the maximum χ^2 per degree of freedom obtained in the momentum fit, as well as the maximum track distance of closest approach (DCA) to the primary vertex (both along the beam direction and in the transverse plane). Variations of these track quality selection criteria typically have a rather small impact on the amplitude of the correlation functions (up to 0.8% for R_2 and 1.2% for P_2), but nonetheless have measurable effects on the width of the near-side peak of the CI and CD correlation functions listed in Table I.

The differences between correlation functions obtained with charged-particle tracks reconstructed with only TPC hits

TABLE III. Maximum systematic uncertainties on b_n coefficients obtained from R_2 and P_2 in p-Pb collisions. Total errors are obtained as sums in quadrature of individual contributions.

Category	Correlation function	b_1	b_2	b_3	b_4
z-vertex binning	R_2	1.4%	1.2%	1.9%	2.7%
	P_2	2.0%	1.7%	2.2%	3.2%
Track selection	R_2	8.3%	6.4%	8.1%	8.9%
	P_2	10.8%	9.3%	10.9%	11.0%
Electron rejection	R_2	0.9%	0.2%	0.7%	0.9%
	P_2	0.7%	0.9%	0.8%	1.0%
$\Delta\varphi$binning	R_2	0.1%	0.2%	0.7%	1.3%
	P_2	0.2%	0.6%	1.1%	2.0%
Total	R_2	8.5%	6.5%	8.4%	9.4%
	P_2	11.0%	9.5%	11.2%	11.7%

(known as TPC tracks), TPC tracks refitted to include the primary vertex, and so-called hybrid tracks, which include a mixture of TPC tracks with vertex refit and tracks that also include one or several hits in the ITS, were considered. Amplitude differences between correlation functions obtained with TPC tracks only and TPC tracks with a primary vertex refit are typically small, i.e., less than 5%, but the R_2 and P_2 CI correlation functions exhibit differences as large as 8% and 15%, respectively, in the range $|\Delta\eta| < 0.6$, $|\Delta\varphi| < 0.6$, in the most-central collisions. The impact of these amplitude changes on the width and shape of the correlation functions is summarized in Tables I and II. Correlation functions, most particularly $P_2^{(\mathrm{CD})}$ correlations, obtained with hybrid tracks featured significant distortions associated with TPC sector boundary. Correlation functions obtained with these tracks were thus not included in our assessment of systematic effects associated with the track quality and the track reconstruction algorithm.

Uncertainties associated with the criteria used for rejection of electron contamination were studied by varying the selection criteria on deviations from the expected Bethe-Bloch parametrization of the specific ionization energy loss, dE/dx, for electrons from 3σ to 5σ. Changes in the correlation function amplitude were smaller than 1.3% for both collision systems and all multiplicity classes.

Systematic uncertainties associated with the track-by-track efficiency and contamination corrections were studied by using simulated p-Pb and Pb-Pb collisions produced with the HIJING event generator [89,90] and propagated through a GEANT3 [91] model of the ALICE detector. Correlation functions obtained at the event generator level were compared with those obtained after taking full account of detector effects. Deviations are typically negligible in noncentral collisions. Maximum discrepancies of about 1.6% were found in the most-central Pb-Pb collisions. No measurable effects were observed in the most-peripheral Pb-Pb collisions and p-Pb collisions.

Systematic uncertainties on the width of the near side of the CI and CD correlation functions were studied by repeating the analysis with the variations discussed earlier in this section. Additionally, the effect of the incomplete efficiency correction in the $(\Delta\eta, \Delta\varphi) = (0, 0)$ bin was studied by arbitrarily doubling the correlation yield in that bin. Such a change produces width reductions smaller than 3%. All systematic uncertainty contributions to the near-side peak widths are listed in Table I.

Systematic effect studies pertaining specifically to the determination of the azimuthal dependence of the correlations, and most particularly the Fourier decomposition coefficients extracted from R_2 and P_2, LS, US, and CI correlation functions were also carried out. These correlation functions were initially determined with 72 bins in $\Delta\varphi$ but rebinned to 36 bins to suppress some residual effects on the Fourier decomposition fits, particularly in the case of the P_2 correlation functions. Studies showed, however, that the coefficients extracted from R_2 are less sensitive to rebinning, within statistical uncertainties, while coefficients obtained in fits of P_2 for $n \geqslant 2$ did exhibit greater sensitivity to the rebinning. One finds that the fit coefficients are stable, with rebinning, for 0%–50% collision centralities (Pb-Pb), but measurable variations were observed for more peripheral bins. For central Pb-Pb collisions, systematic shifts for $n \geqslant 1$ coefficients were found to be smaller than 5% while shifts as large as 13% were obtained in Pb-Pb peripheral collisions. Distortions were far smaller for R_2 and P_2 correlation functions measured in p-Pb collisions. The systematic uncertainties associated with distortions are estimated to be less than one percent for this system.

The v_n coefficients extracted by using the scalar-product method were studied under variations of the number of the TPC space points (varied from 70 to 100), the collision centrality determination, the v_z binning, charged-particle track definition, different magnetic-field polarities, criteria for electron rejection, and various other aspects of the detector response. Systematic uncertainties inferred from these studies are presented in Table III. We also studied the impact of the detector response based on GEANT simulations of HIJING [89,90] and AMPT [92] events. We compared v_n coefficients evaluated directly from the models with those obtained from reconstructed tracks (i.e., tracks obtained from a simulation of the detector performance) and assessed maximum systematic uncertainties of 3%, 4%, and 5% for v_2, v_3, and v_4, respectively.

Systematic uncertainties associated with the extraction of the average correlation function widths $\langle\Delta\eta\rangle$, discussed in Sec. VI D, are summarized in Table I, whereas typical values of systematic uncertainties of the flow harmonic v_n coefficients measured in Pb-Pb collisions, reported in Sec. VI E, are summarized in Table II. Similarly, systematic uncertainties associated with the Fourier decomposition coefficients b_n obtained for p-Pb collisions are summarized in Table III. Systematic uncertainty values listed in these tables correspond to maximum differences encountered for each system and across all multiplicity classes and all pseudorapidity ranges considered in this analysis.

VI. RESULTS

Measurements of the correlation functions R_2 and P_2 for LS and US particle pairs are presented in Sec. VI A while charge-independent (CI) and charge-dependent (CD) correlation functions constructed from these are presented in

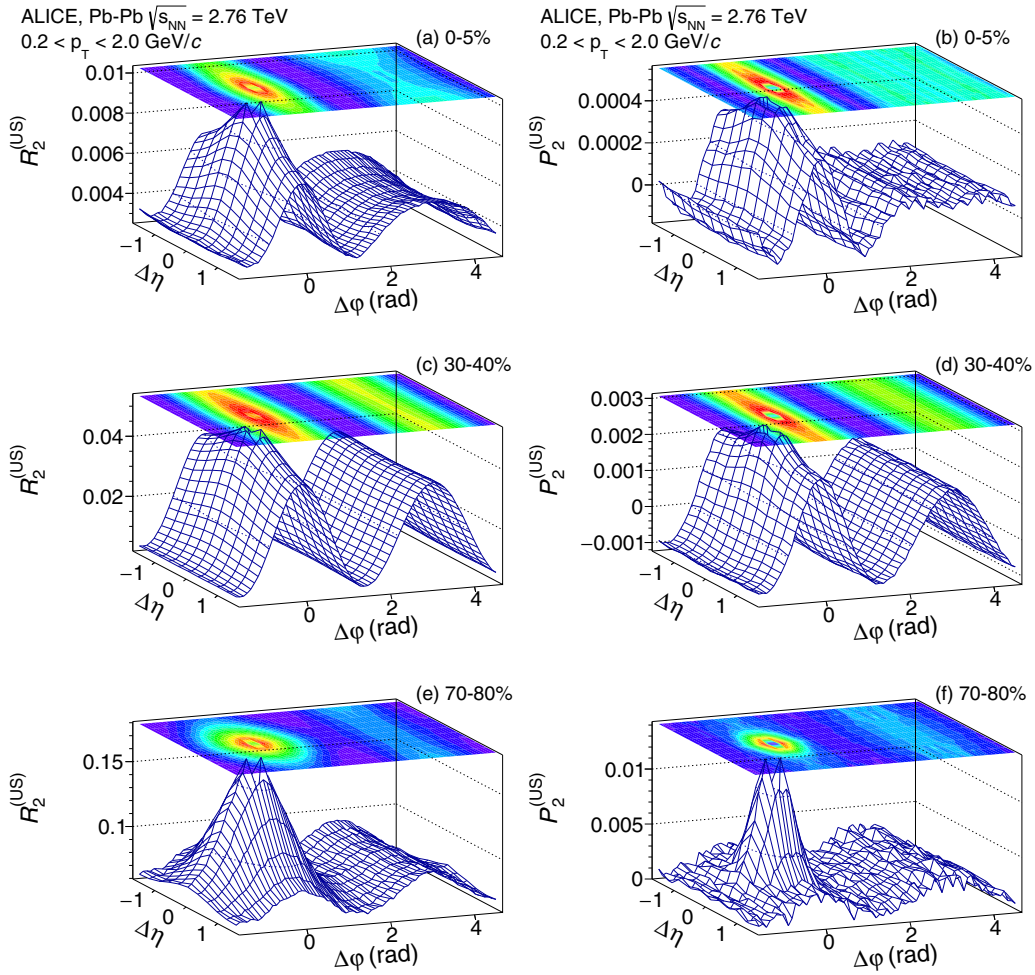

FIG. 2. Correlation functions $R_2^{(US)}$ (left column) and $P_2^{(US)}$ (right column) of charged hadrons in the range $0.2 < p_T < 2.0\,\text{GeV}/c$ measured in Pb-Pb collisions at $\sqrt{s_{NN}} = 2.76\,\text{TeV}$ for selected centrality classes.

Secs. VI B and VI C, respectively. The amplitude, shape, and width of R_2 and P_2 CI and CD correlations are sensitive to the particle-production dynamics as well as to the system evolution. Several phenomena may in fact contribute to shaping the azimuthal and longitudinal dependence of these correlation functions, including anisotropic and radial flow, thermal diffusion [46], as well as two-stage quark production [38]. A detailed characterization of the longitudinal and azimuthal profiles of both CI and CD correlation functions is thus of interest to further improve the understanding of these competing mechanisms and effects. Section VI D presents analyses of the correlation function longitudinal and azimuthal widths and their evolution with increasing produced-particle multiplicity. Section VI E reports studies of Fourier decompositions of azimuthal projections of R_2 and P_2 as a function of the longitudinal separation of particle pairs. Altogether, these different studies enable the characterization of flow and nonflow components in Pb-Pb and p-Pb collisions.

A. Like-sign and unlike-sign correlation functions

The R_2 and P_2 correlation functions measured in Pb-Pb collisions are displayed in Figs. 2 and 3 for unlike- and like-sign pairs for three representative multiplicity classes corresponding to 70%–80% (peripheral collisions), 30%–40% (mid-central collisions), and 0%–5% (most-central collisions) fractions of the cross section. The corresponding correlation functions measured in p-Pb collisions are shown in Figs. 4 and 5 for event multiplicity classes corresponding to fractions of cross sections of 60%–100%, 20%–40%, and 0%–20%. These do not unambiguously map to distinct p-Pb collision impact parameters or centrality.

One observes that the $R_2(\Delta\eta, \Delta\varphi)$ and $P_2(\Delta\eta, \Delta\varphi)$ correlation functions measured in Pb-Pb and p-Pb exhibit similar trends with increasing multiplicity. Although they have quite different amplitudes, owing to the $\Delta p_T \Delta p_T$ dependence of P_2, one finds correlation amplitudes to be largest in peripheral Pb-Pb collisions and low-multiplicity classes in p-Pb. Furthermore, the amplitudes of the R_2 and P_2 correlation functions qualitatively exhibit similar decreasing trends with increasing particle multiplicity, reaching the smallest values in the 5% and 20% highest multiplicity classes in Pb-Pb and p-Pb collisions, respectively. A similar dependence on produced-particle multiplicity has been observed for both triggered and untriggered number correlation functions [6,20,22,26,62,93,94] but is reported for the first time, in this

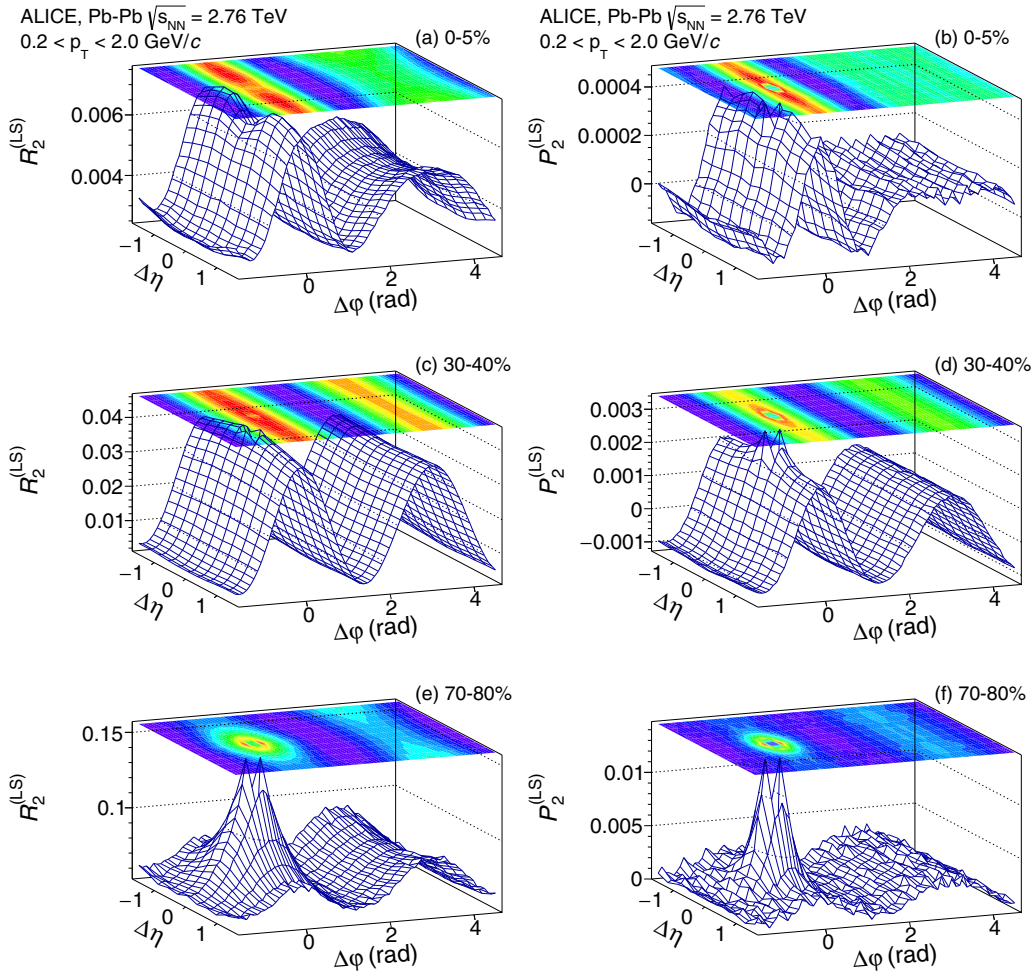

FIG. 3. Correlation functions $R_2^{(\mathrm{LS})}$ (left column) and $P_2^{(\mathrm{LS})}$ (right column) of charged hadrons in the range $0.2 < p_{\mathrm{T}} < 2.0\,\mathrm{GeV}/c$ measured in Pb-Pb collisions at $\sqrt{s_{\mathrm{NN}}} = 2.76\,\mathrm{TeV}$ for selected centrality classes.

work, for the P_2 observable. It results in a large part from the increasing number of elementary interactions (e.g., parton-parton interactions) associated with the growing geometrical overlap of the colliding nuclei.

In addition, the R_2 and P_2 correlation functions exhibit a strong near-side peak in 70%–80% Pb-Pb collisions. This peak is noticeably narrower, along both the $\Delta\eta$ and $\Delta\varphi$ axes, in the P_2 correlations, a feature we study quantitatively in Sec. VI D. Both R_2 and P_2 correlations are strongly modified in higher multiplicity collisions with the emergence of strong $\Delta\varphi$ modulations, known to arise from anisotropic flow in Pb-Pb collisions. Although the near-side peak remains an important feature of US correlations, in all multiplicity classes, it appears significantly overshadowed by flow-like modulations in the 5% highest multiplicity LS correlations. One additionally finds that the R_2 correlations are positive, although, as cumulants, they are not required to be, while the P_2 correlations feature $\Delta\varphi$ ranges where the correlation strength is negative. Such negative values reflect $\Delta\varphi$ intervals in which, on average, the p_{T} of one particle might be found above $\langle p_{\mathrm{T}}\rangle$, while the other is below $\langle p_{\mathrm{T}}\rangle$, effectively yielding a negative $\Delta p_{\mathrm{T}}\Delta p_{\mathrm{T}}$ value. One also observes that the P_2 and R_2 away-side (i.e., for $\Delta\varphi \sim \pi$) dependence on the relative pseudorapidity, $\Delta\eta$, are qualitatively different. While R_2 features a bowed shape, i.e., a concave dependence on $\Delta\eta$ with a minimum at $\Delta\eta = 0$, the away-side strength of the P_2 correlation is essentially flat, i.e., independent of $\Delta\eta$ within uncertainties. Similar concave dependencies also reported by the CMS collaboration in high-multiplicity pp collisions [95] and by the STAR collaboration in 5% central Au-Au collisions [96].

Another interesting difference between R_2 and P_2, visible in US (Fig. 2) and LS (Fig. 3) correlations involves their away-side dependence on $\Delta\varphi$ in the 5% highest multiplicity collisions. One finds that the away-side of P_2 exhibits a broad structure extending over the full range of the measured $\Delta\eta$ acceptance and features a weak double-hump structure with a minimum at $\Delta\varphi = \pi$ and side peaks located approximately at $\Delta\varphi = \pi \pm \pi/3$, while the R_2 correlation function, in the same multiplicity class, exhibits a convex dependence on $\Delta\varphi$. It is worth noting, however, that double-hump structures similar to that observed in P_2 have already been reported with triggered and untriggered number correlations, albeit only for A-A collision centralities in the range 0%–2% [6,97]

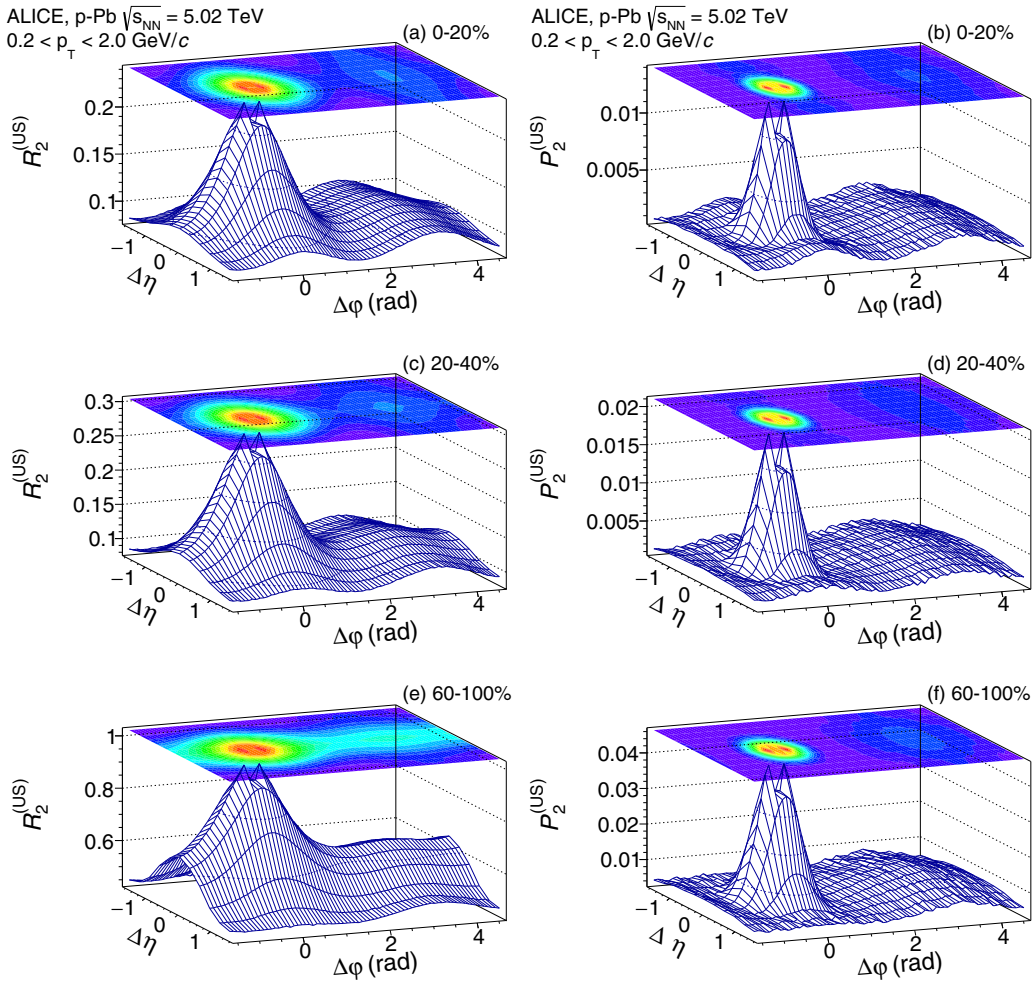

FIG. 4. Correlation functions $R_2^{(US)}$ (left column) and $P_2^{(US)}$ (right column) of charged hadrons in the range $0.2 < p_T < 2.0$ GeV/c measured in p-Pb collisions at $\sqrt{s_{NN}} = 5.02$ TeV for selected multiplicity classes.

or after subtraction of a v_2 flow background in less-central collisions [20,23,24]. These features were initially associated with conical particle emission [24,98–107] but are now understood to be caused by strong triangular flow (v_3) originating from initial-state fluctuations in A-A collisions [29]. The P_2 correlation function features a double hump structure already in the 5% Pb-Pb collisions, by contrast with the more-central collisions required to identify a similar structure in R_2. This suggests that P_2 correlations are more sensitive to the presence of the triangular flow component [108]. We thus carry out a comparative analysis of the Fourier decompositions of the R_2 and P_2 correlation functions both as a function of collision centrality and pseudorapidity difference in Sec. VI E.

We contrast the near-side peaks of LS and US correlation functions and their evolution with produced-particle multiplicity. The $R_2^{(US)}$ and $P_2^{(US)}$ correlation functions feature stronger near-side peaks than the $R_2^{(LS)}$ and $P_2^{(LS)}$ correlation functions in equivalent multiplicity classes. Additionally, the amplitudes of the near-side peaks of the US correlation functions decrease in higher multiplicity classes but remain an essential feature of both R_2 and P_2. By contrast, the $R_2^{(LS)}$ and $P_2^{(LS)}$ near-side peaks not only weaken in amplitude, but essentially disappear in higher-multiplicity classes in Pb-Pb, leaving behind near-side structures with a complicated dependence on $\Delta\eta$. The LS correlation functions measured at the highest multiplicities (Fig. 2) hint that R_2 and P_2 are sensitive to different aspects of the correlation dynamics, which we discuss in greater detail in Sec. VII.

We next focus on the US and LS correlation functions measured in p-Pb collisions, displayed in Figs. 4 and 5. We find that both the R_2 and P_2 correlation functions feature prominent near-side peaks similar to those observed in most-peripheral Pb-Pb collisions. Unlike Pb-Pb collisions, however, the near-side peaks of both R_2 and P_2 dominate the correlation functions irrespective of their multiplicity class, although the peak amplitude decreases, as expected, with increasing particle multiplicity. Flow-like $\Delta\varphi$ modulations are observed in the 20%–40% and 0%–20% multiplicity classes that are qualitatively similar to those reported by the CMS collaboration [109] in very-high-multiplicity triggered events and those observed by the ALICE collaboration for charged particles in the range $0.2 < p_T < 3.0$ GeV/c in the same multiplicity classes [83]. The amplitude of the modulations is further examined in Sec. VI E of this article.

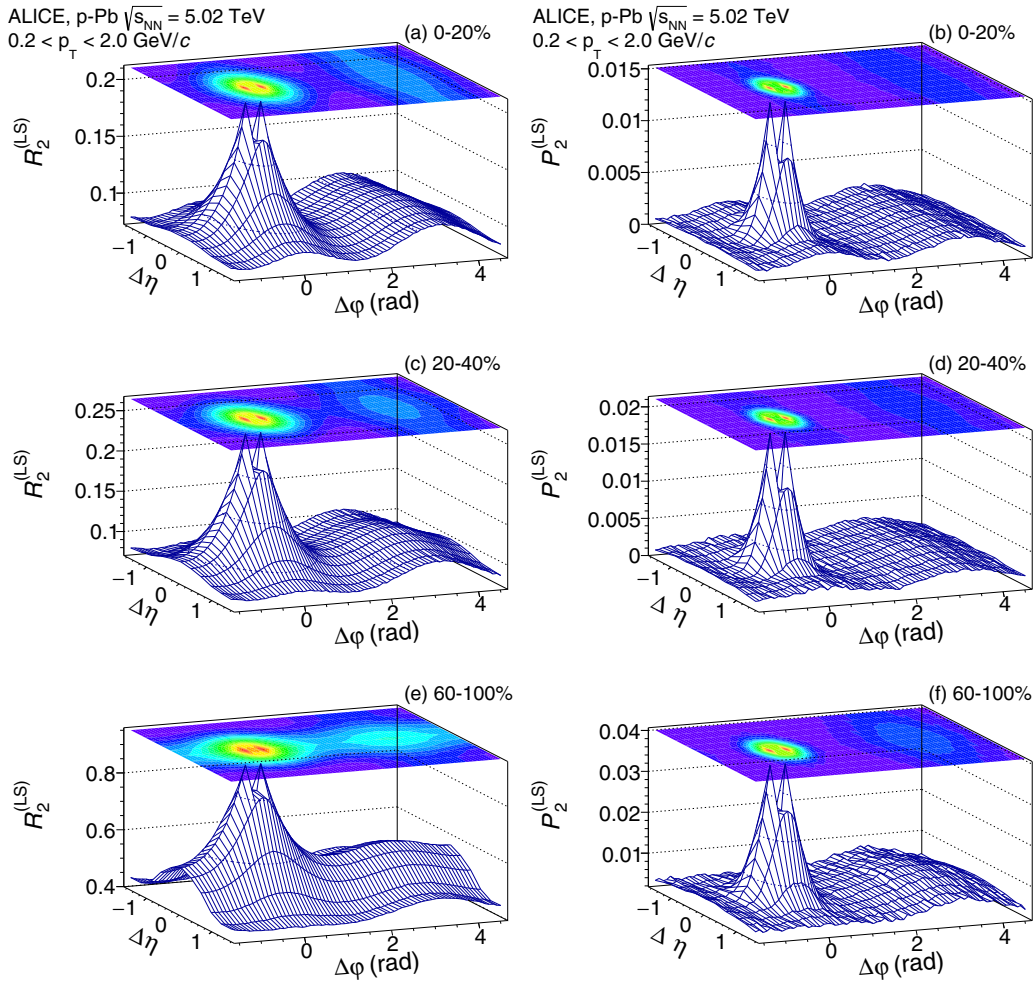

FIG. 5. Correlation functions $R_2^{(\mathrm{LS})}$ (left column) and $P_2^{(\mathrm{LS})}$ (right column) of charged hadrons in the range $0.2 < p_{\mathrm{T}} < 2.0\,\mathrm{GeV}/c$ measured in p-Pb collisions at $\sqrt{s_{\mathrm{NN}}} = 5.02\,\mathrm{TeV}$ for selected multiplicity classes.

Furthermore, one notes that the near-side peak of US and LS P_2 correlation functions measured in p-Pb collisions is considerably narrower than those observed in R_2. Additionally, the shape of the near-side peaks observed in US and LS correlation functions are remarkably different. The US peaks are wider and rounder at the top, while the LS peaks are very narrow at the top but appear to fan out with relatively longer tails along both the $\Delta\eta$ and $\Delta\varphi$ axes. Such differences may arise in part due to Coulomb and HBT effects. The evolution of the width of the near-side peak of the R_2 and P_2 distributions as a function of the multiplicity class are discussed in Sec. VI D.

In addition, the R_2 correlation functions observed in p-Pb feature an away-side shape and dependence on $\Delta\eta$ significantly different from those observed in Pb-Pb. The away side of R_2 observed in the lowest p-Pb multiplicity class is dominated by a structure essentially independent of $\Delta\varphi$ and with a strong concave dependence on $\Delta\eta$. This structure progressively evolves, with increasing multiplicity, into an elongated, but still concave, $\Delta\eta$ distribution in the 0%–20% multiplicity class. In contrast, the away-side of P_2 correlations features a much smaller amplitude (relative to the near-side peak) and exhibits a weaker dependence on $\Delta\eta$ than observed in R_2.

Finally, at large multiplicity, one also notes the emergence of flow-like modulations in both the R_2 and P_2 correlation functions. A quantitative study of the strength of these modulations is presented in Sec. VI E.

B. Charge-independent correlations

Figures 6 and 7 present $R_2^{(\mathrm{CI})}$ and $P_2^{(\mathrm{CI})}$ correlation functions, determined according to Eq. (5), for selected multiplicity classes in Pb-Pb collisions at $\sqrt{s_{\mathrm{NN}}} = 2.76\,\mathrm{TeV}$ and p-Pb collisions at $\sqrt{s_{\mathrm{NN}}} = 5.02\,\mathrm{TeV}$, respectively. The CI correlation functions constitute signatures of the particle-production dynamics and the evolution of the collision system formed in Pb-Pb and p-Pb interactions. As averages of the US and LS distributions, these carry essentially the same features as these correlation functions. They show the same decreasing amplitude trend as a function of collision centrality in Pb-Pb collisions and multiplicity classes in p-Pb collisions, as well as the emergence of strong $\Delta\varphi$ modulation in mid-central Pb-Pb collisions. In absence of medium-induced effects, the

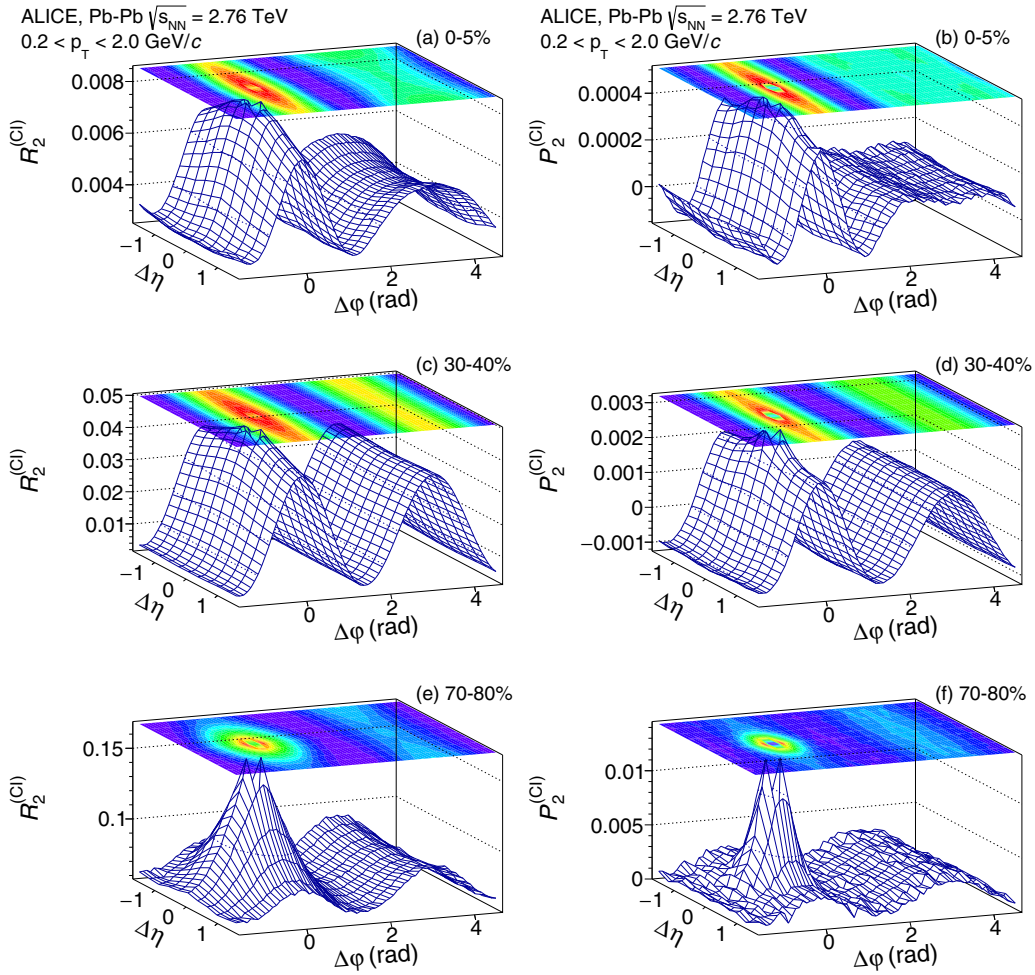

FIG. 6. Correlation functions $R_2^{(CI)}$ and $P_2^{(CI)}$ measured with charged particles in the range $0.2 < p_T < 2.0$ GeV/c for selected centrality classes in Pb-Pb collisions.

shape of these correlation functions should be independent of the collision centrality and their magnitude should scale with the inverse of the number of binary nucleon-nucleon collisions. From Figs. 6 and 7, one observes that the two correlation functions exhibit decreasing amplitude with increasing multiplicity in both Pb-Pb and p-Pb collisions. However, both R_2 and P_2 correlation functions show nonscaling behavior: their shapes, i.e., dependencies on $\Delta\eta$ and $\Delta\varphi$, significantly evolve with increasing multiplicity in both p-Pb and Pb-Pb collisions. This lack of scaling indicates a different reaction dynamics and collision system evolution with produced particle multiplicity. The appearance of strong $\Delta\varphi$ modulations, associated with collective flow, has been observed in several measurements of two-particle correlation functions [20,26,93,94]. We find that both the near-side and flow-like feature of P_2 and R_2 exhibit a somewhat different evolution with produced-particle multiplicity. The near-side peak of P_2 correlations is significantly narrower in $\Delta\eta$ and $\Delta\varphi$ than that observed with R_2. One also notes that the away-side of P_2 has a significantly different evolution with collision centrality than R_2, featuring a dip and double-hump structure in 5% most-central Pb-Pb collisions not seen in R_2 correlation of the same centrality class. Clearly, the P_2 observable is more sensitive to the presence of higher harmonics than R_2. The flow components of the two observables, however, are not independent and have been reported to be closely related [108]. The harmonics coefficients v_n obtained with the P_2 observable, for relative pseudorapidities $\Delta\eta > 0.9$ are successfully predicted by a simple formula, known as the flow ansatz [35,108]. This ansatz is based on the notion that two-particle correlations observed in Pb-Pb collisions are predominantly determined by particle emission relative to a collision's symmetry plane. The dependencies of the harmonic flow coefficients v_n on charge combination, pseudorapidity difference $\Delta\eta$, and produced-particle multiplicity are presented in more detail in Sec. VI E.

C. Charge-dependent correlations

Energy-momentum and quantum number (e.g., charge, strangeness, baryon number) conservation laws govern the production of particles and thus have a strong impact on correlation functions. Given the very-high-energy scale reached in the Pb-Pb and p-Pb interactions reported in this work, it is reasonable to assume that considerations of energy-momentum conservation may play an equally important role in the

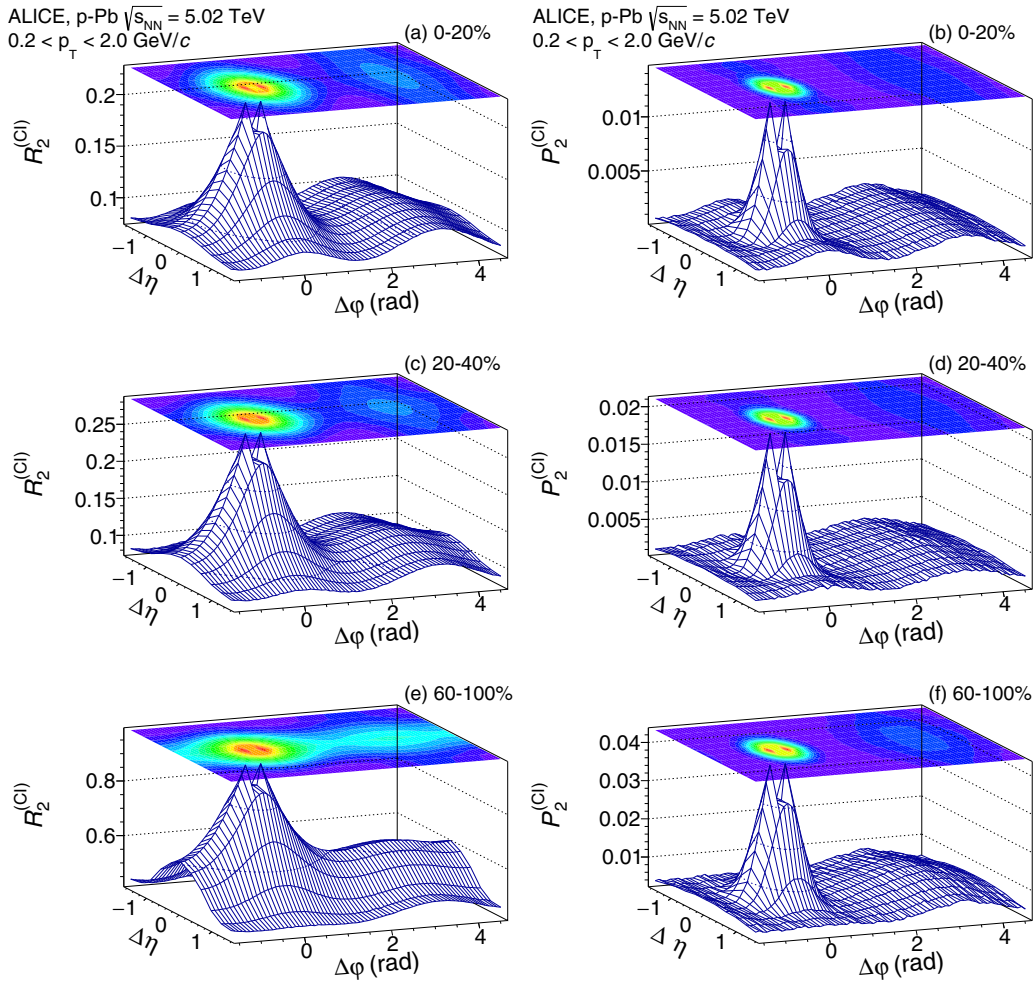

FIG. 7. Correlation functions $R_2^{(CI)}$ and $P_2^{(CI)}$ measured with charged particles in the range $0.2 < p_T < 2.0$ GeV/c for selected multiplicity classes in p-Pb collisions.

production of LS and US charge pairs. One should then be able to remove, or at least suppress, the effect of energy-momentum conservation on particle correlations by considering charge-dependent (CD) correlation functions. The shape and strength of CD correlation functions should thus be predominantly driven by processes of creation of charge pairs, their transport, and the fact that electric charge is a conserved quantity.

The CD correlation functions $R_2^{(CD)}$ and $P_2^{(CD)}$, shown in Figs. 8 and 9, respectively, were obtained according to Eq. (6) based on US and LS correlation functions presented in Sec. VI A. In 70%–80% central Pb-Pb collisions, the $R_2^{(CD)}$ correlation function features a very strong and relatively broad near-side peak that extends to $\Delta\varphi \sim \pi$ and slowly decreases in amplitude for large values of $|\Delta\eta|$. The width of the near-side peak narrows in the centrality range 30%–40% and even more in the 0%–5% range. One notes, in particular, that the away side of these two correlation functions is essentially flat and nearly vanishing, except for minor and incompletely corrected detector effects—most noticeable in the case of the $P_2^{(CD)}$ observable in Fig. 8. The low-amplitude, high-frequency modulations seen on the away-side of $P_2^{(CD)}$ in the 0%–5% collisions are due to instrumental effects near the boundaries between TPC sectors. Although these effects are very much suppressed by the weight-based analysis used in this work, they could not be completely eliminated. The presence of narrow near-side peaks as well as flat and essentially vanishing away side in $R_2^{(CD)}$ and $P_2^{(CD)}$ indicate that the US pair production on the near and away sides (seen in $R_2^{(CD)}$ and $P_2^{(CD)}$) are uncorrelated and causally disconnected. By contrast, the finite away-side amplitude observed in the charge-independent correlation functions $R_2^{(CI)}$, shown in Fig. 6, indicates that the corresponding charged-particle correlations must arise from particle-production mechanisms insensitive to charge conservation.

The narrowing of $R_2^{(CD)}$ observed with increasing produced-particle multiplicity in Figs. 8 and 9 is qualitatively similar to the narrowing of the balance function (BF) reported by the ALICE collaboration [62,63]. A quantitative comparison of the widths obtained from $R_2^{(CD)}$ correlations and those already reported for the BF is presented in Sec. VI D.

The strength of $P_2^{(CD)}$ in Pb-Pb collisions is approximately one order of magnitude weaker than that of $R_2^{(CD)}$. One finds that the away-side of $P_2^{(CD)}$ is essentially flat, i.e., independent

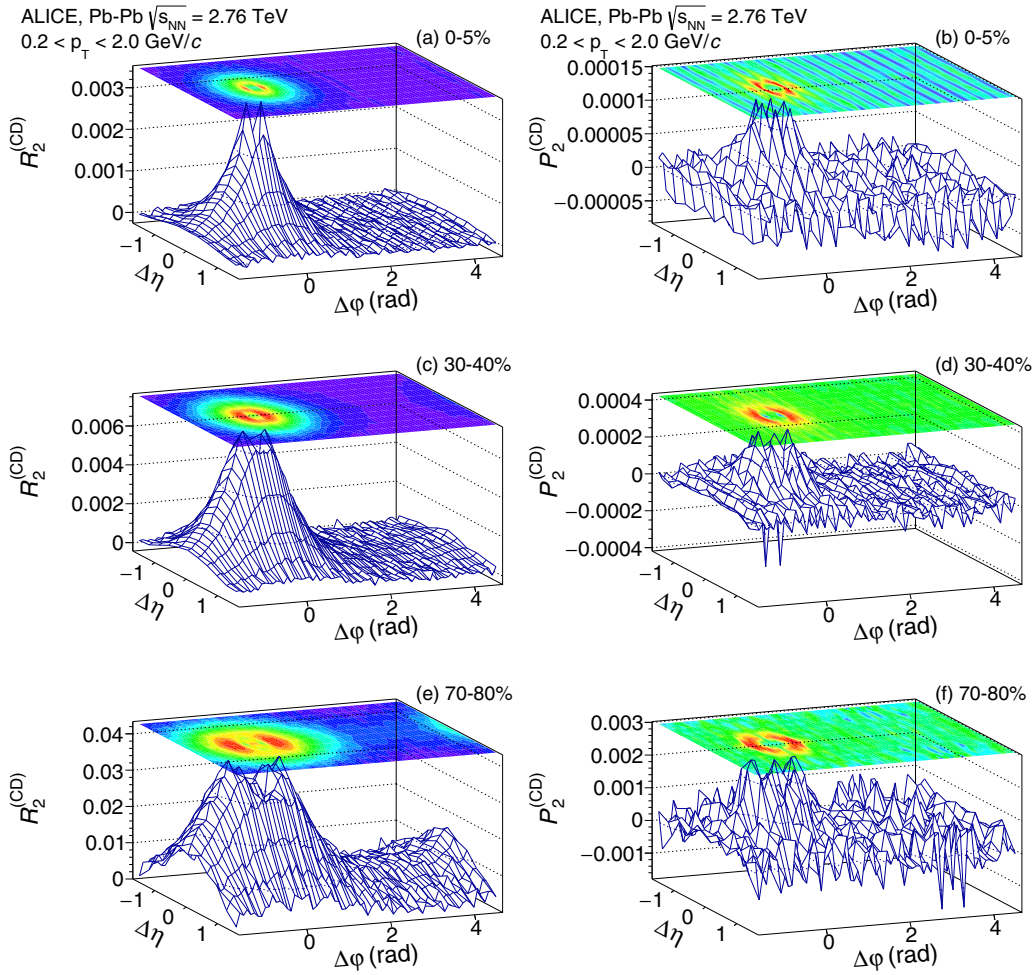

FIG. 8. Correlation functions $R_2^{(CD)}$ and $P_2^{(CD)}$ measured with charged particles in the range $0.2 < p_T < 2.0$ GeV/c for selected centrality classes in Pb-Pb collisions.

of $\Delta\eta$ and $\Delta\varphi$, in all centrality classes. The salient feature of $P_2^{(CD)}$ is a near-side peak significantly narrower than the near-side peak observed in $R_2^{(CD)}$. This is an interesting result given that both R_2 and P_2 are derived from the same two-particle density $\rho_2(\vec{p}_1, \vec{p}_2)$. It provides indications that the product $\Delta p_{T,1}\Delta p_{T,2}$ has a significant dependence on $\Delta\eta$ and $\Delta\varphi$ for correlated US pairs. Also, note that, in Fig. 9, the near-side peak of P_2 observed in p-Pb collisions exhibits a circular and narrow undershoot ring at $\sqrt{|\Delta\eta|^2 + |\Delta\varphi|^2} \sim 0.75$. For larger particle separations, the product $\Delta p_{T,1}\Delta p_{T,2}$ is approximately constant and averages to a small positive value whereas, for smaller separations, it forms a clear peak. In the undershoot region, the strength of the correlation dips to zero or even below zero. The origin of the very narrow width of the P_2 near-side peak and the presence of the undershoot is discussed in Sec. VII.

It is interesting to compare the $R_2^{(CD)}$ and $P_2^{(CD)}$ correlation functions obtained in p-Pb collisions, shown in Fig. 9, with those obtained in Pb-Pb collisions discussed above. The $R_2^{(CD)}$ correlation functions feature strong and broad near-side peaks similar to that observed in the 70%–80% centrality range. However, the latter has an amplitude smaller than those featured in Fig. 9, consistent with the notion that collisions in that centrality range involve a significant geometrical overlap yielding a larger number of binary collisions, on average, than p-Pb collisions. One also notes that the near-side peak observed in 0%–20% collisions remains fairly broad and features an amplitude nearly half of that observed in 60%–100% collisions. Finally, one also observes that all three multiplicity classes feature finite correlation amplitudes at $\Delta\eta \approx 0$, $\Delta\varphi \approx \pi$, much like the $R_2^{(CD)}$ distribution observed in 70%–80% Pb-Pb collisions. These features have already been reported in Ref. [63]. Remarkably, all three p-Pb $P_2^{(CD)}$ shown in Fig. 9 exhibit essentially uniform, but nonvanishing, correlation amplitudes on the away-side. This indicates that P_2 correlations manifest a different sensitivity to particle production than number correlations R_2. Note that such a conclusion could not be readily established based on the 70%–80% centrality range in Pb-Pb collisions for the $P_2^{(CD)}$ distribution because of finite residual sector boundary effects observed in that distribution. One additionally notes that all $P_2^{(CD)}$ correlation functions measured in p-Pb exhibit a rather sharp and narrow near-side peak. The width of these peaks is quantified more precisely in the next section, but it is visually rather obvious that the $P_2^{(CD)}$ near-side peaks are much narrower than those observed in $R_2^{(CD)}$ correlations. It is also interesting to notice that the

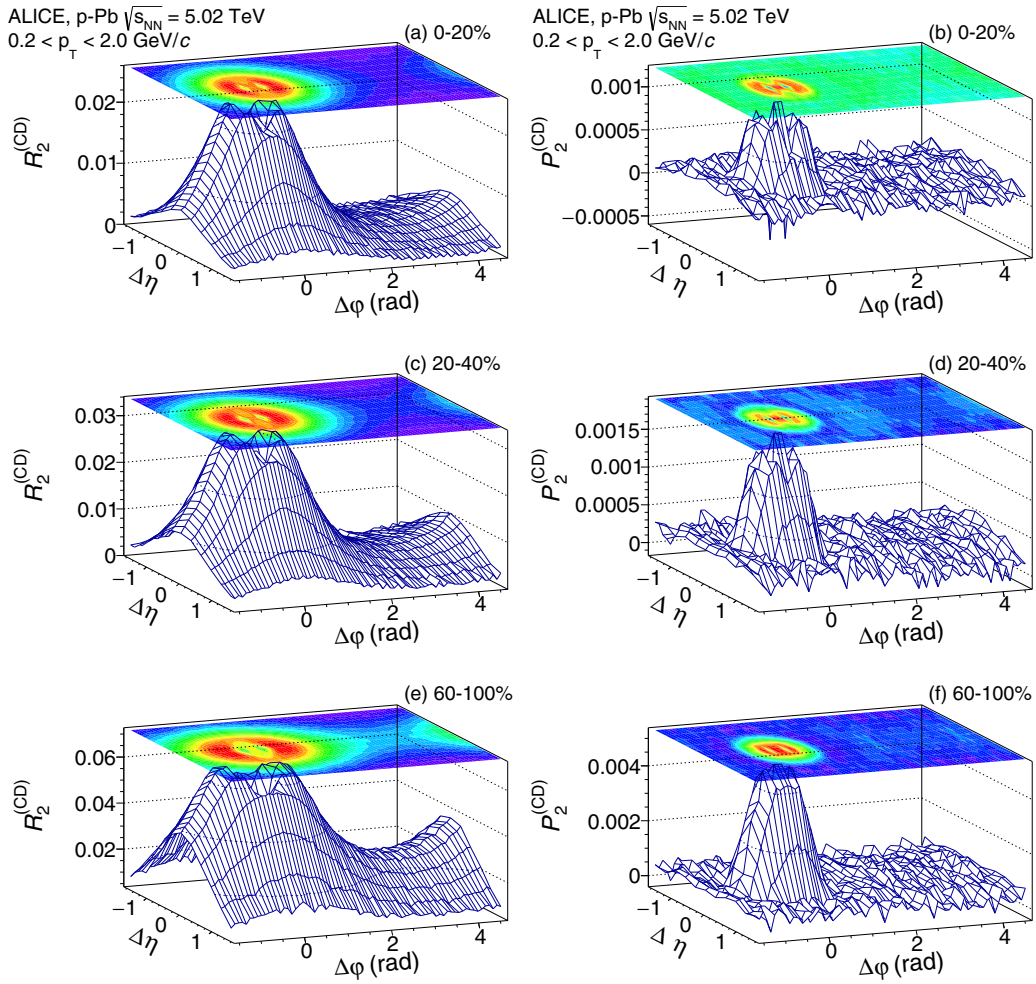

FIG. 9. Correlation functions $R_2^{(CD)}$ and $P_2^{(CD)}$ measured with charged particles in the range $0.2 < p_T < 2.0$ GeV/c for selected multiplicity classes in p-Pb collisions.

amplitude of the near-side reduces by about a factor of five from 60%–100% to 0%–20% multiplicity classes, while the amplitude of the $R_2^{(CD)}$ correlation decreases by a factor of two only. Clearly, the $P_2^{(CD)}$ correlation has a rather different sensitivity to charge creation than the $R_2^{(CD)}$ correlation.

D. Near-side peak widths

The presence of a relatively narrow near-side peak in R_2 and P_2 correlation functions indicates that the production of two particles (or more) at small relative azimuthal angle and pseudorapidity is substantially more probable than large-angle emission. Such narrowly focused emission may in principle be produced by in-flight decays of highly boosted resonances or clusters, jet fragmentation, or string (or color tube) fragmentation [30–34,44,45,93]. However, these different production mechanisms feature distinct p_T dependencies and may thus produce noticeable differences in the structures of the R_2 and P_2 correlation functions. Comprehensive particle-production models should in principle enable detailed calculations of the shape and strength of $R_2^{(CI)}$, $R_2^{(CD)}$, $P_2^{(CI)}$, and $P_2^{(CD)}$ to be compared with two-dimensional distributions presented in this work. It is interesting, nonetheless, to extract simple characterizations of these distributions and consider their multiplicity dependence in Pb-Pb and p-Pb collisions.

Measurements of the evolution of the width of the distributions with increasing multiplicity, in particular, are of interest given that variations of the widths might reflect important changes in the underlying particle-production mechanisms [36,37,40]. To enable comparisons with previous works (e.g., balance function) [59,62], we proceed to determine the longitudinal and azimuthal means as well as the rms widths of the measured correlation functions in terms of the moments $\langle \Delta\eta^k \rangle$ and $\langle \Delta\varphi^k \rangle$, with $k = 1, 2$, calculated according to

$$\langle \Delta\eta^k \rangle = \frac{\sum_{\Delta\eta_{\min}}^{\Delta\eta_{\max}} [O(\Delta\eta_i, \Delta\varphi_i) - O_{\text{off}}] \Delta\eta_i^k}{\sum_{\Delta\eta_{\min}}^{\Delta\eta_{\max}} [O(\Delta\eta_i, \Delta\varphi_i) - O_{\text{off}}]}, \tag{15}$$

$$\langle \Delta\varphi^k \rangle = \frac{\sum_{\Delta\varphi_{\min}}^{\Delta\varphi_{\max}} \left[O\left(\Delta\varphi_i, \Delta\varphi_i^k\right) - O_{\text{off}}\right] \Delta\varphi_i^k}{\sum_{\Delta\varphi_{\min}}^{\Delta\varphi_{\max}} [O(\Delta\varphi_i, \Delta\varphi_i) - O_{\text{off}}]}, \tag{16}$$

where $O(\Delta\eta_i, \Delta\varphi_i)$ represents values of the correlation functions $R_2^{(CI)}$, $R_2^{(CD)}$, $P_2^{(CI)}$, or $P_2^{(CD)}$ for the relative pseudorapidity bin $\Delta\eta_i$ (azimuthal angle $\Delta\varphi_i$). For $k = 1$, the summations are carried out one-sided, i.e., from $\Delta\eta_{\min} = 0$ ($\Delta\varphi_{\min} = 0$) to maximum values $\Delta\eta_{\max}$ ($\Delta\varphi_{\max}$), while for $k = 2$, the

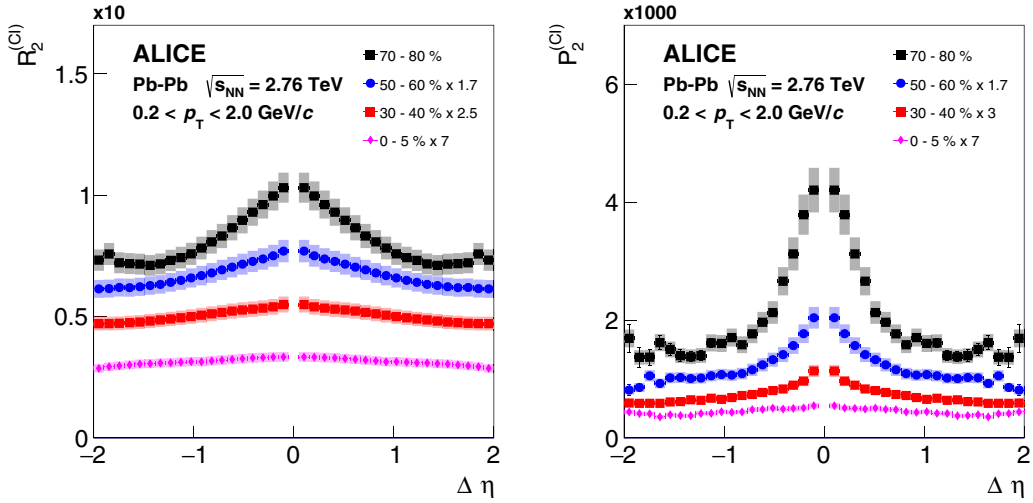

FIG. 10. Projections of $R_2^{(CI)}$ and $P_2^{(CI)}$ correlation functions, measured in Pb-Pb collision at $\sqrt{s_{NN}} = 2.76$ TeV, for selected ranges of collision centrality. Projections onto the $\Delta\eta$ axis are calculated as averages of the two-dimensional correlations in the range $|\Delta\varphi| \leqslant \pi$. Vertical bars and shaded areas represent statistical and systematic uncertainties, respectively.

summations are carried two-sided, i.e., in the range $-\Delta\eta_{max} \leqslant \Delta\eta \leqslant \Delta\eta_{max}$ $(-\Delta\varphi_{max} \leqslant \Delta\varphi \leqslant \Delta\varphi_{max})$. For $\langle\Delta\eta^k\rangle$ calculations, $\Delta\eta_{max}$ is chosen either at the edge of the acceptance or at $\Delta\eta$ values where the correlation functions reach a plateau (most particularly in the case of CD correlations) to avoid undue accumulation of noise in the calculation of the moments. For $\langle\Delta\varphi^k\rangle$ calculations, the upper edge of the range is set to $\Delta\varphi_{max} = \pi$ for $R_2^{(CD)}$ correlations and whichever values the $\Delta\varphi$ projections reach a minimum, in the case of $P_2^{(CD)}$ correlations. Offsets O_{off} are nominally used to eliminate trivial dependencies of the averages on the width of the experimental acceptance. For calculations of $\langle\Delta\varphi^k\rangle$, offsets O_{off} are determined by taking a three-bin average near $\Delta\varphi = \pi$, while for calculations of $\langle\Delta\eta^k\rangle$, offsets O_{off} are evaluated near the edge of the acceptance $\Delta\eta \sim 2$. However, in the case of $R_2^{(CD)}$, since the correlation is vanishing for large $|\Delta\eta|$ values, one uses a null offset. In this case, contributions to $\langle\Delta\eta^k\rangle^{1/k}$ from the unobserved part of $R_2^{(CD)}$, i.e., beyond the acceptance, are then neglected. Moments $\langle\Delta\eta^k\rangle$ and $\langle\Delta\varphi^k\rangle$ are determined on the basis of projections of the $R_2^{(CI)}$, $R_2^{(CD)}$, $P_2^{(CI)}$, or $P_2^{(CD)}$ correlation functions onto the $\Delta\eta$ and $\Delta\varphi$ axes, respectively. Projections onto $\Delta\eta$ are calculated in the range $|\Delta\varphi| \leqslant \pi$, whereas the projections onto $\Delta\varphi$ are determined in the range $|\Delta\eta| \leqslant 1.8$ for R_2 correlations and $|\Delta\eta| \leqslant 1$ for P_2 correlations, also to suppress accumulation of statistical noise. Only $\Delta\eta$ projections and the corresponding moments $\langle\Delta\eta^k\rangle$ are considered in the case of $R_2^{(CI)}$ and $P_2^{(CI)}$ given that these correlation functions feature strong azimuthal modulations. Projections of the $R_2^{(CI)}$, $R_2^{(CD)}$, $P_2^{(CI)}$, or $P_2^{(CD)}$ correlation functions are shown in Figs. 10–15. They have been divided by the number of integrated bins and scaled for ease of comparison.

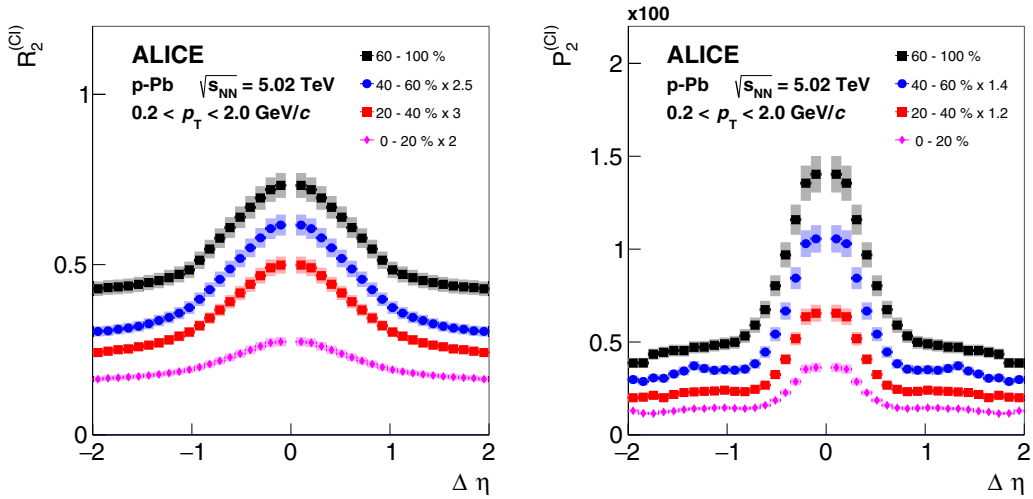

FIG. 11. Projections of $R_2^{(CI)}$ and $P_2^{(CI)}$ correlation functions, measured in p-Pb collisions at $\sqrt{s_{NN}} = 5.02$ TeV, for selected multiplicity classes. Projections onto the $\Delta\eta$ axis are calculated as averages of the two-dimensional correlations in the range $|\Delta\varphi| \leqslant \pi$. Vertical bars and shaded areas represent statistical and systematic uncertainties, respectively.

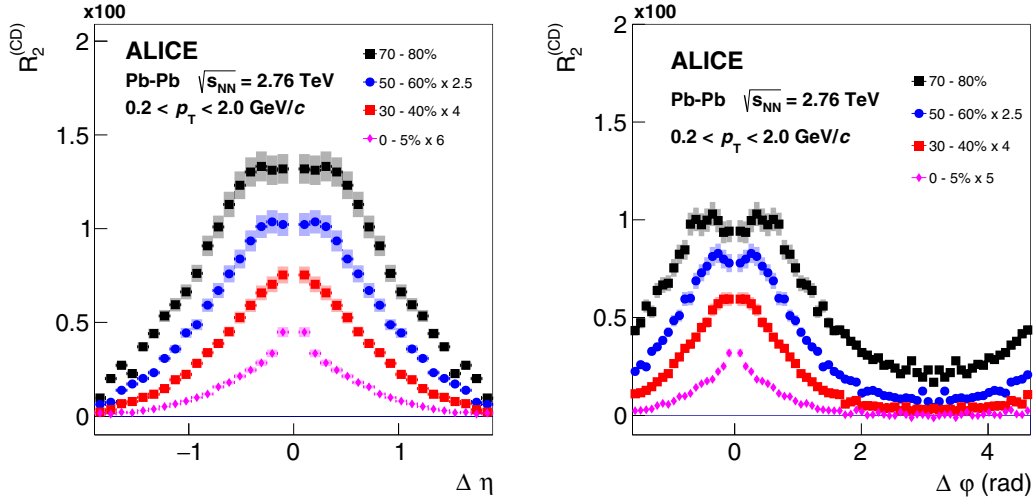

FIG. 12. Projections of $R_2^{(CD)}$ correlation functions, measured in Pb-Pb collision at $\sqrt{s_{NN}} = 2.76$ TeV, for selected ranges of collision centrality. The $\Delta\eta$ and $\Delta\varphi$ projections are calculated as averages of the two-dimensional correlations in the ranges $|\Delta\varphi| \leqslant \pi$ and $|\Delta\eta| \leqslant 1.8$, respectively. Vertical bars and shaded areas represent statistical and systematic uncertainties, respectively.

The longitudinal widths of the near-side peaks of $R_2^{(CI)}$ and $P_2^{(CI)}$ correlation functions are presented in Figs. 16 and 17 as a function of collision centrality and multiplicity class, respectively, while the longitudinal and azimuthal widths of near-side peak of $R_2^{(CD)}$ and $P_2^{(CD)}$ are displayed in Figs. 18–21.

The widths $\langle\Delta\eta^k\rangle^{1/k}$ of $R_2^{(CI)}$ (Fig. 16) grow monotonically in Pb-Pb collisions from 70%–80% to 0%–5% multiplicity classes, reaching a maximum in the 5% most-central collisions. A similar monotonic increase is observed for P_2, except for the 70%–80% multiplicity class. By contrast, in p-Pb collisions (Fig. 17), the longitudinal widths of the near-side peak of $R_2^{(CI)}$ and $P_2^{(CI)}$ have rather weak dependence, if any, on multiplicity. These different dependencies may in part be attributed to diffusion processes, expected to play a larger role in the longer-lived systems created in more-central Pb-Pb collisions [46,110]. However, the formation of long-range color tubes or strings compounded with radial flow may also play an important role in the observed longitudinal broadening of the near-side peak of the $R_2^{(CI)}$ and $P_2^{(CI)}$ correlation functions [111]. Interestingly, the longitudinal widths $\langle\Delta\eta^k\rangle^{1/k}$ observed for $P_2^{(CI)}$ are significantly smaller than those observed for $R_2^{(CI)}$ in both Pb-Pb and p-Pb collisions. Charge-dependent correlation functions are expected to have a different sensitivity to particle correlations than charge-independent correlations. This is readily verified in Figs. 18–21, which display the near-side peak width of CD correlations, measured in both Pb-Pb and p-Pb, as a function of produced-particle multiplicity classes. One finds that, in contrast with CI correlations whose near-side peaks width increase with

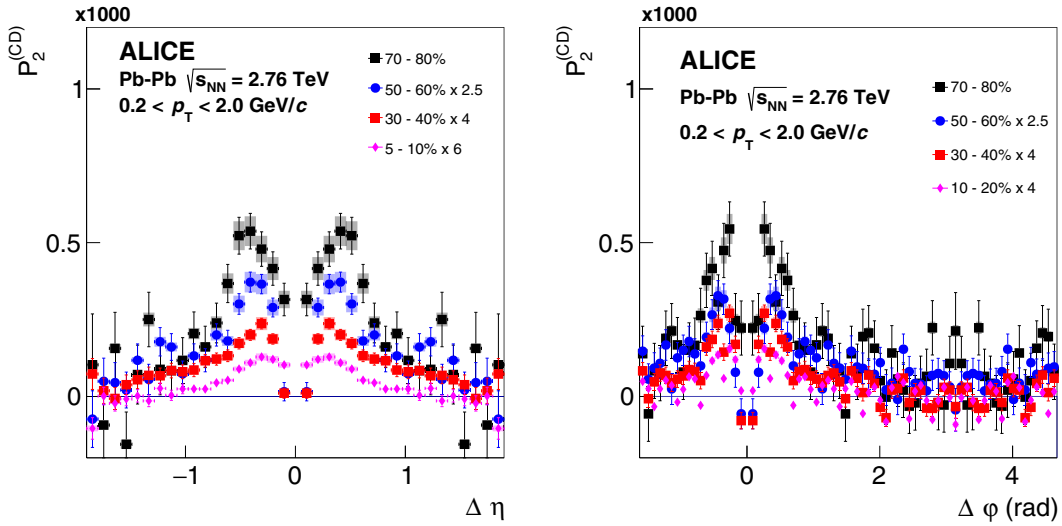

FIG. 13. Projections of $P_2^{(CD)}$ correlation functions, measured in Pb-Pb collision at $\sqrt{s_{NN}} = 2.76$ TeV, for selected ranges of collision centrality. The $\Delta\eta$ and $\Delta\varphi$ projections are calculated as averages of the two-dimensional correlations in the ranges $|\Delta\varphi| \leqslant \pi$ and $|\Delta\eta| \leqslant 1.8$, respectively. Vertical bars and shaded areas represent statistical and systematic uncertainties, respectively.

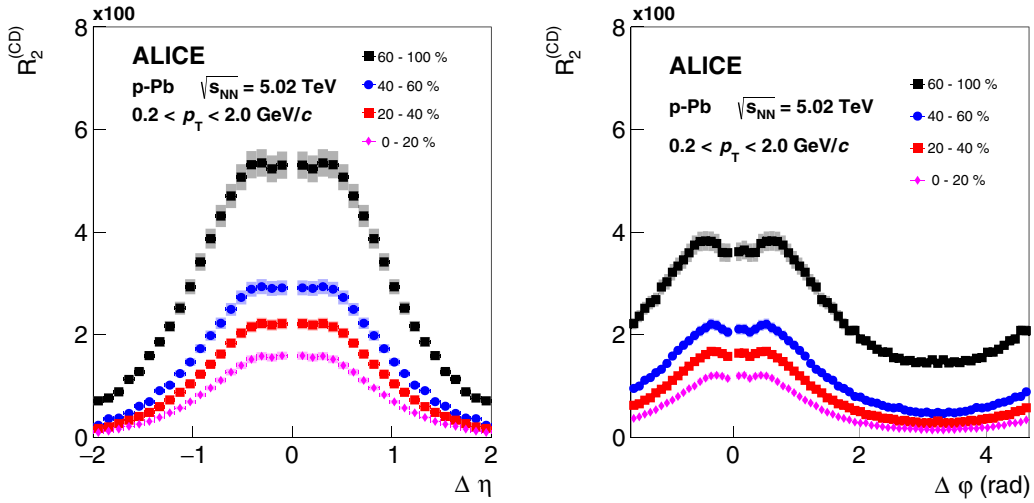

FIG. 14. Projections of $R_2^{(CD)}$ correlation functions, measured in p-Pb collision at $\sqrt{s_{NN}} = 5.02$ TeV, for selected multiplicity classes. The $\Delta\eta$ and $\Delta\varphi$ projections are calculated as averages of the two-dimensional correlations in the ranges $|\Delta\varphi| \leqslant \pi$ and $|\Delta\eta| \leqslant 1.8$, respectively. Vertical bars and shaded areas represent statistical and systematic uncertainties, respectively.

produced-particle multiplicity, the widths of the near-side peak of $R_2^{(CD)}$ correlation functions monotonically decrease with increasing multiplicity.

The widths measured in this work, shown with solid blue circles for $k = 2$ (rms) and open blue circles for $k = 1$ (one-sided mean) in Figs. 18 and 20, are compared with rms values of the longitudinal and azimuthal widths, shown in red, of the balance function reported by the ALICE collaboration [62]. One observes that the rms widths, $\langle\Delta\eta^2\rangle^{1/2}$, obtained in this work are in very good agreement with the longitudinal rms values reported for the balance function. A similar trend with collision centrality is observed for the rms width, $\langle\Delta\varphi^2\rangle^{1/2}$, albeit with a finite offset owing to differences in the rms calculation methods used in this and the prior work. In this work, an offset, evaluated at the minimum of the $\Delta\varphi$ projection is used and the rms calculation is performed in the range $-\pi \leqslant \Delta\varphi \leqslant \pi$, whereas the widths reported in Ref. [62] were evaluated without the use of an offset and in the range $-\pi/2 \leqslant \Delta\varphi \leqslant \pi/2$.

The $R_2^{(CD)}$ distributions measured in Pb-Pb exhibit a strong reduction from peripheral to central while the widths measured in p-Pb show a weaker but nonetheless noticeable reduction with increased charged-particle production. Multiplicity class dependencies of the widths of the near-side peak of $P_2^{(CD)}$ correlations are more difficult to assess owing to larger statistical and systematic uncertainties: measurements in Pb-Pb are consistent with a modest decrease with increasing collision centrality, whereas those in p-Pb suggest a reverse trend.

The reductions of the longitudinal and azimuthal widths of the near-side peak of $R_2^{(CD)}$ observed in Pb-Pb and p-Pb collisions are in agreement with prior measurements (both

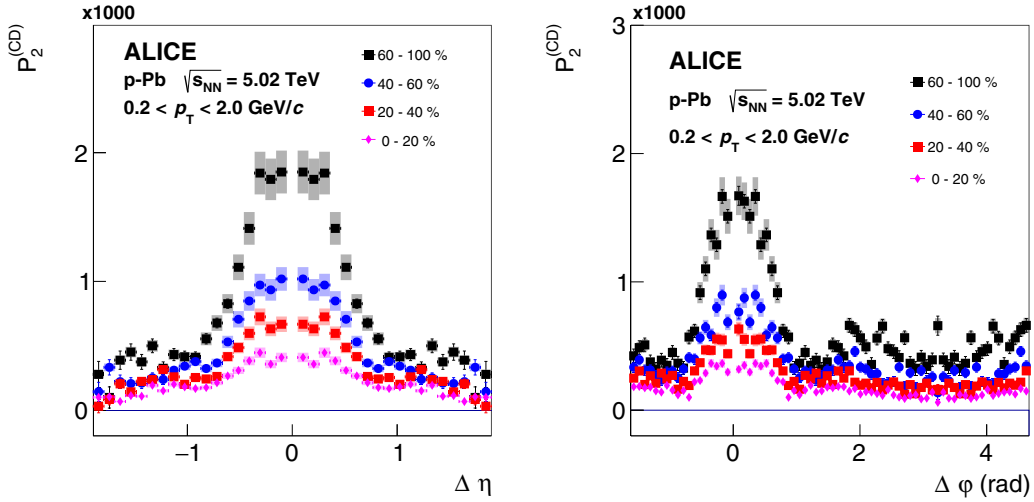

FIG. 15. Projections of $P_2^{(CD)}$ correlation functions, measured in p-Pb collision at $\sqrt{s_{NN}} = 5.02$ TeV, for selected multiplicity classes. The $\Delta\eta$ and $\Delta\varphi$ projections are calculated as averages of the two-dimensional correlations in the ranges $|\Delta\varphi| \leqslant \pi$ and $|\Delta\eta| \leqslant 1.8$, respectively. Vertical bars and shaded areas represent statistical and systematic uncertainties, respectively.

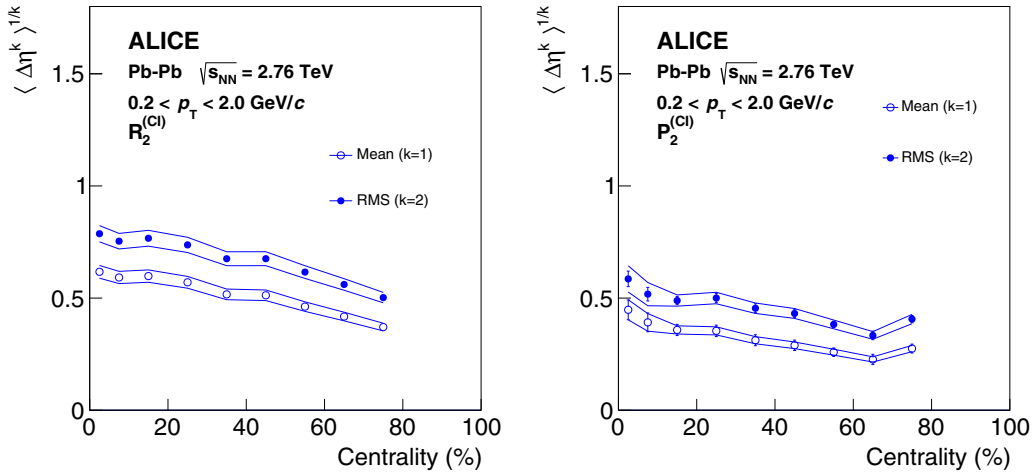

FIG. 16. Width of the near-side peak of $R_2^{(CI)}$ (left) and $P_2^{(CI)}$ (right) correlation functions along $\Delta\eta$ measured in Pb-Pb collisions as a function of the collision centrality class. Vertical bars and solid lines represent statistical and systematic uncertainties, respectively.

at RHIC and LHC) and are qualitatively consistent with the presence of strong radial flow and the existence of two-stage emission in these collisions, particularly in Pb-Pb collisions. However, one must also consider the role of diffusion processes, which for longer system lifetimes, would produce a broadening of the $R_2^{(CD)}$ correlations. Traditional collision-centrality-dependent analyses of the width of balance functions or $R_2^{(CD)}$ do not readily enable separation of the diffusion process, radial flow, and two-stage hadronization. However, the longitudinal (rapidity) expansion of the system might provide a useful clock towards the evaluation of azimuthal diffusion processes. As the system expands longitudinally, scatterings within the QGP phase would produce a progressive broadening of the CD correlation functions in $\Delta\varphi$. It thus becomes of interest to study whether there is evidence for larger diffusion at progressively wider $\Delta\eta$ separations. Figures 22 and 23 display the azimuthal rms width, $\langle\Delta\varphi^2\rangle^{1/2}$, measured in selected collision centrality ranges (Pb-Pb) and multiplicity classes (p-Pb), as a function of the pair separation $\Delta\eta$. First note that in both p-Pb and peripheral Pb-Pb collisions, the presence of a strong HBT component leads to small or even negative values of $R_2^{(CD)}$ and $P_2^{(CD)}$ at short pair separations in $\Delta\eta$ thereby creating a depletion near $\Delta\eta,\ \Delta\varphi = 0$ in plots of this correlator vs $\Delta\eta,\ \Delta\varphi$. This depression effectively pushes outward, in $\Delta\varphi$, the value of the azimuthal width of the distribution thereby leading to enhanced values of $\langle\Delta\varphi\rangle$ for short pair separations (i.e., $\Delta\eta < 0.5$). However, the HBT contribution to $R_2^{(CD)}$ is very narrow and not resolved by this measurement in mid-to-central Pb-Pb collisions. It consequently does not appreciably contribute to the calculation of the $\Delta\varphi$ widths in the 0%–50% centrality interval. The width of $R_2^{(CD)}$ in these mid-to-central collisions is thus believed to be dominated by charge-conserving particle-production processes and the evolution dynamics of the collision systems. In the 0%–5% and 30%–40% collision centralities, one finds that the rms width $\langle\Delta\varphi^2\rangle^{1/2}$ is in fact smallest at shortest pair separation and essentially monotonically grows with increasing pair separation. The growth for 0%–5% collisions can be approximately described with a function of the form $a + b\Delta\eta^{1/2}$ which suggests that the observed width dependence

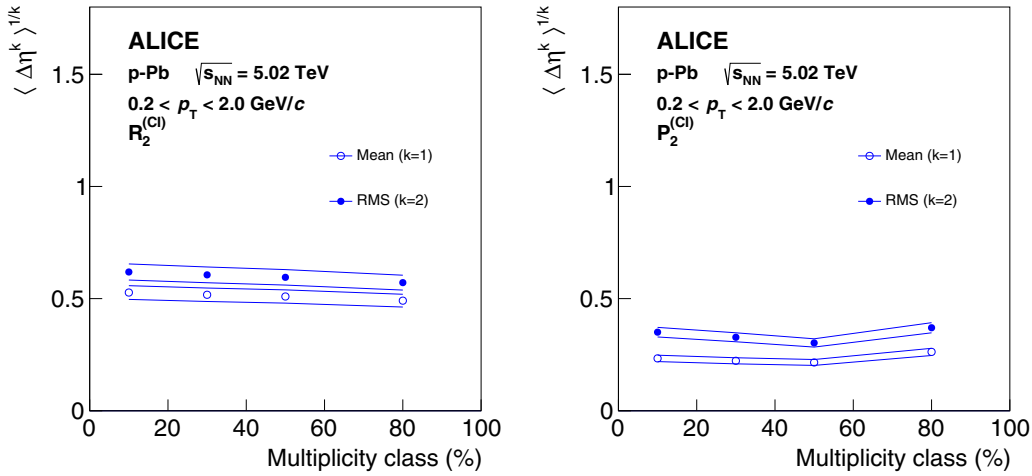

FIG. 17. Width of the near-side peak of $R_2^{(CI)}$ (left) and $P_2^{(CI)}$ (right) correlation functions along $\Delta\eta$ measured in p-Pb collisions as a function of produced-particle multiplicity class. Vertical bars and solid lines represent statistical and systematic uncertainties, respectively.

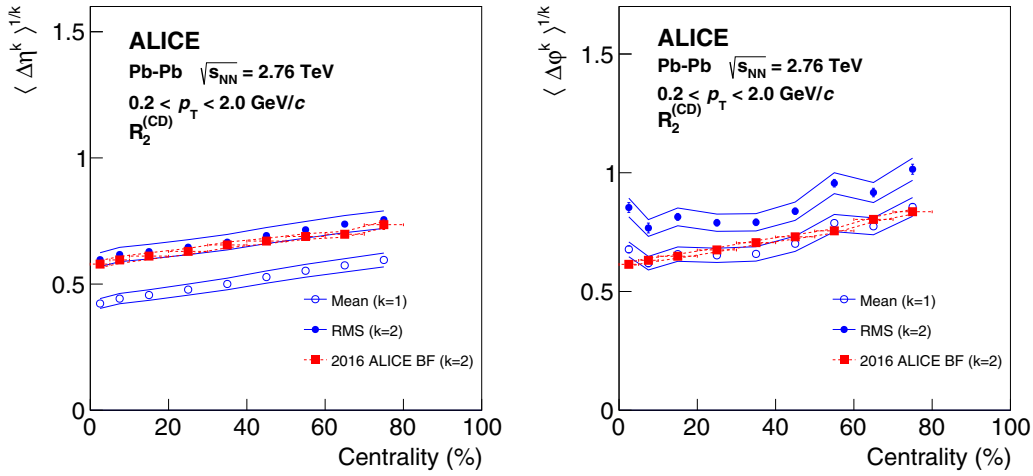

FIG. 18. Width of the near-side peak of $R_2^{(CD)}$ correlation functions along $\Delta\eta$ (left) and $\Delta\varphi$ (right) measured in Pb-Pb collisions as a function of collision centrality class. Vertical bars and solid lines represent statistical and systematic uncertainties, respectively. Mean and rms $\Delta\varphi$ widths (right; blue circles) were computed in the range $-\pi \leqslant \Delta\varphi \leqslant \pi$ with an offset according to Eq. (16). Red symbols show rms $\Delta\eta$ and $\Delta\varphi$ widths (systematic uncertainties shown as red dashed lines) reported by a prior ALICE analysis based on measurements of balance functions [62]. The $\Delta\varphi$ widths reported in this earlier work were computed in the range $-\pi/2 \leqslant \Delta\varphi \leqslant \pi/2$.

is compatible with a naive model of the diffusion process. Indeed, the azimuthal width of the correlation peak should qualitatively grow as the power $1/2$ of the lifetime of the system, i.e., $\tau^{1/2}$, which in turn should be roughly proportional to $\Delta\eta^{1/2}$ for sufficiently large separations. However, a fit with a linear function $a' + b'\Delta\eta$ produces a χ^2/dof of similar magnitude as the $\Delta\eta^{1/2}$ fit. It is thus not possible, with this measurement, to precisely assess the $\Delta\varphi$ broadening dependence on the pair separation in $\Delta\eta$. While the measured evolution of the $R_2^{(CD)}$ $\Delta\varphi$ width with pair separation might indicate the presence of diffusion processes, it might also be attributable to radial flow effects [112]. Hydrodynamic models of the evolution of heavy-ion collisions and blast-wave fits of Au-Au and Pb-Pb data reveal the presence of significant radial flow with velocity profiles dependent on the point of origin of the produced particles [113,114]. Given that balanced charged-particle pairs originate from a common production mechanism such as resonance decays or string fragmentation, the pair separation in $\Delta\eta$ and $\Delta\varphi$ is thus expected to decrease with the outward radial velocity of the source. Slow sources shall produce large pair separations in $\Delta\eta$ and $\Delta\varphi$, on average, while larger radial velocity will produce significantly smaller $\Delta\eta$ and $\Delta\varphi$ separations. In effect, differential flow profiles shall yield, overall, $\Delta\varphi$ widths that increase with the pair separation in $\Delta\eta$. The observed dependence of $\Delta\varphi$ widths on pair separation might then in part result from radial flow, diffusion, and possibly other effects [112]. A proper assessment of these contributions shall thus require model studies beyond the scope of this work.

E. Fourier decompositions of R_2 and P_2 correlation functions

Correlation analyses based on multiparticle cumulants, including the scalar-product, Q distribution, Lee-Yang

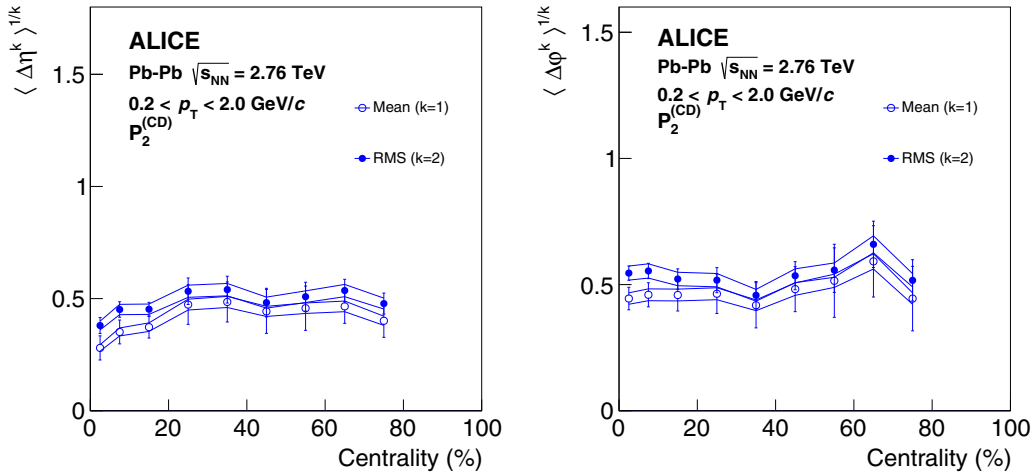

FIG. 19. Width of the near-side peak of $P_2^{(CD)}$ correlation functions along $\Delta\eta$ (left) and $\Delta\varphi$ (right) measured in Pb-Pb collisions as a function of collision centrality class. Vertical bars and solid lines represent statistical and systematic uncertainties, respectively.

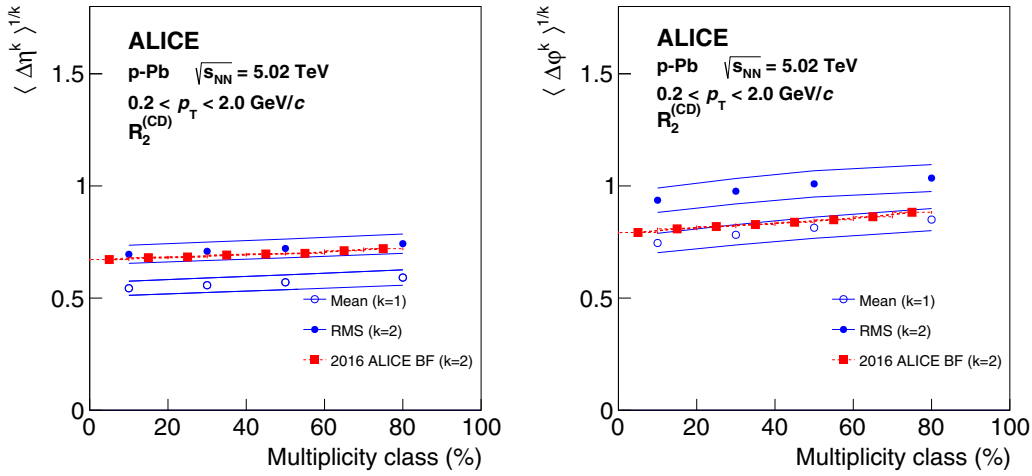

FIG. 20. Width of the near-side peak of $R_2^{(CD)}$ correlation functions along $\Delta\eta$ (left) and $\Delta\varphi$ (right) measured in p-Pb collisions as a function of produced-particle multiplicity class. Vertical bars and solid lines represent statistical and systematic uncertainties, respectively. Mean and rms $\Delta\varphi$ widths (right; blue circles) were computed in the range $-\pi \leqslant \Delta\varphi \leqslant \pi$ with an offset according to Eq. (16). Red symbols show rms $\Delta\eta$ and $\Delta\varphi$ widths (systematic uncertainties shown as red dashed lines) reported by a prior ALICE analysis based on measurements of balance functions [62]. The $\Delta\varphi$ widths reported in this earlier work were computed in the range $-\pi/2 \leqslant \Delta\varphi \leqslant \pi/2$.

zeros, and Fourier-Bessel transforms methods, have established the presence of strong collective anisotropic flow in Au-Au and Pb-Pb collisions [1,2,4,8,81], and recent multiparticle correlation analyses suggest that collective behavior might also play an important role in p-Pb and pp collisions [83,95,115–121]. However, noncollective particle-production mechanisms, including resonance decays, jets, and other nonflow effects, are also known to contribute to correlation functions, particularly at small particle pair separation in (pseudo)rapidity and in small collision systems. One studies the interplay of flow and nonflow effects by carrying out Fourier decomposition of the $\Delta\varphi$ dependence of $R_2(\Delta\eta, \Delta\varphi)$ and $P_2(\Delta\eta, \Delta\varphi)$ as a function of the pair separation $|\Delta\eta|$. Flow coefficients $v_n[R_2]$ and $v_n[P_2]$, calculated according to Eqs. (10) and (11), are reported for Pb-Pb collisions, whereas harmonic coefficients $b_n[R_2]$ and $b_n[P_2]$ are reported for p-Pb collisions.

Figure 24 presents the v_n coefficients, $n = 2, 3, 4$, (defined in Sec. IV B) plotted as a function of Pb-Pb collision centrality, obtained from projections of $R_2^{(US)}$ and $R_2^{(LS)}$, in the ranges $0.2 \leqslant |\Delta\eta| \leqslant 0.9$ and $0.9 \leqslant |\Delta\eta| \leqslant 1.9$. One observes that the $v_n[R_2]$ coefficients obtained from US and LS correlations are essentially identical at "large" $|\Delta\eta|$ (i.e., $|\Delta\eta| \geqslant 0.9$). Aside from weak Coulomb distortions [57], one expects that two-particle correlations determined by collective behavior to be essentially independent of the charge of the particles. The near perfect agreement between LS and US Fourier coefficients of order two, three, and four is thus an indication that nonflow effects, which might exhibit explicit dependencies on charges, are rather weak for pair separations in excess of $|\Delta\eta| = 0.9$. The observed azimuthal coefficients at $|\Delta\eta| > 0.9$ are thus consistent with the dominance of collective flow effects in this range. The US and LS coefficients obtained for pairs with $0.2 \leqslant |\Delta\eta| \leqslant 0.9$, on the other hand, exhibit

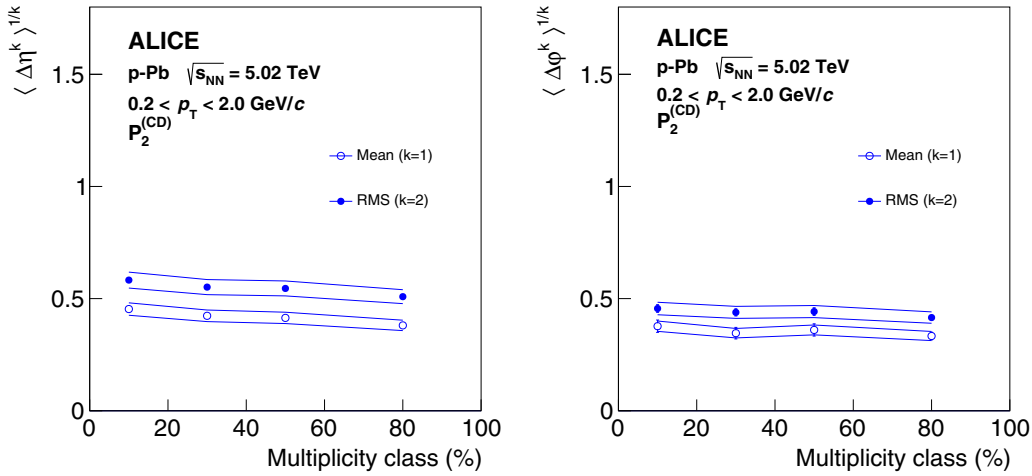

FIG. 21. Width of the near-side peak of $P_2^{(CD)}$ correlation functions along $\Delta\eta$ (left) and $\Delta\varphi$ (right) measured in p-Pb collisions as a function of produced-particle multiplicity class. Vertical bars and solid lines represent statistical and systematic uncertainties, respectively.

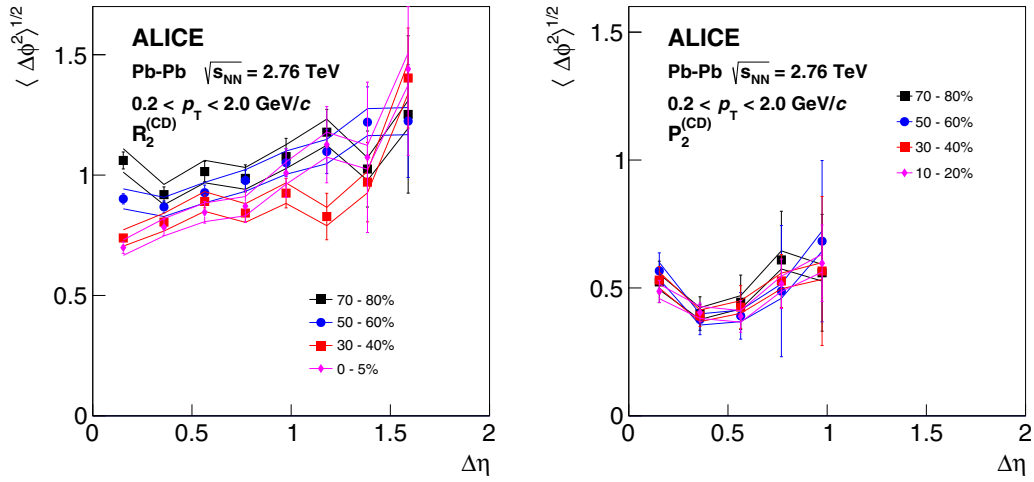

FIG. 22. Width of the near-side peak of $R_2^{(CD)}$ (left) and $P_2^{(CD)}$ (right) correlation functions along $\Delta\varphi$ measured in Pb-Pb collisions as a function of the $\Delta\eta$ pair separation for selected collision centralities. Vertical bars and solid lines represent statistical and systematic uncertainties, respectively.

systematic discrepancies at all collision centralities. Considering the ratio of US and LS coefficients plotted in the lower panel of Fig. 24, one observes that US v_n coefficients are systematically larger than those of LS pairs. One also finds that the v_2 coefficients exhibit the smallest differences, while the v_4 coefficients have the largest. This behavior is largely driven by the presence of the stronger near-side peak observed in US R_2 correlations, and is thus a result of nonflow effects associated with the creation of charge particle pairs.

Figure 25 compares $v_n[R_2^{(CI)}]$ coefficients, $n = 2, 3, 4$ (solid symbols), extracted from $R_2^{(CI)}$ correlation functions with flow coefficients $v_2\{2\}$ (open symbols) obtained with the scalar-product method according to Eq. (12). The comparison is carried out in Figs. 25(a) and 25(b) for charged-particle pairs with pseudorapidity separations of $0.2 \leqslant |\Delta\eta| \leqslant 0.9$ and $0.9 \leqslant |\Delta\eta| \leqslant 1.9$, respectively. Figures 25(c) and 25(d) display the ratio of coefficients obtained with the two methods. One observes that the deviations between the $v_2\{2\}$ and $v_n[R_2^{(CI)}]$ for $0.9 \leqslant |\Delta\eta| \leqslant 1.9$ are typically smaller than 2%, irrespective of collision centrality. Such small deviations are expected given that $v_2\{2\}$ coefficients were determined with a minimal $|\Delta\eta|$ of 0.9 units of pseudorapidity. The coefficients v_n obtained from $R_2^{(CI)}$, for pair separation in excess of 0.9, are thus equivalent to those obtained with the SP method. However, the deviations for pair separations in the range $0.2 \leqslant |\Delta\eta| \leqslant 0.9$ are finite in all centrality classes in Pb-Pb collisions. They are smallest in central-to-mid-central collisions but rise in excess of 10% in more-peripheral collisions, owing to the presence of the near-side peak that dominates the R_2 correlations in this collision centrality range.

Similarly to Fig. 24, Fig. 26 presents the v_n coefficients, $n = 2, 3, 4$, plotted as a function of Pb-Pb collision centrality, obtained from projections of $P_2^{(US)}$ and $P_2^{(LS)}$, in ranges $0.2 \leqslant |\Delta\eta| \leqslant 0.9$ and $0.9 \leqslant |\Delta\eta| \leqslant 1.9$. In this case also, one observes that US and LS v_n coefficients measured for

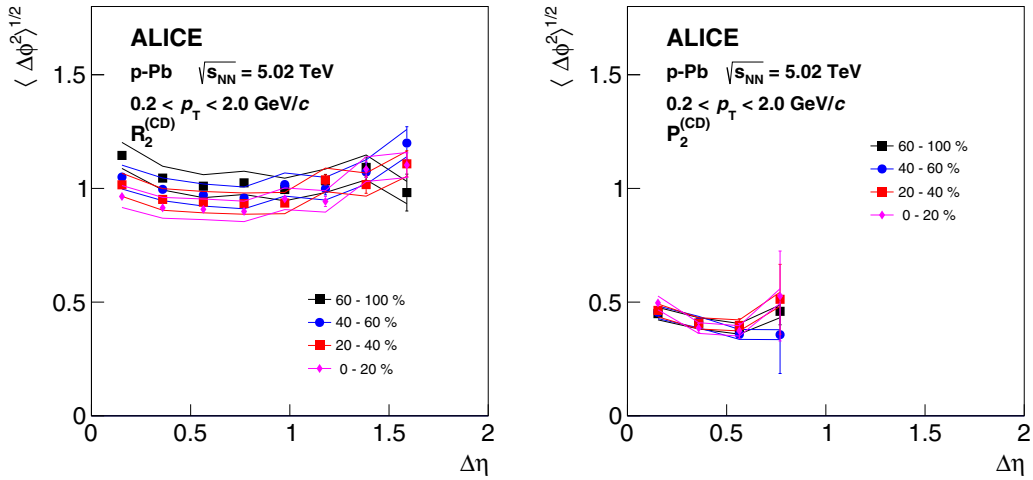

FIG. 23. Width of the near-side peak of $R_2^{(CD)}$ (left) and $P_2^{(CD)}$ (right) correlation functions along $\Delta\varphi$ measured in p-Pb collisions as a function of the $\Delta\eta$ pair separation for selected ranges of produced multiplicities. Vertical bars and solid lines represent statistical and systematic uncertainties, respectively.

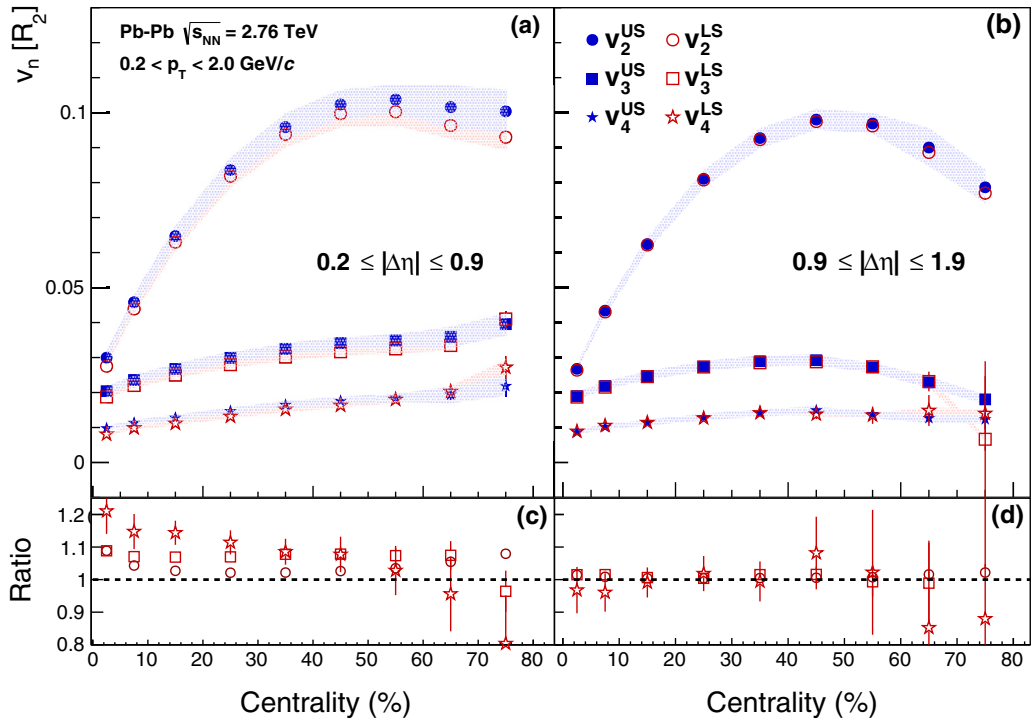

FIG. 24. Fourier coefficients v_n, with $n = 2, 3, 4$, extracted from US and LS R_2 correlation functions in the range $0.2 \leqslant |\Delta\eta| \leqslant 0.9$ and $0.9 \leqslant |\Delta\eta| \leqslant 1.9$ in panels (a) and (b), respectively. The ratios between US and LS v_n coefficients are shown in panels (c) and (d). Vertical bars and shaded areas represent statistical and systematic uncertainties, respectively.

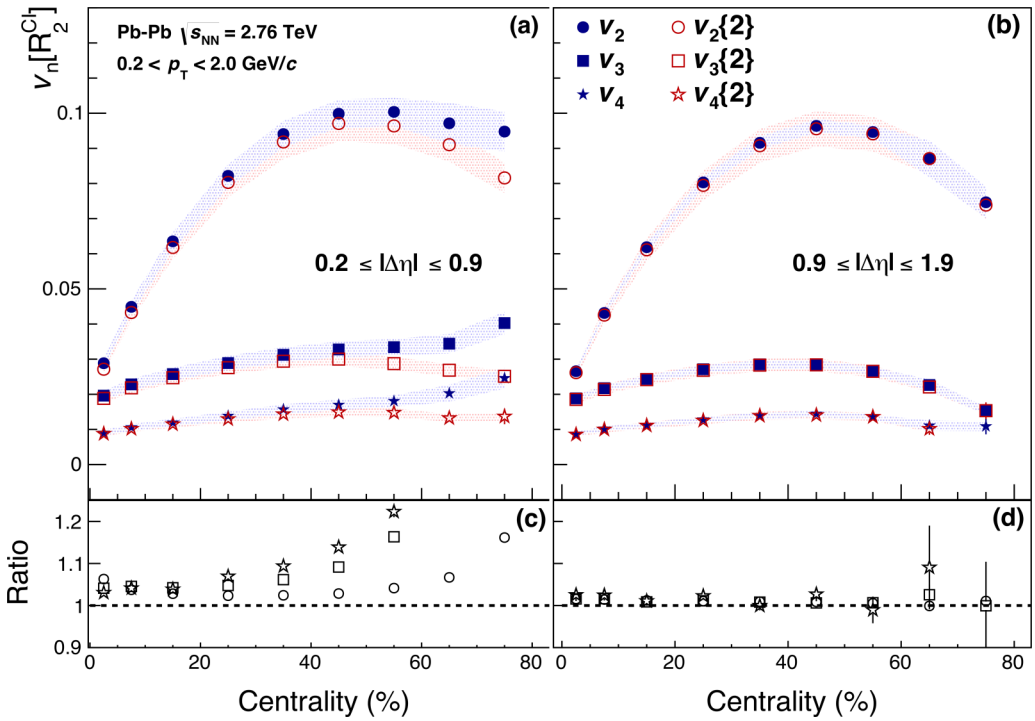

FIG. 25. Solid symbols: coefficients v_n, $n = 2, 3, 4$, obtained from Fourier decompositions of charge-independent correlators, $R_2^{(CI)}$, in the ranges $0.2 \leqslant |\Delta\eta| \leqslant 0.9$ (left) and $0.9 \leqslant |\Delta\eta| \leqslant 1.9$ (right). Open symbols: flow coefficients v_n obtained with the scalar-product method according to Eq. (12). (c), (d) Ratios of the coefficients v_n values obtained from $R_2^{(CI)}$ to those obtained with the scalar-product method. Vertical bars and shaded areas indicate statistical and systematic uncertainties, respectively.

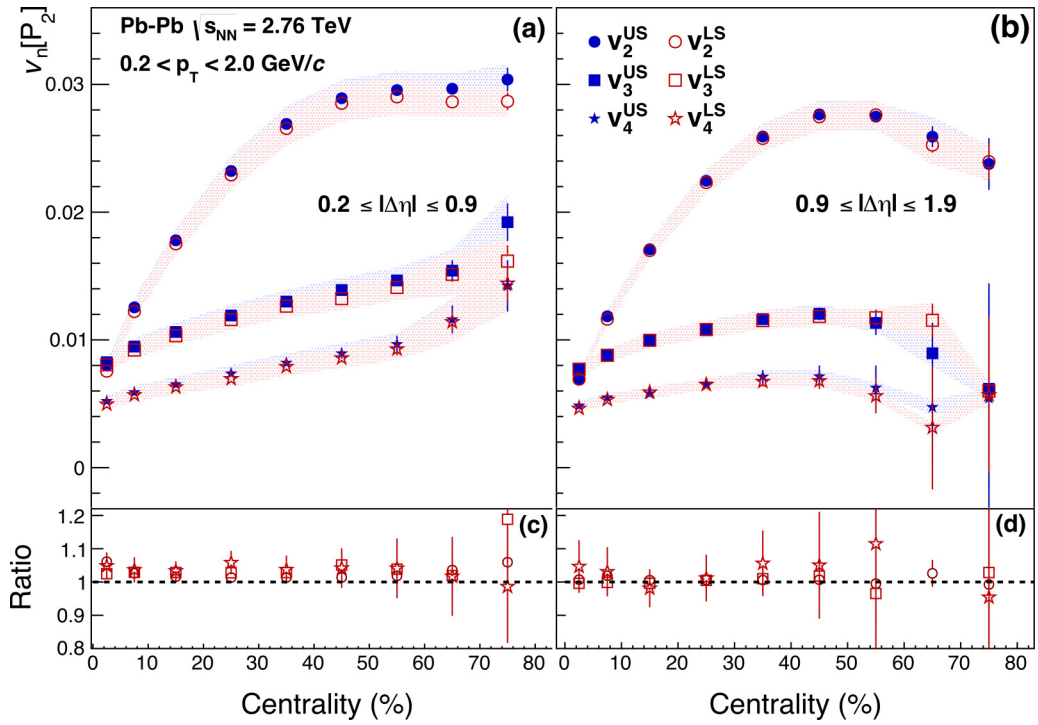

FIG. 26. Fourier coefficients with $n = 2, 3, 4$ obtained in P_2 for US and LS charge-correlations in the ranges (a) $0.2 \leqslant |\Delta\eta| \leqslant 0.9$ and (b) $0.9 \leqslant |\Delta\eta| \leqslant 1.9$. The ratios between US and LS v_n coefficients are shown in panels (c) and (d), respectively. Vertical bars and shaded areas indicate statistical and systematic uncertainties, respectively.

pairs in the range $0.9 \leqslant |\Delta\eta| \leqslant 1.9$ are essentially identical, whereas coefficients for US pairs in the range $0.2 \leqslant |\Delta\eta| \leqslant 0.9$ uniformly exceed those of LS by about 5% for $n = 2$, 3, and 4, and at all observed centralities.

Comparing the left and right panels of Figs. 24 and 26, one concludes that $v_n[R_2]$ and $v_n[P_2]$ coefficients exhibit a rather large dependence on the relative pseudorapidity of the pair. These deviations evidently arise because of nonflow effects manifested by the presence of the strong near-side peak centered at $\Delta\eta = 0$, $\Delta\varphi = 0$ observed in R_2 and P_2 correlations. One expects the impact of such nonflow effects on the magnitude of the v_n coefficients to weaken with pair separation.

This is explicitly verified by studying the magnitude of the coefficients as a function of pair separation, shown in Figs. 27 and 28 for 0%–5% and 70%–80% Pb-Pb collisions, respectively. One observes similar trends for $v_n[R_2]$ and $v_n[P_2]$, coefficients with $n = 2, 3$. The coefficient amplitudes are largest at $|\Delta\eta| \sim 0.2$ and decrease approximately linearly with increasing $|\Delta\eta|$ until they seemingly reach plateaus. Interestingly, one observes that the $v_n[P_2]$ coefficients reach their plateau at $|\Delta\eta| \sim 0.7$ in peripheral collisions ($|\Delta\eta| \sim 1$ in central collisions), while the $v_n[R_2]$ coefficients do not reach a plateau until $|\Delta\eta| \sim 1.2 - 1.3$ ($|\Delta\eta| \sim 1.5$ in central collisions). This numerical difference is evidently due to the fact that the near-side of P_2 distributions are significantly narrower than those of R_2 distributions, but it also shows that P_2 somehow features a smaller sensitivity to nonflow. Indeed, nonflow effects in P_2 appear to be limited to a narrower range of $\Delta\eta$. Were it not for the fact that high-precision analyses of P_2 require a larger dataset than those of R_2, the suppression of nonflow effects in flow studies might be better achieved by using $\Delta p_T \Delta p_T$-weighted observables rather than by using correlators simply based on the number of particles. The difference between the P_2 and R_2 coefficients evidently also provides a new perspective and tool to investigate the near-side peak of correlation functions and the nature and origin of nonflow effects.

The R_2 and P_2 correlation functions shown in Fig. 7 exhibit nontrivial structures and dependencies on $\Delta\varphi$. These may be due to a number of different particle production processes including resonance decays, coalescence of constituent quarks, string fragmentation, jets, and possibly several other mechanisms. In general, transverse anisotropies associated with hydrodynamic flow and differential attenuation of high-p_T particles by the anisotropic medium formed in p-Pb collisions are not readily expected in small collision systems such as those produced in the minimum-bias or low-multiplicity p-Pb collisions considered in this work. However, a number of recent works have reported evidence for collective motion in high-multiplicity p-Pb collisions. It is thus of interest and valuable to characterize the azimuthal dependence of the correlation R_2 and P_2 in terms of Fourier decompositions as a function of the relative pseudorapidity $|\Delta\eta|$ of measured particles. Given that nonflow effects are expected to dominate in minimum-bias p-Pb collisions, we report the coefficients b_n calculated according to Eq. (10) rather than flow coefficients v_n. These are determined based on projections of the R_2 and P_2 correlation functions onto $\Delta\varphi$ in several ranges of $|\Delta\eta|$. The coefficients' dependence on $|\Delta\eta|$ obtained from fits to the R_2 and P_2 projections are displayed in Figs. 29 and 30 for three different multiplicity classes.

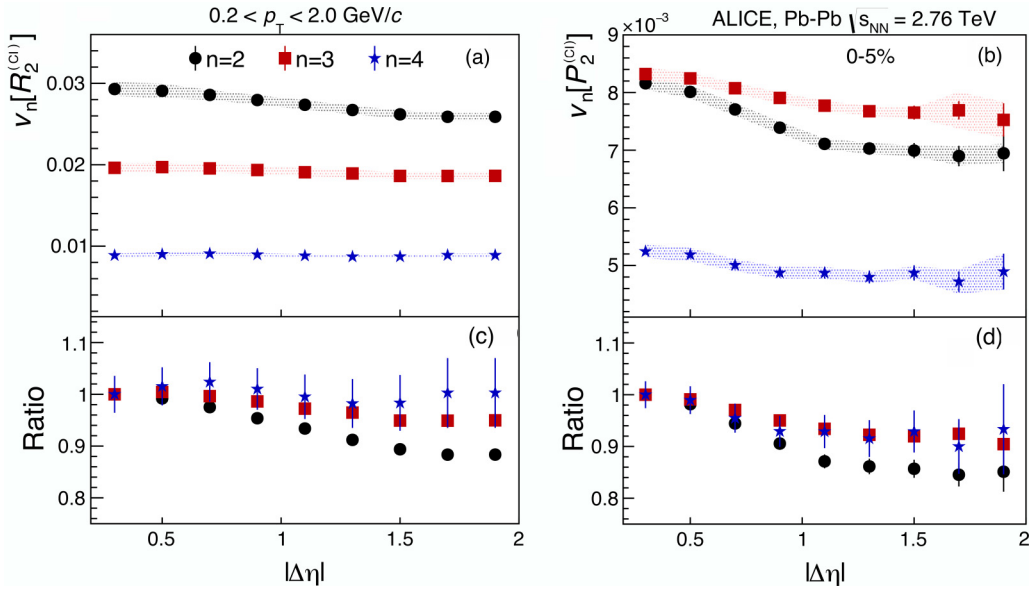

FIG. 27. (a) Pair separation $|\Delta\eta|$ dependence of Fourier coefficients $v_n[R_2^{(CI)}]$ and (b) $v_n[P_2^{(CI)}]$, with $n = 2, 3, 4$, obtained from $R_2^{(CI)}$ and $P_2^{(CI)}$ correlation functions in Pb-Pb 5% most-central collisions. (c), (d) Ratios of the coefficients to $v_n(|\Delta\eta|)$ to their respective values at $|\Delta\eta| = 0.3$. Vertical bars and shaded areas indicate statistical and systematic uncertainties, respectively. Reproduced from Ref. [108].

All in all, the coefficients b_n obtained from fits to the R_2 and P_2 correlation functions measured at selected multiplicity classes exhibit different dependencies on $|\Delta\eta|$. The long range (i.e., in $|\Delta\eta|$) of these correlation functions, in particular, is of interest to understand the role of nonflow effects in measurements of flow. Nonflow contributions (e.g., those associated with resonance decays, jets, and momentum conservation) are expected to decrease with increasing large $|\Delta\eta|$ gap. This can be verified quantitatively based on the Fourier decompositions of R_2 and P_2 reported in Figs. 31 and 32, where one observes that the coefficients b_n have decreasing amplitudes for increasing $|\Delta\eta|$. One notes, however, that the coefficient b_2 and coefficients of higher order, b_3 and b_4, exhibit qualitatively different dependencies on $|\Delta\eta|$. The higher-order coefficients decrease rapidly, within $|\Delta\eta| < 1.5(0.75)$ in $R_2^{(CI)}$ ($P_2^{(CI)}$) and become vanishingly small, within the statistical accuracy of this measurement, for larger values of $|\Delta\eta|$, whereas b_2 coefficients' reduction with increasing $|\Delta\eta|$

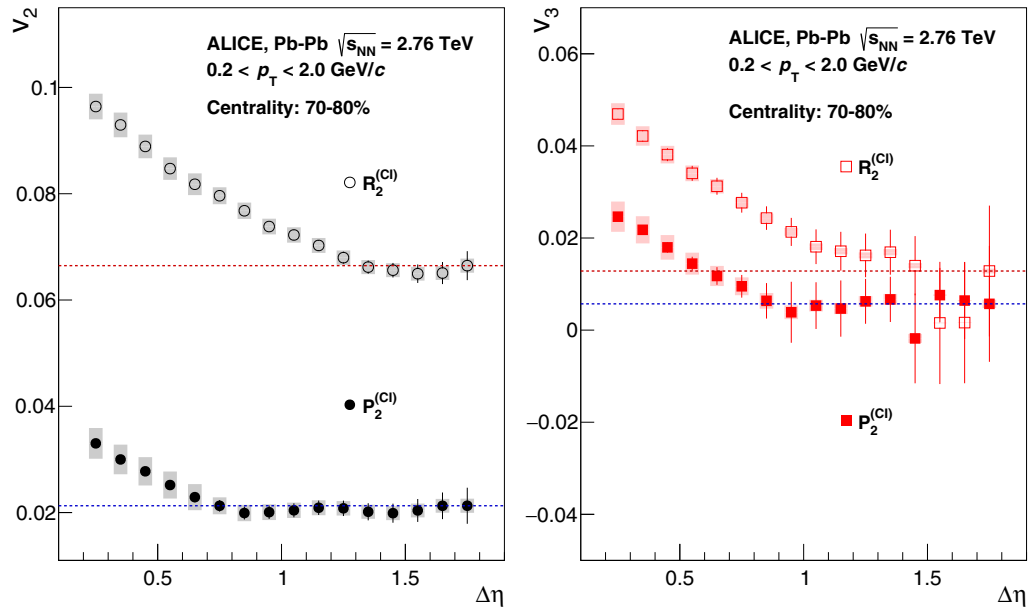

FIG. 28. Coefficients v_2 (left) and v_3 (right) as a function of $|\Delta\eta|$ obtained from P_2^{CI} and R_2^{CI} correlation functions in the 70%–80% centrality interval in Pb-Pb collisions. Dotted lines show baselines drawn at $v_n(|\Delta\eta| = 1.75)$. Vertical bars and shaded areas indicate statistical and systematic uncertainties, respectively.

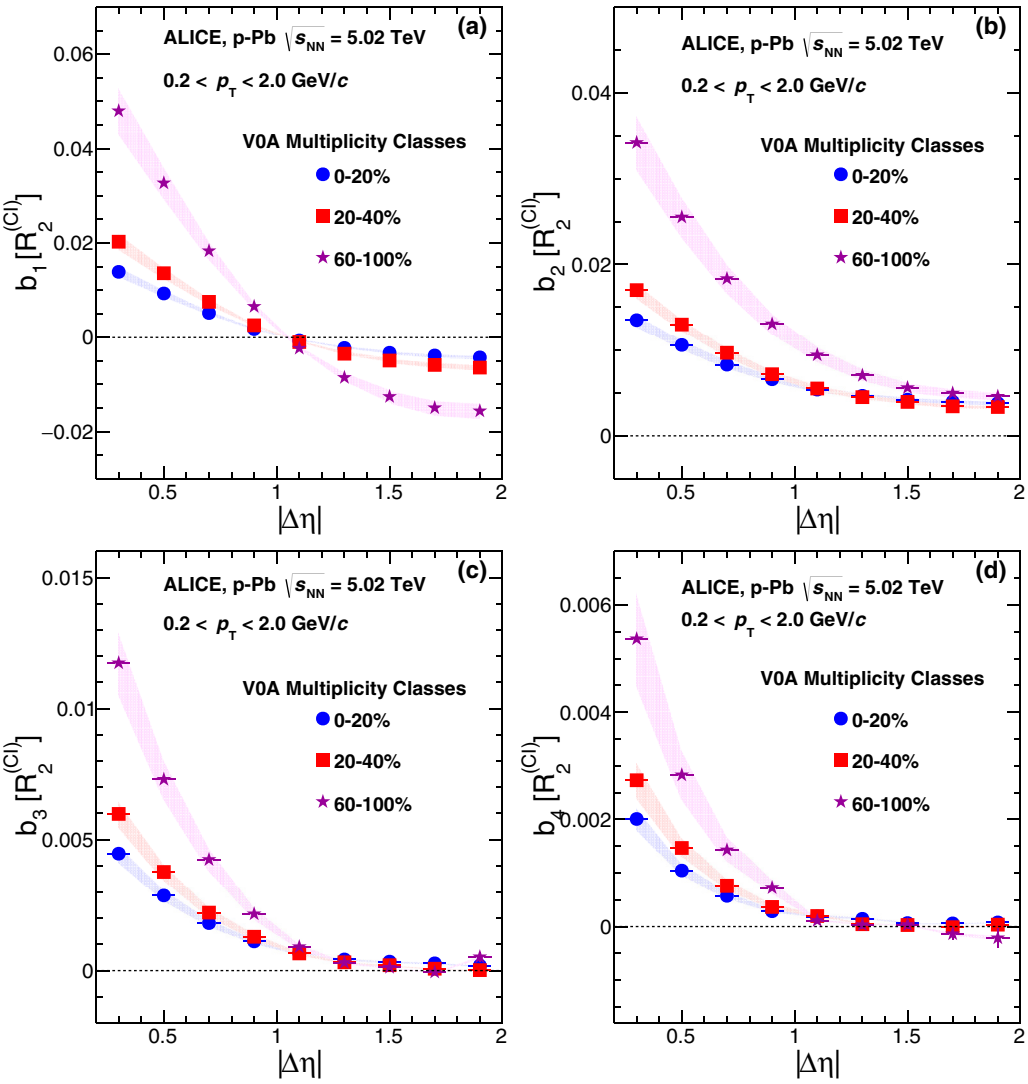

FIG. 29. Fourier coefficients, b_n, $n = 1, \ldots, 4$, extracted from $R_2^{(\mathrm{CI})}$ correlation functions measured in p-Pb collisions at $\sqrt{s_{\mathrm{NN}}} = 5.02$ TeV using three multiplicity classes. Vertical bars and shaded areas represent statistical and systematic uncertainties, respectively.

saturates and reach a constant value beyond $|\Delta\eta| \sim 1.5(0.75)$. One compares the evolution of $b_n[R_2]$ and $b_n[P_2]$ coefficients with $|\Delta\eta|$ in more detail. The coefficients $b_1[R_2]$ measured in all three multiplicity classes, shown in Fig. 29(a), exhibit a monotonic dependence on $|\Delta\eta|$, decreasing from positive values at $|\Delta\eta| = 0.2$ to negative values at $|\Delta\eta| = 1.9$, and crossing the axis (zero amplitude) at $|\Delta\eta| = 1.0$. The positive values at $|\Delta\eta| \leqslant 0.9$ are determined by the presence of the strong near-side peak, whereas negative values observed at large $|\Delta\eta|$ likely result from momentum-conservation effects. The coefficients $b_1[P_2]$, shown in Fig. 30(a), exhibit similar monotonic trends as the $b_1[R_2]$ coefficients, with positive and negative values at short and large $|\Delta\eta|$ ranges, respectively, but their $|\Delta\eta|$ dependence crosses the axis and thus appear to vanish at approximately $|\Delta\eta| = 0.6$ rather than at the larger value $|\Delta\eta| = 1.0$ observed in the case of the R_2 correlations. The lower crossing point, $|\Delta\eta| = 0.6$, evidently results from the much narrower near-side peaks observed in P_2 correlations relative to those found in the R_2 distributions.

One next considers graphs of b_n, $n \geqslant 2$, shown in Figs. 29(b)–29(d) and 30(b)–30(d), extracted from $R_2^{(\mathrm{CI})}$ and $P_2^{(\mathrm{CI})}$ distributions. One finds that similarly to b_1 coefficients, the $b_n[R_2]$ and $b_n[P_2]$ coefficients all exhibit decreasing monotonic trends with increasing $|\Delta\eta|$. However, these coefficients remain positive in all three multiplicity classes and at all values of $|\Delta\eta|$, except for a few negative values of the b_3 and b_4 coefficients observed at large $|\Delta\eta|$, which given their statistical accuracy are consistent with positive values. One notes, additionally, that the magnitude of the $b_n[R_2]$ coefficients decreases much slower with increasing $|\Delta\eta|$ than the amplitude of the $b_n[P_2]$ coefficients. Indeed, the $b_2[R_2]$ coefficients appear to drop to a minimum value at $|\Delta\eta| = 1.5 - 1.6$ while $b_2[P_2]$ clearly reaches a plateau near $|\Delta\eta| = 0.6$–0.7. The third-order coefficients exhibit similar behavior, albeit, asymptotically reaching much smaller values. The coefficient

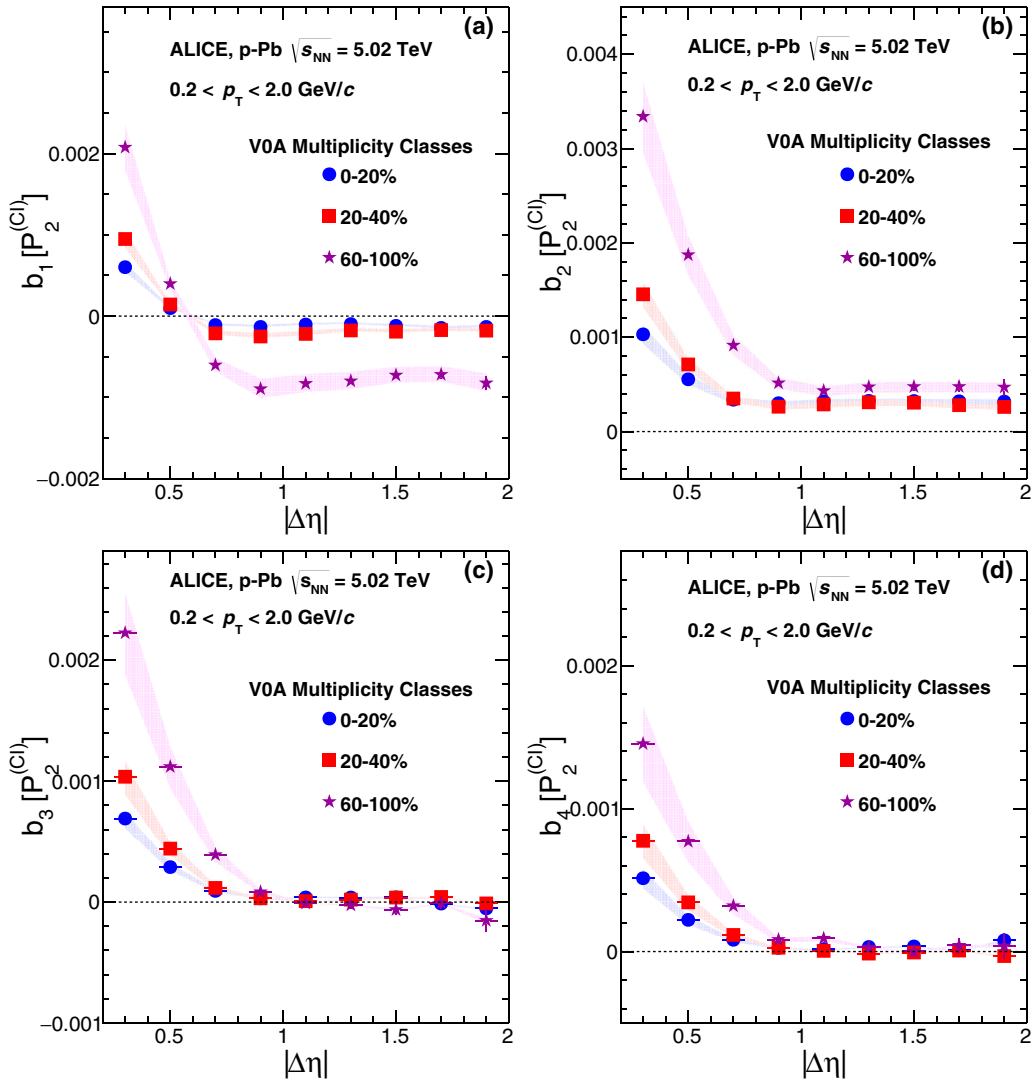

FIG. 30. Fourier coefficients, b_n, $n = 1, \ldots, 4$, extracted from $P_2^{(CI)}$ correlation functions measured in p-Pb collisions at $\sqrt{s_{NN}} = 5.02$ TeV using three multiplicity classes. Vertical bars and shaded areas represent statistical and systematic uncertainties, respectively.

$b_3[P_2]$ clearly plateaus beyond $|\Delta\eta| = 0.6$–0.7 while $b_3[R_2]$ is not clearly plateaued at $|\Delta\eta| = 1.8$. Similar trends are qualitatively observed with the b_4 coefficients within statistical uncertainties.

Overall, one finds that the $|\Delta\eta|$ dependence of the b_n coefficients extracted in p-Pb collisions for R_2 and P_2 correlation functions is rather similar to the evolution of the v_n coefficients with $|\Delta\eta|$ observed in Pb-Pb collisions. Both sets of coefficients feature large values at small pair separations, decrease for increasing $|\Delta\eta|$, and tend to plateau at approximately $|\Delta\eta| \sim 0.6$–0.7 in P_2 and $|\Delta\eta| \sim 1.5$ in R_2. The nonflow component associated with the near-side peak is thus found to be suppressed in the case of P_2 for pair separations $0.7 < |\Delta\eta| < 1.5$, implying that $\Delta p_T \Delta p_T$ averages to zero in that range. It is worth emphasizing, also, that b_2 remains constant and nonvanishing in both R_2 and P_2 beyond $|\Delta\eta| \sim 1.5$ and $|\Delta\eta| \sim 0.7$, respectively, thereby supporting the notion that collective behavior might be present in p-Pb collisions [115–120]. Unfortunately, the measurements presented in this work do not provide sufficient accuracy on b_3 and b_4 to establish whether significant triangular and quadrangular flow components are present in high-multiplicity p-Pb collisions.

One further explores the long-range behavior of the R_2 and P_2 correlation functions by comparing the Fourier coefficients' $|\Delta\eta|$ dependence of LS and US correlations presented in Figs. 31 and 32, respectively. The presentation is limited to the 0%–20% multiplicity class but we verified that correlations from lower multiplicity exhibit a similar behavior as that shown. One observes that the coefficients obtained from US distributions, most particularly b_1 and b_2, are significantly larger than those extracted from LS distributions for rapidity difference smaller than $|\Delta\eta| \sim 1.5$, as evidently expected from the prominence of the near-side US peaks observed in both R_2 and P_2 relative to the much smaller near-side structure encountered in LS distributions. One notes, however, that US and LS R_2 coefficients converge to essentially equal values at $|\Delta\eta| > 1.5$ and thus provide an indication that the correlation dynamics is charge agnostic at large relative pseudorapidities; a result also readily obvious from the $R_2^{(CD)}$ presented in Fig. 9. It is worth additionally noting that the

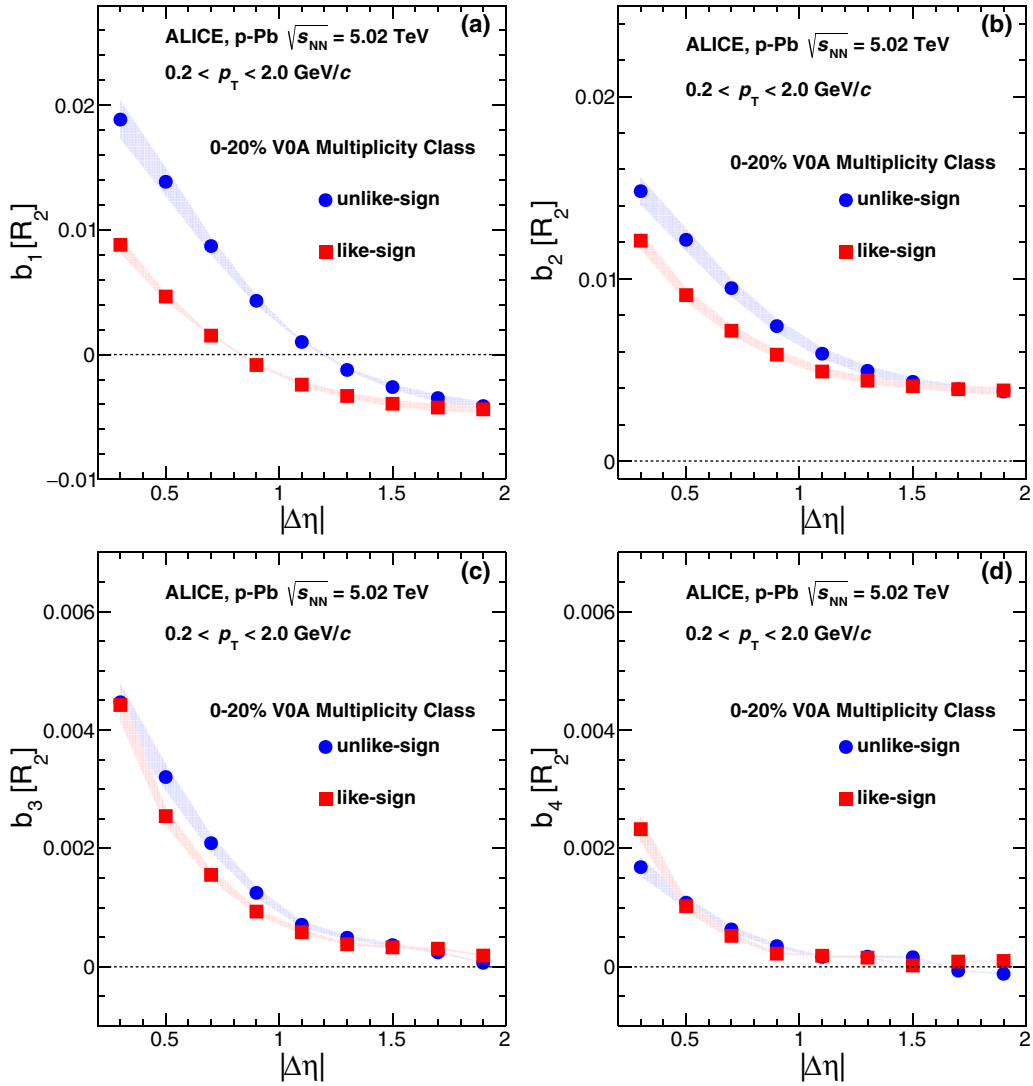

FIG. 31. Fourier coefficient, $b_n, n = 1, \ldots, 4$, measured in R_2 in 0%–20% multiplicity class in p-Pb collisions at $\sqrt{s_{NN}} = 5.02$ TeV. Vertical bars and shaded areas represent statistical and systematic uncertainties, respectively.

differences between $b_3[R_2]$ and $b_4[R_2]$ of US and LS are rather small for $|\Delta\eta| < 1$ and essentially vanishing, within experimental uncertainties beyond $|\Delta\eta| \sim 1$. The behavior and dependence of the $b_n[P_2]$ coefficients are qualitatively similar to those of $b_n[R_2]$ coefficients. One finds, however, that differences between US and LS coefficients are typically very small or vanishing for relative pseudorapidities as small as $|\Delta\eta| \sim 0.6$, again emphasizing the narrow peak observed in P_2 distributions relative to those measured in R_2 distributions.

VII. DISCUSSION

A. Charge insensitive nonflow contributions at large $|\Delta\eta|$

Fourier decomposition analyses of R_2 and P_2 correlation functions measured in Pb-Pb collisions, shown in Figs. 26–28, reveal that beyond $|\Delta\eta| \sim 0.9$, the coefficients v_2, v_3, and v_4 obtained with LS and US pairs are identical within measurement uncertainties. This is confirmed also by the inspection of CD correlations, shown in Figs. 8 and 9, which exhibit nearly vanishing amplitude in mid-to-central collisions beyond $|\Delta\eta| \sim 1.4$ and on the away side, i.e., at $\Delta\varphi \sim \pi$. One can then consider a two-component model of these correlations consisting of a near-side component determined chiefly by charge-dependent particle production processes [such as resonance decays, $(+,-)$ pair creation in jets or via string hadronization, etc.] and a long-range component essentially insensitive to particle charges. In mid-to-central Pb-Pb collisions, this long-range component is attributed to collective flow resulting in part from spatial anisotropy of the system and energy density and/or pressure gradients. However, the possibility of a long-range nonflow contribution, i.e., noncollective in nature, cannot be eliminated. Indeed, long-range and charge-insensitive nonflow contributions may in part arise from back-to-back jets, but they may also result from a superposition of long-range particle correlations arising in simpler collision systems such as pp and p-Pb. The $R_2^{(\mathrm{CD})}$ and $P_2^{(\mathrm{CD})}$ distributions shown in Fig. 9 reveal that two-particle correlations in p-Pb collisions also feature nearly

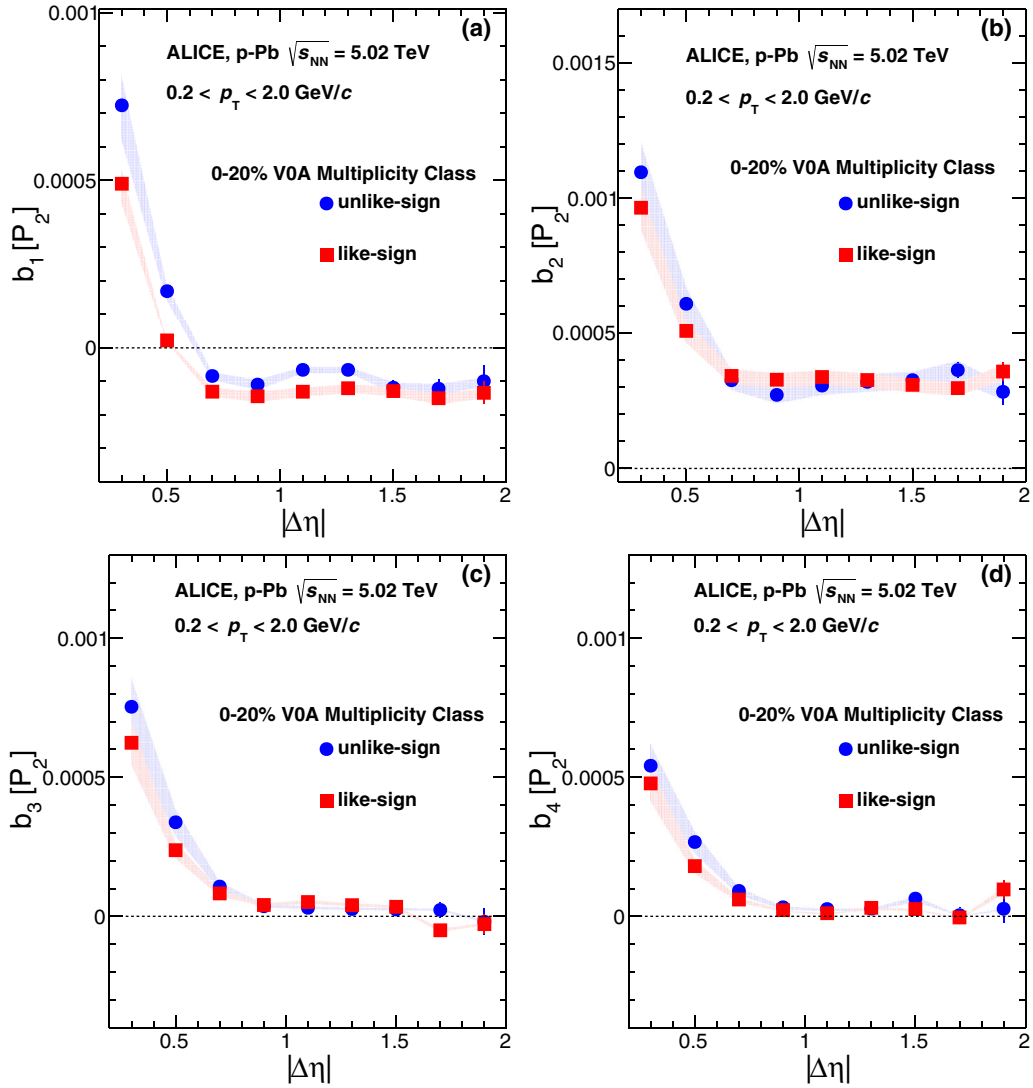

FIG. 32. Fourier coefficient, b_n, $n = 1, \ldots, 4$, measured in P_2 in 0%–20% multiplicity class in p-Pb collisions at $\sqrt{s_{NN}} = 5.02$ TeV. Vertical bars and shaded areas represent statistical and systematic uncertainties, respectively.

vanishing correlation amplitude at large $|\Delta\eta|$ and on the away side of these correlation functions. Recall from Sec. VI E that the Fourier decompositions of R_2 and P_2 correlation functions of LS and US pairs feature essentially identical harmonic coefficients b_n for $n = 2$, 3, and 4 at large $|\Delta\eta|$. Correlations in p-Pb collisions can then, at least approximately, be considered as a superposition of short-range correlations leading to the production of the near-side peak observed in these correlations and a long-range component insensitive to the charge of particles. It is unclear whether this long-range component reflects the production of a flowing medium in p-Pb collisions or whether it arises from noncollective particle production and transport. It is nonetheless of interest to consider how such a component would scale in Pb-Pb collisions if nucleon-nucleon (or parton-parton) interactions taking place in these collisions were completely independent of one another and in the absence of rescattering of the particles these interactions produce. Indeed, assuming Pb-Pb collisions are such a trivial superposition of p-Pb collisions, the long-range component of these p-Pb collisions can be considered, for practical intents, as a nonflow contribution to the correlation measured in Pb-Pb. One can then use a basic property of cumulants to determine an upper bound on nonflow effects in Pb-Pb arising from a superposition of p-Pb subprocesses. The normalized cumulants R_2 and P_2 scale inversely with the number of identical subprocesses. The nonflow contributions to the v_n coefficients should then be of the order of $\sqrt{b_n}/\sqrt{m}$, where m is the average number of wounded nucleons encountered at a given collision centrality in Pb-Pb collisions. Let us thus consider, as an example, a simple evaluation of an upper limit of contributions to elliptical flow measured in Pb-Pb collisions based on the long-range values of b_2 in p-Pb. In p-Pb collisions, one finds $b_2 \sim 0.004$ at $|\Delta\eta| > 1.5$. Assuming that, on average, a central Pb-Pb collision is equivalent to approximately 200 p-Pb collisions, the nonflow contribution to long-range v_2 values is thus of the order of $\sqrt{0.004/200} = 0.0045$. The measured v_2 for LS and US pairs in 0%–5% collision centralities amounts to $v_2 = 0.027$. Considering that

this "nonflow" contribution adds in quadrature with the flow term in Pb-Pb, one concludes that nonflow contributions are of the order of ∼1.5% of the observed v_2 in this centrality. This conclusion is in qualitative agreement with assessments of nonflow contributions obtained from other methods [87].

B. Charge sensitive nonflow contributions at small $|\Delta\eta|$

The two-component model invoked in the previous section to separate the near-side short-range correlation peaks and the long-range correlations observed in this work has been commonly used in other works to subtract the long-range component as a background, and to study the features of the near-side peak. However, the near-side peaks observed in R_2 and P_2 exhibit rather different properties and one may then wonder whether a two-component model is actually appropriate. Indeed, one finds that the near-side peaks observed in P_2 correlations, in both Pb-Pb and p-Pb collisions, cover a different $|\Delta\eta|$ range than the peaks observed in R_2 distributions. Accordingly, one finds that the LS and US v_n and b_n coefficients measured in Pb-Pb and p-Pb collisions, respectively, reach a plateau at much smaller $|\Delta\eta|$ in P_2 distributions than in R_2 distributions. This is rather remarkable given that both observables are proportional, effectively, to integrals over the 0.2 to 2.0 GeV/c momentum range of the two-particle density $\rho_2(\mathbf{p}_1, \mathbf{p}_2)$, albeit with different coefficients (unity for R_2 and $\Delta p_{\rm T}\Delta p_{\rm T}$ for P_2). One would thus expect the two correlation observables to feature similar near-side structures and dependence on $|\Delta\eta|$. The observed difference between the shapes, not just the strengths, must then arise from the dependence of P_2 on $\Delta p_{\rm T}\Delta p_{\rm T}$. In fact, given that this coefficient is not positive definite, correlated pairs may yield either positive or negative contributions to P_2. The narrower peak observed in P_2 implies that pairs in the range $0.5 < |\Delta\eta| < 0.9$, where P_2 is suppressed relative to R_2, and receives, on average, vanishing contributions from the $\Delta p_{\rm T}\Delta p_{\rm T}$ coefficient, while the range $|\Delta\eta| < 0.5$ is positive definite on average. Conceivably, the near-side might itself consist of two components: one "regular" component with nonvanishing $\langle\Delta p_{\rm T}\Delta p_{\rm T}\rangle$ present in both R_2 and P_2, and one component with vanishing $\langle\Delta p_{\rm T}\Delta p_{\rm T}\rangle$ contributing only to R_2. However, it is difficult to identify particle-production processes that might feature such properties. It is possible, on the other hand, that certain processes might feature vanishing $\langle\Delta p_{\rm T}\Delta p_{\rm T}\rangle$ over a limited range of phase space. Consider, for instance, the decay of resonances such as the ρ^0-meson into a pair of $\pi^+\pi^-$ mesons. In-flight decays of ρ^0-mesons produce kinematically focused $\pi^+\pi^-$ pairs, which are detected at small relative angles ($\Delta\phi$ and $\Delta\eta$) in the laboratory frame. Correlated pions from such decays could feature positive or negative values of $\Delta p_{\rm T}\Delta p_{\rm T}$ depending on the orientation of the decay relative to the direction of their parent ρ^0 meson. Likewise, particles composing jets might also contribute differentially, with $|\Delta\eta|$, to P_2. The core of jets (particles emitted at small angles relative to the jet axis) typically involve large momenta, i.e., particles with momenta well in excess of the inclusive average $\langle p_{\rm T}\rangle$. They would thus make a strong positive contribution to P_2. Particles emitted at large angles, relative to the jet axis, typically feature lower momenta. They might then contribute equally negative and positive terms to $\Delta p_{\rm T}\Delta p_{\rm T}$ and thus yield a vanishing average. Particles of the jet outer edges would evidently have positive contributions to R_2 and thus produce a near-side peak characteristic of the width of jets but their vanishing $\Delta p_{\rm T}\Delta p_{\rm T}$ average might effectively produce a narrower peak in P_2 relative to that observed in R_2.

One can speculate further about the role of jets in near-side correlations based on the $R_2^{\rm (CD)}$ and $P_2^{\rm (CD)}$ distributions shown in Figs. 8 and 9. In Pb-Pb collisions, the observed longitudinal narrowing of $R_2^{\rm (CD)}$ distributions with increasing collision centrality may be interpreted as evidence, in part, for strong radial flow and two-stage particle emission. Indeed, correlated particles emitted from a radially boosted source are kinematically focused, i.e., emitted at smaller relative rapidity. Similarly, late-stage particle emission, after the system has cooled down, may also produce particles with smaller relative rapidity. The $R_2^{\rm (CD)}$ correlation function is thus expected to narrow considerably under the combination of the two effects. Careful modeling of the correlation functions shall be required, however, to interpret the observed narrowing of $R_2^{\rm (CD)}$ and disentangle the relative contributions of radial flow and late-stage emission.

Additionally, in light of the narrower width of $P_2^{\rm (CI)}$ distributions relative to those of $R_2^{\rm (CI)}$ and the role of jet-like contributions in these correlation functions, as discussed above, one should also examine the role of jet-like contributions to $R_2^{\rm (CD)}$ and $P_2^{\rm (CD)}$ distributions. It is in fact interesting that the longitudinal width of $P_2^{\rm (CD)}$ remains essentially independent of collision centrality, thereby hinting that it might be insensitive to effects associated with radial flow and two-stage particle production. A dominance of jet-like contributions to this correlation could then be used to study the impact of the medium on jets. That would likely require, however, a much larger dataset to reduce statistical uncertainties and enable more precise corrections for instrumental effects, which currently limit the precision of the measurement reported in this work.

VIII. SUMMARY AND CONCLUSION

Measurements of two-particle differential number-correlation functions R_2 and transverse momentum correlation functions P_2 obtained in Pb-Pb collisions at $\sqrt{s_{\rm NN}} = 2.76$ TeV and in p-Pb collisions at $\sqrt{s_{\rm NN}} = 5.02$ TeV were presented. Measurements were reported as a function of collision centrality and multiplicity for these two collision systems, respectively, for charged particles in the range $|\eta| < 1.0$ and $0.2 < p_{\rm T} < 2.0$ GeV/c. Measurements of correlation functions for like-sign (LS) and unlike-sign (US) particle pairs were first carried out separately and combined to obtain charge-independent (CI) and charge-dependent (CD) correlation functions. The R_2 and P_2 correlators exhibit similar features; most notably a relatively strong near-side peak centered at $|\Delta\eta| \sim \Delta\varphi \sim 0$, and a weaker away-side ridge (at $\Delta\varphi = \pi$) with a width larger than the η acceptance (two units) in low-multiplicity event classes. Both correlation observables also exhibit strong harmonic modulations in mid-central-to-central Pb-Pb collisions. However, there are

also interesting and revealing differences. One finds, both in Pb-Pb and p-Pb collisions, that the near-side peak of P_2 is much narrower in $|\Delta\eta|$ and $\Delta\varphi$ than observed with R_2. One also observes, in the 5% most-central Pb-Pb collisions, that the away-side of P_2 features a dip structure at $\Delta\varphi \sim \pi$, and sideband peaks at $\Delta\varphi \sim \pi \pm \pi/3$ extending across $|\Delta\eta| < 2$. Such a modulated structure is not present in the 5% most-central Pb-Pb collisions measured in this work for R_2 but was observed for number correlations, similar to R_2, only in very-central collisions (0%–2%), thereby indicating that P_2 is somewhat more sensitive to the presence of a third-harmonic (triangular) flow component.

The width of the near-side peak of the R_2 and P_2 charge-independent and charge-dependent correlation functions were studied in order to better understand the relative contributions of nonflow and flow effects to particle correlations. In Pb-Pb, the longitudinal width $\langle \Delta\eta^k \rangle^{1/k}$ of both $R_2^{(\mathrm{CI})}$ and $P_2^{(\mathrm{CI})}$ exhibits sizable growth for increasing collision centrality. However, no significant dependence of the CI correlation widths was observed in p-Pb. In contrast, one finds that the width of $R_2^{(\mathrm{CD})}$ correlation functions significantly narrow with increasing collision centrality in Pb-Pb, or produced-particle multiplicity in p-Pb, while only a modest decrease of the width of the near-side $P_2^{(\mathrm{CD})}$ peak could be ascertained within the current analysis. One furthermore observes that the $\Delta\varphi$ width of the near-side peak of $R_2^{(\mathrm{CD})}$ exhibits a significant decrease with increasing produced-particle multiplicity in Pb-Pb. The decrease is more modest in p-Pb collisions for $R_2^{(\mathrm{CD})}$, while the observed azimuthal width of the near-side peak of $P_2^{(\mathrm{CD})}$ is consistent with a modest decrease with increasing multiplicity.

The narrowing of the near-side of $R_2^{(\mathrm{CD})}$ is consistent with the narrowing of the balance function already reported and can be interpreted, in part, as an effect of radial flow and two-stage hadronization. However, finite diffusion effects, which broaden the correlation functions, are also expected in long-lived collision systems. The observed broadening of $R_2^{(\mathrm{CI})}$ and $P_2^{(\mathrm{CI})}$, with increasing collision centrality in Pb-Pb collisions, might in part result from such diffusive effects, but other processes influencing the strength of long-range longitudinal correlations must be considered. The dependence of the $\Delta\varphi$ width of the near-side peak of $R_2^{(\mathrm{CD})}$ and $P_2^{(\mathrm{CD})}$ were studied vs increasing pair separation in $\Delta\eta$. They exhibit a nonmonotonic dependence on the pair separation, which might in part be caused by diffusion effects, although the role of differential radial flow may not be excluded without specific models of these effects. In fact, one anticipates that the observed centrality and pair-separation dependence of the width of the near-side peaks of $R_2^{(\mathrm{CD})}$ and $P_2^{(\mathrm{CD})}$ shall provide important constraints in the formulation of models of the collision dynamics, which might help to better constrain the contributions of radial flow, diffusion, and two-stage emission in Pb-Pb collisions, most particularly.

The need to better understand the roles of nonflow and flow also prompted the analysis in terms of $|\Delta\eta|$ pair separation (η gap) dependent Fourier decompositions of the $\Delta\varphi$ behavior of the R_2 and P_2 correlation functions. Significant differences in the dependence of the harmonic and flow coefficients between the correlator R_2 and P_2 were found, owing to the fact, most likely, that the measured P_2 correlation functions feature a much narrower near-side peak than their corresponding R_2 counterparts. Indeed, one observes that the v_n coefficients measured in P_2 correlations reach a plateau at much smaller pair separation than those observed in R_2 correlations. These differences indicate that the R_2 and P_2 correlation functions exhibit distinct sensitivities to flow and nonflow effects and could then be exploited, in theoretical models, to obtain better insight into particle-production and transport dynamics in heavy-ion collisions. Long-range nonflow effects may also exist, however, and the magnitude of the b_2 coefficients observed at large pair separation in p-Pb collisions was used to obtain an upper limit of 1.5% for nonflow contributions to v_2 in the 5% most-central Pb-Pb collisions.

ACKNOWLEDGMENTS

The ALICE Collaboration would like to thank all its engineers and technicians for their invaluable contributions to the construction of the experiment and the CERN accelerator teams for the outstanding performance of the LHC complex. The ALICE Collaboration gratefully acknowledges the resources and support provided by all Grid centers and the Worldwide LHC Computing Grid (WLCG) collaboration. The ALICE Collaboration acknowledges the following funding agencies for their support in building and running the ALICE detector: A. I. Alikhanyan National Science Laboratory (Yerevan Physics Institute) Foundation (ANSL), State Committee of Science and World Federation of Scientists (WFS), Armenia; Austrian Academy of Sciences and Nationalstiftung für Forschung, Technologie und Entwicklung, Austria; Ministry of Communications and High Technologies, National Nuclear Research Center, Azerbaijan; Conselho Nacional de Desenvolvimento Científico e Tecnológico (CNPq), Universidade Federal do Rio Grande do Sul (UFRGS), Financiadora de Estudos e Projetos (Finep) and Fundação de Amparo à Pesquisa do Estado de São Paulo (FAPESP), Brazil; Ministry of Science & Technology of China (MSTC), National Natural Science Foundation of China (NSFC) and Ministry of Education of China (MOEC), China; Ministry of Science and Education, Croatia; Ministry of Education, Youth and Sports of the Czech Republic, Czech Republic; The Danish Council for Independent Research—Natural Sciences, the Carlsberg Foundation and Danish National Research Foundation (DNRF), Denmark; Helsinki Institute of Physics (HIP), Finland; Commissariat à l'Energie Atomique (CEA) and Institut National de Physique Nucléaire et de Physique des Particules (IN2P3) and Centre National de la Recherche Scientifique (CNRS), France; Bundesministerium fü Bildung, Wissenschaft, Forschung und Technologie (BMBF) and GSI Helmholtzzentrum für Schwerionenforschung GmbH, Germany; General Secretariat for Research and Technology, Ministry of Education, Research and Religions, Greece; National Research, Development and Innovation Office, Hungary; Department of Atomic Energy, Government of India (DAE), Department of Science and Technology, Government of India (DST), University Grants Commission, Government of India (UGC) and Council of Scientific and Industrial Research (CSIR), India; Indonesian Institute of Science, Indonesia;

Centro Fermi - Museo Storico della Fisica e Centro Studi e Ricerche Enrico Fermi and Istituto Nazionale di Fisica Nucleare (INFN), Italy; Institute for Innovative Science and Technology, Nagasaki Institute of Applied Science (IIST), Japan Society for the Promotion of Science (JSPS) KAKENHI and Japanese Ministry of Education, Culture, Sports, Science and Technology (MEXT), Japan; Consejo Nacional de Ciencia (CONACYT) y Tecnología, through Fondo de Cooperación Internacional en Ciencia y Tecnología (FONCICYT) and Dirección General de Asuntos del Personal Academico (DGAPA), Mexico; Nederlandse Organisatie voor Wetenschappelijk Onderzoek (NWO), Netherlands; The Research Council of Norway, Norway; Commission on Science and Technology for Sustainable Development in the South (COMSATS), Pakistan; Pontificia Universidad Católica del Perú, Peru; Ministry of Science and Higher Education and National Science Centre, Poland; Korea Institute of Science and Technology Information and National Research Foundation of Korea (NRF), Republic of Korea; Ministry of Education and Scientific Research, Institute of Atomic Physics and Romanian National Agency for Science, Technology and Innovation, Romania; Joint Institute for Nuclear Research (JINR), Ministry of Education and Science of the Russian Federation and National Research Centre Kurchatov Institute, Russia; Ministry of Education, Science, Research and Sport of the Slovak Republic, Slovakia; National Research Foundation of South Africa, South Africa; Centro de Aplicaciones Tecnológicas y Desarrollo Nuclear (CEADEN), Cubaenergía, Cuba and Centro de Investigaciones Energéticas, Medioambientales y Tecnológicas (CIEMAT), Spain; Swedish Research Council (VR) and Knut & Alice Wallenberg Foundation (KAW), Sweden; European Organization for Nuclear Research, Switzerland; National Science and Technology Development Agency (NSDTA), Suranaree University of Technology (SUT) and Office of the Higher Education Commission under NRU project of Thailand, Thailand; Turkish Atomic Energy Agency (TAEK), Turkey; National Academy of Sciences of Ukraine, Ukraine; Science and Technology Facilities Council (STFC), United Kingdom; National Science Foundation of the United States of America (NSF) and United States Department of Energy, Office of Nuclear Physics (DOE NP), United States of America.

[1] J. Adams *et al.* (STAR Collaboration), Experimental and theoretical challenges in the search for the quark gluon plasma: The STAR's critical assessment of the evidence from RHIC collisions, Nucl. Phys. A **757**, 102 (2005).

[2] K. Adcox *et al.* (PHENIX Collaboration), Formation of dense partonic matter in relativistic nucleus-nucleus collisions at RHIC: Experimental evaluation by the PHENIX, Nucl. Phys. A **757**, 184 (2005).

[3] I. Arsene *et al.* (BRAHMS Collaboration), Quark gluon plasma and color glass condensate at RHIC? The perspective from the BRAHMS experiment, Nucl. Phys. A **757**, 1 (2005).

[4] B. B. Back *et al.* (PHOBOS Collaboration), The PHOBOS perspective on discoveries at RHIC, Nucl. Phys. A **757**, 28 (2005).

[5] J. Adams *et al.* (STAR Collaboration), Azimuthal anisotropy in Au-Au collisions at $\sqrt{s_{\rm NN}} = 200\,{\rm GeV}$, Phys. Rev. C **72**, 014904 (2005).

[6] K. Aamodt *et al.* (ALICE Collaboration), Harmonic decomposition of two-particle angular correlations in Pb-Pb collisions at $\sqrt{s_{\rm NN}} = 2.76\,{\rm TeV}$, Phys. Lett. B **708**, 249 (2012).

[7] U. Heinz and R. Snellings, Collective flow and viscosity in relativistic heavy-ion collisions, Annu. Rev. Nucl. Part. Sci. **63**, 123 (2013).

[8] K. Aamodt *et al.* (ALICE Collaboration), Elliptic Flow of Charged Particles in Pb-Pb Collisions at $\sqrt{s_{\rm NN}} = 2.76\,{\rm TeV}$, Phys. Rev. Lett. **105**, 252302 (2010).

[9] J. Adams *et al.* (STAR Collaboration), Evidence from $d+$ Au Measurements for Final State Suppression of High-$p_{\rm T}$ Hadrons in Au-Au Collisions at RHIC, Phys. Rev. Lett. **91**, 072304 (2003).

[10] B. I. Abelev *et al.* (STAR Collaboration), System size dependence of associated yields in hadron-triggered jets, Phys. Lett. B **683**, 123 (2010).

[11] C. Adler *et al.* (STAR Collaboration), Disappearance of Back-To-Back High-$p_{\rm T}$ Hadron Correlations in Central Au-Au Collisions at $\sqrt{s_{\rm NN}} = 200\,{\rm GeV}$, Phys. Rev. Lett. **90**, 082302 (2003).

[12] S. S. Adler *et al.* (PHENIX Collaboration), Suppressed π^0 Production at Large Transverse Momentum in Central Au-Au Collisions at $\sqrt{s_{\rm NN}} = 200\,{\rm GeV}$, Phys. Rev. Lett. **91**, 072301 (2003).

[13] K. Adcox *et al.* (PHENIX Collaboration), Suppression of Hadrons with Large Transverse Momentum in Central Au-Au Collisions at $\sqrt{s_{\rm NN}} = 130\,{\rm GeV}$, Phys. Rev. Lett. **88**, 022301 (2001).

[14] J. Adams *et al.* (STAR Collaboration), Transverse-Momentum and Collision-Energy Dependence of High-p_T Hadron Suppression in Au-Au Collisions at Ultrarelativistic Energies, Phys. Rev. Lett. **91**, 172302 (2003).

[15] S. S. Adler *et al.* (PHENIX Collaboration), High-$p_{\rm T}$ charged hadron suppression in Au-Au collisions at $\sqrt{s_{\rm NN}} = 200\,{\rm GeV}$, Phys. Rev. C **69**, 034910 (2004).

[16] S. S. Adler *et al.* (PHENIX Collaboration), Common Suppression Pattern of η and π^0 Mesons at High Transverse Momentum in Au-Au Collisions at $\sqrt{s_{\rm NN}} = 200\,{\rm GeV}$, Phys. Rev. Lett. **96**, 202301 (2006).

[17] S. S. Adler *et al.* (PHENIX Collaboration), High transverse momentum η meson production in pp, d-Au, and Au-Au collisions at $\sqrt{s_{\rm NN}} = 200\,{\rm GeV}$, Phys. Rev. C **75**, 024909 (2007).

[18] B. I. Abelev *et al.* (STAR Collaboration), Identified Baryon and Meson Distributions at Large Transverse Momenta from Au-Au Collisions at $\sqrt{s_{\rm NN}} = 200\,{\rm GeV}$, Phys. Rev. Lett. **97**, 152301 (2006).

[19] A. Sickles (PHENIX Collaboration), Jet correlations of identified particles in PHENIX, J. Phys. G **30**, S1291 (2004).

[20] A. Adare *et al.* (PHENIX Collaboration), Dihadron azimuthal correlations in Au-Au collisions at $\sqrt{s_{\rm NN}} = 200\,{\rm GeV}$, Phys. Rev. C **78**, 014901 (2008).

[21] J. Adams *et al.* (STAR Collaboration), Direct Observation of Dijets in Central Au-Au Collisions at $\sqrt{s_{\rm NN}} = 200\,{\rm GeV}$, Phys. Rev. Lett. **97**, 162301 (2006).

[22] A. Adare *et al.* (PHENIX Collaboration), Transverse momentum and centrality dependence of dihadron correlations in Au-Au collisions at $\sqrt{s_{\rm NN}} = 200$ GeV: Jet quenching and the response of partonic matter, Phys. Rev. C **77**, 011901 (2008).

[23] J. Adams *et al.* (STAR Collaboration), Distributions of Charged Hadrons Associated with High Transverse Momentum Particles in pp and Au-Au Collisions at $\sqrt{s_{\rm NN}} =$ 200 GeV, Phys. Rev. Lett. **95**, 152301 (2005).

[24] S. S. Adler *et al.* (PHENIX Collaboration), Dense-Medium Modifications to Jet-Induced Hadron Pair Distributions in Au-Au Collisions at $\sqrt{s_{\rm NN}} = 200$ GeV, Phys. Rev. Lett. **97**, 052301 (2006).

[25] A. Adare *et al.* (PHENIX Collaboration), System Size and Energy Dependence of Jet-Induced Hadron Pair Correlation Shapes in Cu-Cu and Au-Au Collisions at $\sqrt{s_{\rm NN}} = 200$ and 62.4 GeV, Phys. Rev. Lett. **98**, 232302 (2007).

[26] J. Adams *et al.* (STAR Collaboration), $\Delta\phi\Delta\eta$ correlations in central Au-Au collisions at 200 GeV, Phys. Rev. C **75**, 034901 (2007).

[27] J. Adams *et al.* (STAR Collaboration), Minijet deformation and charge-independent angular correlations on momentum subspace (η, ϕ) in Au-Au collisions at $\sqrt{s_{\rm NN}} = 130$ GeV, Phys. Rev. C **73**, 064907 (2006).

[28] B. I. Abelev *et al.* (STAR Collaboration), Growth of Long-Range Forward-Backward Multiplicity Correlations with Centrality in Au-Au Collisions at $\sqrt{s_{\rm NN}} = 200$ GeV, Phys. Rev. Lett. **103**, 172301 (2009).

[29] B. Alver and G. Roland, Collision geometry fluctuations and triangular flow in heavy-ion collisions, Phys. Rev. C **81**, 054905 (2010); **82**, 039903(E) (2010).

[30] A. Dumitru, F. Gelis, L. McLerran, and R. Venugopalan, Glasma flux tubes and the near side ridge phenomenon at RHIC, Nucl. Phys. A **810**, 91 (2008).

[31] S. Gavin, L. McLerran, and G. Moschelli, Long range correlations and the soft ridge in relativistic nuclear collisions, Phys. Rev. C **79**, 051902(R) (2009).

[32] K. Dusling, D. Fernandez-Fraile, and R. Venugopalan, Three-particle correlation from glasma flux tubes, Nucl. Phys. A **828**, 161 (2009).

[33] P. Romatschke, Momentum broadening in an anisotropic plasma, Phys. Rev. C **75**, 014901 (2007).

[34] E. V. Shuryak, Origin of the "ridge" phenomenon induced by jets in heavy ion collisions, Phys. Rev. C **76**, 047901 (2007).

[35] M. Sharma and C. A. Pruneau, Methods for the study of transverse momentum differential correlations, Phys. Rev. C **79**, 024905 (2009).

[36] S. A. Bass, P. Danielewicz, and S. Pratt, Clocking Hadronization in Relativistic Heavy-Ion Collisions with Balance Functions, Phys. Rev. Lett. **85**, 2689 (2000).

[37] S. Jeon and S. Pratt, Balance functions, correlations, charge fluctuations, and interferometry, Phys. Rev. C **65**, 044902 (2002).

[38] S. Pratt, W. P. McCormack, and C. Ratti, Production of charge in heavy-ion collisions, Phys. Rev. C **92**, 064905 (2015).

[39] M. Sakaida, M. Asakawa, and M. Kitazawa, Effects of global charge conservation on time evolution of cumulants of conserved charges in relativistic heavy ion collisions, Phys. Rev. C **90**, 064911 (2014).

[40] S. Pratt, S. Schlichting, and S. Gavin, Effects of momentum conservation and flow on angular correlations at RHIC, Phys. Rev. C **84**, 024909 (2011).

[41] N. Borghini, Multiparticle correlations and momentum conservation in nucleus-nucleus collisions, PoS **(LHC 07)**, 013 (2007).

[42] N. Borghini, Momentum conservation and correlation analyses in heavy ion collisions at ultrarelativistic energies, Phys. Rev. C **75**, 021904(R) (2007).

[43] S. A. Voloshin, V. Koch, and H. G. Ritter, Event-by-event fluctuations in collective quantities, Phys. Rev. C **60**, 024901 (1999).

[44] S. A. Voloshin, Heavy-ion collisions: Correlations and fluctuations in particle production, J. Phys.: Conf. Ser. **50**, 111 (2006).

[45] C. A. Pruneau, S. Gavin, and S. A. Voloshin, Transverse radial flow effects on two- and three-particle angular correlations, Nucl. Phys. A **802**, 107 (2008).

[46] M. Abdel-Aziz and S. Gavin, Diffusion and two-particle correlations, Acta Phys. Hung. New Ser.: Heavy Ion Phys. **25**, 515 (2006).

[47] S. Gavin and M. Abdel-Aziz, Measuring Shear Viscosity Using Transverse Momentum Correlations in Relativistic Nuclear Collisions, Phys. Rev. Lett. **97**, 162302 (2006).

[48] S. Gavin and G. Moschelli, Fluctuation probes of early-time correlations in nuclear collisions, Phys. Rev. C **85**, 014905 (2012).

[49] S. Gavin and G. Moschelli, Viscosity and the soft ridge at RHIC, J. Phys. G **35**, 104084 (2008).

[50] S. Ravan, P. Pujahari, S. Prasad, and C. A. Pruneau, Correcting correlation function measurements, Phys. Rev. C **89**, 024906 (2014).

[51] J. Adams *et al.* (STAR Collaboration), Transverse-momentum $p_{\rm T}$ correlations on (η, ϕ) from mean-$p_{\rm T}$ fluctuations in Au-Au collisions at $\sqrt{s_{\rm NN}} = 200$ GeV, J. Phys. G **32**, L37 (2006).

[52] D. Adamova *et al.* (CERES Collaboration), Event by event fluctuations of the mean transverse momentum in 40, 80, and 158 A GeV/c Pb-Au collisions, Nucl. Phys. A **727**, 97 (2003).

[53] D. Adamova *et al.* (CERES Collaboration), Scale-dependence of transverse momentum correlations in Pb-Au collisions at 158 A-GeV/c, Nucl. Phys. A **811**, 179 (2008).

[54] B. B. Abelev *et al.* (ALICE Collaboration), Event-by-event mean $p_{\rm T}$ fluctuations in pp and Pb-Pb collisions at the LHC, Eur. Phys. J. C **74**, 3077 (2014).

[55] J. Adams *et al.* (STAR Collaboration), Identified Particle Distributions in pp and Au + Au Collisions at $\sqrt{s_{\rm NN}} = 200$ GeV, Phys. Rev. Lett. **92**, 112301 (2004).

[56] B. Abelev *et al.* (ALICE Collaboration), Pion, Kaon, and Proton Production in Central Pb-Pb Collisions at $\sqrt{s_{\rm NN}} =$ 2.76 TeV, Phys. Rev. Lett. **109**, 252301 (2012).

[57] S. Pratt and S. Cheng, Removing distortions from charge balance functions, Phys. Rev. C **68**, 014907 (2003).

[58] J. Adams *et al.* (STAR Collaboration), Narrowing of the Balance Function with Centrality in Au-Au Collisions at $\sqrt{s_{\rm NN}} =$ 130 GeV, Phys. Rev. Lett. **90**, 172301 (2003).

[59] M. M. Aggarwal *et al.* (STAR Collaboration), Balance functions from Au-Au, d-Au, and pp collisions at $\sqrt{s_{\rm NN}} =$ 200 GeV, Phys. Rev. C **82**, 024905 (2010).

[60] B. Abelev *et al.* (STAR Collaboration), Longitudinal scaling property of the charge balance function in Au-Au collisions at $\sqrt{s_{\rm NN}} = 200$ GeV, Phys. Lett. B **690**, 239 (2010).

[61] L. Adamczyk *et al.* (STAR Collaboration), Beam-energy dependence of charge balance functions from Au-Au collisions at energies available at the BNL Relativistic Heavy-ion Collider, Phys. Rev. C **94**, 024909 (2016).

[62] B. Abelev *et al.* (ALICE Collaboration), Charge correlations using the balance function in Pb-Pb collisions at $\sqrt{s_{\rm NN}} = 2.76$ TeV, Phys. Lett. B **723**, 267 (2013).

[63] J. Adam *et al.* (ALICE Collaboration), Multiplicity and transverse momentum evolution of charge-dependent correlations in *pp*, *p*-Pb, and Pb-Pb collisions at the LHC, Eur. Phys. J. C **76**, 86 (2016).

[64] S. Cheng, S. Petriconi, S. Pratt, M. Skoby, C. Gale, S. Jeon, V. T. Pop, and Q.-H. Zhang, Statistical and dynamic models of charge balance functions, Phys. Rev. C **69**, 054906 (2004).

[65] K. Aamodt *et al.* (ALICE Collaboration), The ALICE experiment at the CERN LHC, JINST **3**, S08002 (2008).

[66] D. Nouais *et al.* (ALICE Collaboration), The ALICE silicon drift detector system, Nucl. Instrum. Methods Phys. Res., Sect. A **501**, 119 (2001).

[67] J. Alme *et al.*, The ALICE TPC, a large 3-dimensional tracking device with fast readout for ultra-high multiplicity events, Nucl. Instrum. Methods Phys. Res., Sect. A **622**, 316 (2010).

[68] J. Baechler and T. C. Meyer (ALICE Collaboration), The ALICE time projection chamber: A technological challenge in LHC Heavy-ion physics, Nucl. Instrum. Methods Phys. Res., Sect. A **518**, 94 (2004).

[69] S. Beole *et al.* (ALICE Collaboration), The ALICE inner tracking system: performance with proton and lead beams, Phys. Procedia **37**, 1062 (2012).

[70] P. Cortese *et al.* (ALICE Collaboration), ALICE: Physics performance report, Volume I, J. Phys. G **30**, 1517 (2004).

[71] P. Cortese *et al.* (ALICE Collaboration), ALICE: Physics performance report, Volume II, J. Phys. G **32**, 1295 (2006).

[72] B. B. Abelev *et al.* (ALICE Collaboration), Performance of the ALICE Experiment at the CERN LHC, Int. J. Mod. Phys. A **29**, 1430044 (2014).

[73] K. Aamodt *et al.* (ALICE Collaboration), Centrality Dependence of the Charged-Particle Multiplicity Density at Mid-Rapidity in Pb-Pb Collisions at $\sqrt{s_{\rm NN}} = 2.76$ TeV, Phys. Rev. Lett. **106**, 032301 (2011).

[74] B. Abelev *et al.* (ALICE Collaboration), Centrality determination of Pb-Pb collisions at $\sqrt{s_{\rm NN}} = 2.76$ TeV with ALICE, Phys. Rev. C **88**, 044909 (2013).

[75] J. Adam *et al.* (ALICE Collaboration), Centrality dependence of charged jet production in *p*-Pb collisions at $\sqrt{s_{\rm NN}} = 5.02$ TeV, Eur. Phys. J. C **76**, 271 (2016).

[76] W. Yu (ALICE TPC Collaboration), Particle identification of the ALICE TPC via dE/dx, Nucl. Instrum. Methods Phys. Res., Sect. A **706**, 55 (2013).

[77] B. B. Abelev *et al.* (ALICE Collaboration), Multiplicity dependence of the average transverse momentum in *pp*, *p*-Pb, and Pb-Pb collisions at the LHC, Phys. Lett. B **727**, 371 (2013).

[78] C. Pruneau, S. Gavin, and S. Voloshin, Methods for the study of particle production fluctuations, Phys. Rev. C **66**, 044904 (2002).

[79] L. Tarini, Centrality dependence of two-particle number and transverse momentum correlations in $\sqrt{s_{\rm NN}} = 200$ GeV Au+Au collisions at RHIC, Ph.D. thesis, Wayne State University, 2011 (unpublished).

[80] G. Agakishiev *et al.* (STAR Collaboration), System size and energy dependence of near-side di-hadron correlations, Phys. Rev. C **85**, 014903 (2012).

[81] S. A. Voloshin, A. M. Poskanzer, and R. Snellings, Collective phenomena in non-central nuclear collisions, in *Relativistic Heavy Ion Physics*, Landolt-Börnstein-Group I Elementary Particles, Nuclei and Atoms, edited by R. Stock, Vol. 23 (Springer-Verlag, Berlin, Heidelberg, 2010), p. 293.

[82] N. Borghini, P. M. Dinh, and J.-Y. Ollitrault, Flow analysis from multiparticle azimuthal correlations, Phys. Rev. C **64**, 054901 (2001).

[83] B. B. Abelev *et al.* (ALICE Collaboration), Multiparticle azimuthal correlations in *p*-Pb and Pb-Pb collisions at the CERN Large Hadron Collider, Phys. Rev. C **90**, 054901 (2014).

[84] B. B. Abelev *et al.* (ALICE Collaboration), Long-range angular correlations of π, K, and p in *p*-Pb collisions at $\sqrt{s_{\rm NN}} = 5.02$ TeV, Phys. Lett. B **726**, 164 (2013).

[85] B. B. Abelev *et al.* (ALICE Collaboration), Elliptic flow of identified hadrons in Pb-Pb collisions at $\sqrt{s_{\rm NN}} = 2.76$ TeV, J. High Energy Phys. 06 (2015) 190.

[86] Z. Yin (ALICE Collaboration), Multi-strange baryon elliptic flow in Pb-Pb collisions at $\sqrt{s_{\rm NN}} = 2.76$ TeV measured with the ALICE detector, Central Eur. J. Phys. **10**, 1361 (2012).

[87] J. Adam *et al.* (ALICE Collaboration), Higher harmonic flow coefficients of identified hadrons in Pb-Pb collisions at 2.76 TeV, J. High Energy Phys. 09 (2016) 164.

[88] J. Adam *et al.* (ALICE Collaboration), Centrality dependence of particle production in *p*-Pb collisions at 5.02 TeV, Phys. Rev. C **91**, 064905 (2015).

[89] X. N. Wang and M. Gyulassy, HIJING: A Monte Carlo model for multiple jet production in *pp*, *p-A*, and *A-A* collisions, Phys. Rev. D **44**, 3501 (1991).

[90] M. Gyulassy and X. N. Wang, HIJING 1.0: A Monte Carlo program for parton and particle production in high-energy hadronic and nuclear collisions, Comput. Phys. Commun. **83**, 307 (1994).

[91] R. Brun, F. Bruyant, M. Maire, A. C. McPherson, and P. Zanarini, *GEANT 3: User's guide Geant 3.10, Geant 3.11; rev. version* (CERN, Geneva, 1987).

[92] Z. W. Lin, C. M. Ko, B. A. Li, B. Zhang, and S. Pal, A multi-phase transport model for relativistic heavy-ion collisions, Phys. Rev. C **72**, 064901 (2005).

[93] S. A. Voloshin, Two particle rapidity, transverse momentum, and azimuthal correlations in relativistic nuclear collisions and transverse radial expansion, Nucl. Phys. A **749**, 287 (2005).

[94] B. Alver *et al.* (PHOBOS Collaboration), High Transverse Momentum Triggered Correlations over a Large Pseudorapidity Acceptance in Au-Au Collisions at $\sqrt{s_{\rm NN}} = 200$ GeV, Phys. Rev. Lett. **104**, 062301 (2010).

[95] V. Khachatryan *et al.* (CMS Collaboration), Observation of long-range near-side angular correlations in proton-proton collisions at the LHC, J. High Energy Phys. 09 (2010) 091.

[96] G. Agakishiev *et al.* (STAR Collaboration), Anomalous centrality evolution of two-particle angular correlations from Au-Au collisions at $\sqrt{s_{\rm NN}} = 62$ and 200 GeV, Phys. Rev. C **86**, 064902 (2012).

[97] S. Chatrchyan *et al.* (CMS Collaboration), Studies of azimuthal dihadron correlations in ultra-central Pb-Pb collisions at $\sqrt{s_{\rm NN}} = 2.76$ TeV, J. High Energy Phys. 02 (2014) 088.

[98] U. A. Wiedemann, Gluon radiation off hard quarks in a nuclear environment: Opacity expansion, Nucl. Phys. B **588**, 303 (2000).

[99] J. Casalderrey-Solana, E. V. Shuryak, and D. Teaney, Conical flow induced by quenched QCD jets, J. Phys.: Conf. Ser. **27**, 22 (2005).

[100] I. Vitev, Large angle hadron correlations from medium-induced gluon radiation, Phys. Lett. B **630**, 78 (2005).
[101] A. K. Chaudhuri and U. Heinz, Effect of Jet Quenching on the Hydrodynamical Evolution of QGP, Phys. Rev. Lett. **97**, 062301 (2006).
[102] H. Stoecker, Collective flow signals the quark gluon plasma, Nucl. Phys. A **750**, 121 (2005).
[103] J. Ruppert and B. Muller, Waking the colored plasma, Phys. Lett. B **618**, 123 (2005).
[104] J. Ruppert, Jet-medium interactions: Wakes in the QCD medium, Acta Phys. Hung. New Ser.: Heavy Ion Phys. **27**, 267 (2006).
[105] T. Renk and J. Ruper, The rapidity structure of Mach cones and other large angle correlations in heavy-ion collisions, Phys. Lett. B **646**, 19 (2007).
[106] A. Majumder and X.-N. Wang, Landau-Pomeranchuck-Migdal interference and Cerenkov-like gluon bremsstrahlung in dense matter, Phys. Rev. C **73**, 051901(R) (2006).
[107] G.-Y. Qin, C. Gale, and A. Majumder, Electromagnetic radiation from broken symmetries in relativistic nuclear collisions, Int. J. Mod. Phys. E **16**, 2350 (2007).
[108] J. Adam *et al.* (ALICE Collaboration), Flow Dominance and Factorization of Transverse Momentum Correlations in Pb-Pb Collisions at the LHC, Phys. Rev. Lett. **118**, 162302 (2017).
[109] V. Khachatryan *et al.* (CMS Collaboration), Evidence for Collective Multiparticle Correlations in *p*-Pb Collisions, Phys. Rev. Lett. **115**, 012301 (2015).
[110] S. Gavin, G. Moschelli, and C. Zin, Rapidity correlation structures from causal hydrodynamics, J. Phys.: Conf. Ser. **736**, 012020 (2016).
[111] G. Moschelli and S. Gavin, The glasma and the hard ridge, in Proceedings of the APS meeting of the Division of Particles and Fields 2009, DPF 2009, Detroit, USA, July 26–31, 2009 (2009), arXiv:0911.0094.
[112] C. Pruneau, Modeling correlation functions with a cluster model (unpublished).
[113] P. F. Kolb and U. W. Heinz, Hydrodynamic description of ultrarelativistic heavy-ion collisions, in *Quark Gluon Plasma*, edited by R. C. Hwa and X.-N. Wang (World Scientific, Singapore, 2004), pp. 634–714, arXiv:nucl-th/0305084.
[114] F. Retiere and M. A. Lisa, Observable implications of geometrical and dynamical aspects of freeze out in heavy-ion collisions, Phys. Rev. C **70**, 044907 (2004).
[115] G. Aad *et al.* (ATLAS Collaboration), Observation of Associated Near-Side and Away-Side Long-Range Correlations in $\sqrt{s_{\rm NN}} = 5.02$ TeV Proton-Lead Collisions with the ATLAS Detector, Phys. Rev. Lett. **110**, 182302 (2013).
[116] S. Chatrchyan *et al.* (CMS Collaboration), Multiplicity and transverse momentum dependence of two- and four-particle correlations in *p*-Pb and Pb-Pb collisions, Phys. Lett. B **724**, 213 (2013).
[117] G. Aad *et al.* (ATLAS Collaboration), Measurement with the ATLAS detector of multi-particle azimuthal correlations in *p*-Pb collisions at $\sqrt{s_{\rm NN}} = 5.02$ TeV, Phys. Lett. B **725**, 60 (2013).
[118] P. Bozek, Elliptic flow in proton-proton collisions at $\sqrt{S} = 7$ TeV, Eur. Phys. J. C **71**, 1530 (2011).
[119] P. Bozek and W. Broniowski, Correlations from hydrodynamic flow in *p*-Pb collisions, Phys. Lett. B **718**, 1557 (2013).
[120] P. Bozek and W. Broniowski, Collective dynamics in high-energy proton-nucleus collisions, Phys. Rev. C **88**, 014903 (2013).
[121] D. d'Enterria, G. K. Eyyubova, V. L. Korotkikh, I. P. Lokhtin, S. V. Petrushanko, L. I. Sarycheva, and A. M. Snigirev, Estimates of hadron azimuthal anisotropy from multiparton interactions in proton-proton collisions at 14 TeV, Eur. Phys. J. C **66**, 173 (2010).

S. Acharya,[139] D. Adamová,[93] J. Adolfsson,[80] M. M. Aggarwal,[98] G. Aglieri Rinella,[34] M. Agnello,[31] N. Agrawal,[48] Z. Ahammed,[139] S. U. Ahn,[76] S. Aiola,[144] A. Akindinov,[64] M. Al-Turany,[104] S. N. Alam,[139] D. S. D. Albuquerque,[121] D. Aleksandrov,[87] B. Alessandro,[58] R. Alfaro Molina,[72] Y. Ali,[15] A. Alici,[10,53,27] A. Alkin,[2] J. Alme,[22] T. Alt,[69] L. Altenkamper,[22] I. Altsybeev,[111] M. N. Anaam,[6] C. Andrei,[47] D. Andreou,[34] H. A. Andrews,[108] A. Andronic,[142,104] M. Angeletti,[34] V. Anguelov,[102] C. Anson,[16] T. Antičić,[105] F. Antinori,[56] P. Antonioli,[53] R. Anwar,[125] N. Apadula,[79] L. Aphecetche,[113] H. Appelshäuser,[69] S. Arcelli,[27] R. Arnaldi,[58] O. W. Arnold,[103,116] I. C. Arsene,[21] M. Arslandok,[102] B. Audurier,[113] A. Augustinus,[34] R. Averbeck,[104] M. D. Azmi,[17] A. Badalà,[55] Y. W. Baek,[60,40] S. Bagnasco,[58] R. Bailhache,[69] R. Bala,[99] A. Baldisseri,[135] M. Ball,[42] R. C. Baral,[85] A. M. Barbano,[26] R. Barbera,[28] F. Barile,[52] L. Barioglio,[26] G. G. Barnaföldi,[143] L. S. Barnby,[92] V. Barret,[132] P. Bartalini,[6] K. Barth,[34] E. Bartsch,[69] N. Bastid,[132] S. Basu,[141] G. Batigne,[113] B. Batyunya,[75] P. C. Batzing,[21] J. L. Bazo Alba,[109] I. G. Bearden,[88] H. Beck,[102] C. Bedda,[63] N. K. Behera,[60] I. Belikov,[134] F. Bellini,[34] H. Bello Martinez,[44] R. Bellwied,[125] L. G. E. Beltran,[119] V. Belyaev,[91] G. Bencedi,[143] S. Beole,[26] A. Bercuci,[47] Y. Berdnikov,[96] D. Berenyi,[143] R. A. Bertens,[128] D. Berzano,[34,58] L. Betev,[34] P. P. Bhaduri,[139] A. Bhasin,[99] I. R. Bhat,[99] H. Bhatt,[48] B. Bhattacharjee,[41] J. Bhom,[117] A. Bianchi,[26] L. Bianchi,[125] N. Bianchi,[51] J. Bielčík,[37] J. Bielčíková,[93] A. Bilandzic,[116,103] G. Biro,[143] R. Biswas,[3] S. Biswas,[3] J. T. Blair,[118] D. Blau,[87] C. Blume,[69] G. Boca,[137] F. Bock,[34] A. Bogdanov,[91] L. Boldizsár,[143] M. Bombara,[38] G. Bonomi,[138] M. Bonora,[34] H. Borel,[135] A. Borissov,[18,142] M. Borri,[127] E. Botta,[26] C. Bourjau,[88] L. Bratrud,[69] P. Braun-Munzinger,[104] M. Bregant,[120] T. A. Broker,[69] M. Broz,[37] E. J. Brucken,[43] E. Bruna,[58] G. E. Bruno,[34,33] D. Budnikov,[106] H. Buesching,[69] S. Bufalino,[31] P. Buhler,[112] P. Buncic,[34] O. Busch,[131,a] Z. Buthelezi,[73] J. B. Butt,[15] J. T. Buxton,[95] J. Cabala,[115] D. Caffarri,[89] H. Caines,[144] A. Caliva,[104] E. Calvo Villar,[109] R. S. Camacho,[44] P. Camerini,[25] A. A. Capon,[112] F. Carena,[34] W. Carena,[34] F. Carnesecchi,[27,10] J. Castillo Castellanos,[135] A. J. Castro,[128] E. A. R. Casula,[54] C. Ceballos Sanchez,[8] S. Chandra,[139] B. Chang,[126] W. Chang,[6] S. Chapeland,[34] M. Chartier,[127] S. Chattopadhyay,[139] S. Chattopadhyay,[107] A. Chauvin,[103,116] C. Cheshkov,[133] B. Cheynis,[133]

V. Chibante Barroso,[34] D. D. Chinellato,[121] S. Cho,[60] P. Chochula,[34] T. Chowdhury,[132] P. Christakoglou,[89] C. H. Christensen,[88] P. Christiansen,[80] T. Chujo,[131] S. U. Chung,[18] C. Cicalo,[54] L. Cifarelli,[10,27] F. Cindolo,[53] J. Cleymans,[124] F. Colamaria,[52] D. Colella,[65,34,52] A. Collu,[79] M. Colocci,[27] M. Concas,[58,b] G. Conesa Balbastre,[78] Z. Conesa del Valle,[61] J. G. Contreras,[37] T. M. Cormier,[94] Y. Corrales Morales,[58] P. Cortese,[32] M. R. Cosentino,[122] F. Costa,[34] S. Costanza,[137] J. Crkovská,[61] P. Crochet,[132] E. Cuautle,[70] L. Cunqueiro,[142,94] T. Dahms,[103,116] A. Dainese,[56] S. Dani,[66] M. C. Danisch,[102] A. Danu,[68] D. Das,[107] I. Das,[107] S. Das,[3] A. Dash,[85] S. Dash,[48] S. De,[49] A. De Caro,[30] G. de Cataldo,[52] C. de Conti,[120] J. de Cuveland,[39] A. De Falco,[24] D. De Gruttola,[10,30] N. De Marco,[58] S. De Pasquale,[30] R. D. De Souza,[121] H. F. Degenhardt,[120] A. Deisting,[104,102] A. Deloff,[84] S. Delsanto,[26] C. Deplano,[89] P. Dhankher,[48] D. Di Bari,[33] A. Di Mauro,[34] B. Di Ruzza,[56] R. A. Diaz,[8] T. Dietel,[124] P. Dillenseger,[69] Y. Ding,[6] R. Divià,[34] Ø. Djuvsland,[22] A. Dobrin,[34] D. Domenicis Gimenez,[120] B. Dönigus,[69] O. Dordic,[21] L. V. R. Doremalen,[63] A. K. Dubey,[139] A. Dubla,[104] L. Ducroux,[133] S. Dudi,[98] A. K. Duggal,[98] M. Dukhishyam,[85] P. Dupieux,[132] R. J. Ehlers,[144] D. Elia,[52] E. Endress,[109] H. Engel,[74] E. Epple,[144] B. Erazmus,[113] F. Erhardt,[97] M. R. Ersdal,[22] B. Espagnon,[61] G. Eulisse,[34] J. Eum,[18] D. Evans,[108] S. Evdokimov,[90] L. Fabbietti,[103,116] M. Faggin,[29] J. Faivre,[78] A. Fantoni,[51] M. Fasel,[94] L. Feldkamp,[142] A. Feliciello,[58] G. Feofilov,[111] A. Fernández Téllez,[44] A. Ferretti,[26] A. Festanti,[29,34] V. J. G. Feuillard,[102] J. Figiel,[117] M. A. S. Figueredo,[120] S. Filchagin,[106] D. Finogeev,[62] F. M. Fionda,[22] G. Fiorenza,[52] F. Flor,[125] M. Floris,[34] S. Foertsch,[73] P. Foka,[104] S. Fokin,[87] E. Fragiacomo,[59] A. Francescon,[34] A. Francisco,[113] U. Frankenfeld,[104] G. G. Fronze,[26] U. Fuchs,[34] C. Furget,[78] A. Furs,[62] M. Fusco Girard,[30] J. J. Gaardhøje,[88] M. Gagliardi,[26] A. M. Gago,[109] K. Gajdosova,[88] M. Gallio,[26] C. D. Galvan,[119] P. Ganoti,[83] C. Garabatos,[104] E. Garcia-Solis,[11] K. Garg,[28] C. Gargiulo,[34] P. Gasik,[116,103] E. F. Gauger,[118] M. B. Gay Ducati,[71] M. Germain,[113] J. Ghosh,[107] P. Ghosh,[139] S. K. Ghosh,[3] P. Gianotti,[51] P. Giubellino,[104,58] P. Giubilato,[29] P. Glässel,[102] D. M. Goméz Coral,[72] A. Gomez Ramirez,[74] V. Gonzalez,[104] P. González-Zamora,[44] S. Gorbunov,[39] L. Görlich,[117] S. Gotovac,[35] V. Grabski,[72] L. K. Graczykowski,[140] K. L. Graham,[108] L. Greiner,[79] A. Grelli,[63] C. Grigoras,[34] V. Grigoriev,[91] A. Grigoryan,[1] S. Grigoryan,[75] J. M. Gronefeld,[104] F. Grosa,[31] J. F. Grosse-Oetringhaus,[34] R. Grosso,[104] R. Guernane,[78] B. Guerzoni,[27] M. Guittiere,[113] K. Gulbrandsen,[88] T. Gunji,[130] A. Gupta,[99] R. Gupta,[99] I. B. Guzman,[44] R. Haake,[34] M. K. Habib,[104] C. Hadjidakis,[61] H. Hamagaki,[81] G. Hamar,[143] M. Hamid,[6] J. C. Hamon,[134] R. Hannigan,[118] M. R. Haque,[63] J. W. Harris,[144] A. Harton,[11] H. Hassan,[78] D. Hatzifotiadou,[53,10] S. Hayashi,[130] S. T. Heckel,[69] E. Hellbär,[69] H. Helstrup,[36] A. Herghelegiu,[47] E. G. Hernandez,[44] G. Herrera Corral,[9] F. Herrmann,[142] K. F. Hetland,[36] T. E. Hilden,[43] H. Hillemanns,[34] C. Hills,[127] B. Hippolyte,[134] B. Hohlweger,[103] D. Horak,[37] S. Hornung,[104] R. Hosokawa,[131,78] J. Hota,[66] P. Hristov,[34] C. Huang,[61] C. Hughes,[128] P. Huhn,[69] T. J. Humanic,[95] H. Hushnud,[107] N. Hussain,[41] T. Hussain,[17] D. Hutter,[39] D. S. Hwang,[19] J. P. Iddon,[127] S. A. Iga Buitron,[70] R. Ilkaev,[106] M. Inaba,[131] M. Ippolitov,[87] M. S. Islam,[107] M. Ivanov,[104] V. Ivanov,[96] V. Izucheev,[90] B. Jacak,[79] N. Jacazio,[27] P. M. Jacobs,[79] M. B. Jadhav,[48] S. Jadlovska,[115] J. Jadlovsky,[115] S. Jaelani,[63] C. Jahnke,[120,116] M. J. Jakubowska,[140] M. A. Janik,[140] C. Jena,[85] M. Jercic,[97] O. Jevons,[108] R. T. Jimenez Bustamante,[104] M. Jin,[125] P. G. Jones,[108] A. Jusko,[108] P. Kalinak,[65] A. Kalweit,[34] J. H. Kang,[145] V. Kaplin,[91] S. Kar,[6] A. Karasu Uysal,[77] O. Karavichev,[62] T. Karavicheva,[62] P. Karczmarczyk,[34] E. Karpechev,[62] U. Kebschull,[74] R. Keidel,[46] D. L. D. Keijdener,[63] M. Keil,[34] B. Ketzer,[42] Z. Khabanova,[89] A. M. Khan,[6] S. Khan,[17] S. A. Khan,[139] A. Khanzadeev,[96] Y. Kharlov,[90] A. Khatun,[17] A. Khuntia,[49] M. M. Kielbowicz,[117] B. Kileng,[36] B. Kim,[131] D. Kim,[145] D. J. Kim,[126] E. J. Kim,[13] H. Kim,[145] J. S. Kim,[40] J. Kim,[102] M. Kim,[102,60] S. Kim,[19] T. Kim,[145] T. Kim,[145] S. Kirsch,[39] I. Kisel,[39] S. Kiselev,[64] A. Kisiel,[140] J. L. Klay,[5] C. Klein,[69] J. Klein,[34,58] C. Klein-Bösing,[142] S. Klewin,[102] A. Kluge,[34] M. L. Knichel,[34] A. G. Knospe,[125] C. Kobdaj,[114] M. Kofarago,[143] M. K. Köhler,[102] T. Kollegger,[104] N. Kondratyeva,[91] E. Kondratyuk,[90] A. Konevskikh,[62] M. Konyushikhin,[141] O. Kovalenko,[84] V. Kovalenko,[111] M. Kowalski,[117] I. Králik,[65] A. Kravčáková,[38] L. Kreis,[104] M. Krivda,[65,108] F. Krizek,[93] M. Krüger,[69] E. Kryshen,[96] M. Krzewicki,[39] A. M. Kubera,[95] V. Kučera,[60,93] C. Kuhn,[134] P. G. Kuijer,[89] J. Kumar,[48] L. Kumar,[98] S. Kumar,[48] S. Kundu,[85] P. Kurashvili,[84] A. Kurepin,[62] A. B. Kurepin,[62] A. Kuryakin,[106] S. Kushpil,[93] J. Kvapil,[108] M. J. Kweon,[60] Y. Kwon,[145] S. L. La Pointe,[39] P. La Rocca,[28] Y. S. Lai,[79] I. Lakomov,[34] R. Langoy,[123] K. Lapidus,[144] A. Lardeux,[21] P. Larionov,[51] E. Laudi,[34] R. Lavicka,[37] R. Lea,[25] L. Leardini,[102] S. Lee,[145] F. Lehas,[89] S. Lehner,[112] J. Lehrbach,[39] R. C. Lemmon,[92] I. León Monzón,[119] P. Lévai,[143] X. Li,[12] X. L. Li,[6] J. Lien,[123] R. Lietava,[108] B. Lim,[18] S. Lindal,[21] V. Lindenstruth,[39] S. W. Lindsay,[127] C. Lippmann,[104] M. A. Lisa,[95] V. Litichevskyi,[43] A. Liu,[79] H. M. Ljunggren,[80] W. J. Llope,[141] D. F. Lodato,[63] V. Loginov,[91] C. Loizides,[94,79] P. Loncar,[35] X. Lopez,[132] E. López Torres,[8] A. Lowe,[143] P. Luettig,[69] J. R. Luhder,[142] M. Lunardon,[29] G. Luparello,[59] M. Lupi,[34] A. Maevskaya,[62] M. Mager,[34] S. M. Mahmood,[21] A. Maire,[134] R. D. Majka,[144] M. Malaev,[96] Q. W. Malik,[21] L. Malinina,[75,c] D. Mal'Kevich,[64] P. Malzacher,[104] A. Mamonov,[106] V. Manko,[87] F. Manso,[132] V. Manzari,[52] Y. Mao,[6] M. Marchisone,[129,73,133] J. Mareš,[67] G. V. Margagliotti,[25] A. Margotti,[53] J. Margutti,[63] A. Marín,[104] C. Markert,[118] M. Marquard,[69] N. A. Martin,[104] P. Martinengo,[34] J. L. Martinez,[125] M. I. Martínez,[44] G. Martínez García,[113] M. Martinez Pedreira,[34] S. Masciocchi,[104] M. Masera,[26] A. Masoni,[54] L. Massacrier,[61] E. Masson,[113] A. Mastroserio,[52,136] A. M. Mathis,[116,103] P. F. T. Matuoka,[120] A. Matyja,[117,128] C. Mayer,[117] M. Mazzilli,[33] M. A. Mazzoni,[57] F. Meddi,[23] Y. Melikyan,[91] A. Menchaca-Rocha,[72] E. Meninno,[30] J. Mercado Pérez,[102] M. Meres,[14] C. S. Meza,[109] S. Mhlanga,[124] Y. Miake,[131] L. Micheletti,[26] M. M. Mieskolainen,[43] D. L. Mihaylov,[103] K. Mikhaylov,[64,75] A. Mischke,[63] A. N. Mishra,[70] D. Miśkowiec,[104] J. Mitra,[139] C. M. Mitu,[68] N. Mohammadi,[34] A. P. Mohanty,[63] B. Mohanty,[85] M. Mohisin Khan,[17,d] D. A. Moreira De Godoy,[142] L. A. P. Moreno,[44] S. Moretto,[29] A. Morreale,[113] A. Morsch,[34] V. Muccifora,[51] E. Mudnic,[35] D. Mühlheim,[142] S. Muhuri,[139] M. Mukherjee,[3] J. D. Mulligan,[144] M. G. Munhoz,[120] K. Münning,[42] M. I. A. Munoz,[79] R. H. Munzer,[69] H. Murakami,[130] S. Murray,[73] L. Musa,[34] J. Musinsky,[65] C. J. Myers,[125] J. W. Myrcha,[140] B. Naik,[48] R. Nair,[84]

B. K. Nandi,[48] R. Nania,[53,10] E. Nappi,[52] A. Narayan,[48] M. U. Naru,[15] A. F. Nassirpour,[80] H. Natal da Luz,[120] C. Nattrass,[128] S. R. Navarro,[44] K. Nayak,[85] R. Nayak,[48] T. K. Nayak,[139] S. Nazarenko,[106] R. A. Negrao De Oliveira,[69,34] L. Nellen,[70] S. V. Nesbo,[36] G. Neskovic,[39] F. Ng,[125] M. Nicassio,[104] J. Niedziela,[140,34] B. S. Nielsen,[88] S. Nikolaev,[87] S. Nikulin,[87] V. Nikulin,[96] F. Noferini,[10,53] P. Nomokonov,[75] G. Nooren,[63] J. C. C. Noris,[44] J. Norman,[78] A. Nyanin,[87] J. Nystrand,[22] H. Oh,[145] A. Ohlson,[102] J. Oleniacz,[140] A. C. Oliveira Da Silva,[120] M. H. Oliver,[144] J. Onderwaater,[104] C. Oppedisano,[58] R. Orava,[43] M. Oravec,[115] A. Ortiz Velasquez,[70] A. Oskarsson,[80] J. Otwinowski,[117] K. Oyama,[81] Y. Pachmayer,[102] V. Pacik,[88] D. Pagano,[138] G. Paić,[70] P. Palni,[6] J. Pan,[141] A. K. Pandey,[48] S. Panebianco,[135] V. Papikyan,[1] P. Pareek,[49] J. Park,[60] J. E. Parkkila,[126] S. Parmar,[98] A. Passfeld,[142] S. P. Pathak,[125] R. N. Patra,[139] B. Paul,[58] H. Pei,[6] T. Peitzmann,[63] X. Peng,[6] L. G. Pereira,[71] H. Pereira Da Costa,[135] D. Peresunko,[87] E. Perez Lezama,[69] V. Peskov,[69] Y. Pestov,[4] V. Petráček,[37] M. Petrovici,[47] C. Petta,[28] R. P. Pezzi,[71] S. Piano,[59] M. Pikna,[14] P. Pillot,[113] L. O. D. L. Pimentel,[88] O. Pinazza,[53,34] L. Pinsky,[125] S. Pisano,[51] D. B. Piyarathna,[125] M. Płoskoń,[79] M. Planinic,[97] F. Pliquett,[69] J. Pluta,[140] S. Pochybova,[143] P. L. M. Podesta-Lerma,[119] M. G. Poghosyan,[94] B. Polichtchouk,[90] N. Poljak,[97] W. Poonsawat,[114] A. Pop,[47] H. Poppenborg,[142] S. Porteboeuf-Houssais,[132] V. Pozdniakov,[75] P. Pujahari,[141] S. K. Prasad,[3] R. Preghenella,[53] F. Prino,[58] C. A. Pruneau,[141] I. Pshenichnov,[62] M. Puccio,[26] V. Punin,[106] J. Putschke,[141] S. Raha,[3] S. Rajput,[99] J. Rak,[126] A. Rakotozafindrabe,[135] L. Ramello,[32] F. Rami,[134] R. Raniwala,[100] S. Raniwala,[100] S. S. Räsänen,[43] B. T. Rascanu,[69] V. Ratza,[42] I. Ravasenga,[31] K. F. Read,[128,94] K. Redlich,[84,e] A. Rehman,[22] P. Reichelt,[69] F. Reidt,[34] X. Ren,[6] R. Renfordt,[69] A. Reshetin,[62] J.-P. Revol,[10] K. Reygers,[102] V. Riabov,[96] T. Richert,[63,80] M. Richter,[21] P. Riedler,[34] W. Riegler,[34] F. Riggi,[28] C. Ristea,[68] S. P. Rode,[49] M. Rodríguez Cahuantzi,[44] K. Røed,[21] R. Rogalev,[90] E. Rogochaya,[75] D. Rohr,[34] D. Röhrich,[22] P. S. Rokita,[140] F. Ronchetti,[51] E. D. Rosas,[70] K. Roslon,[140] P. Rosnet,[132] A. Rossi,[29] A. Rotondi,[137] F. Roukoutakis,[83] C. Roy,[134] P. Roy,[107] O. V. Rueda,[70] R. Rui,[25] B. Rumyantsev,[75] A. Rustamov,[86] E. Ryabinkin,[87] Y. Ryabov,[96] A. Rybicki,[117] S. Saarinen,[43] S. Sadhu,[139] S. Sadovsky,[90] K. Šafařík,[34] S. K. Saha,[139] B. Sahoo,[48] P. Sahoo,[49] R. Sahoo,[49] S. Sahoo,[66] P. K. Sahu,[66] J. Saini,[139] S. Sakai,[131] M. A. Saleh,[141] S. Sambyal,[99] V. Samsonov,[96,91] A. Sandoval,[72] A. Sarkar,[73] D. Sarkar,[139] N. Sarkar,[139] P. Sarma,[41] M. H. P. Sas,[63] E. Scapparone,[53] F. Scarlassara,[29] B. Schaefer,[94] H. S. Scheid,[69] C. Schiaua,[47] R. Schicker,[102] C. Schmidt,[104] H. R. Schmidt,[101] M. O. Schmidt,[102] M. Schmidt,[101] N. V. Schmidt,[94,69] J. Schukraft,[34] Y. Schutz,[34,134] K. Schwarz,[104] K. Schweda,[104] G. Scioli,[27] E. Scomparin,[58] M. Šefčík,[38] J. E. Seger,[16] Y. Sekiguchi,[130] D. Sekihata,[45] I. Selyuzhenkov,[104,91] K. Senosi,[73] S. Senyukov,[134] E. Serradilla,[72] P. Sett,[48] A. Sevcenco,[68] A. Shabanov,[62] A. Shabetai,[113] R. Shahoyan,[34] W. Shaikh,[107] A. Shangaraev,[90] A. Sharma,[98] A. Sharma,[99] M. Sharma,[99] N. Sharma,[98] A. I. Sheikh,[139] K. Shigaki,[45] M. Shimomura,[82] S. Shirinkin,[64] Q. Shou,[6,110] K. Shtejer,[26] Y. Sibiriak,[87] S. Siddhanta,[54] K. M. Sielewicz,[34] T. Siemiarczuk,[84] D. Silvermyr,[80] G. Simatovic,[89] G. Simonetti,[34,103] R. Singaraju,[139] R. Singh,[85] R. Singh,[99] V. Singhal,[139] T. Sinha,[107] B. Sitar,[14] M. Sitta,[32] T. B. Skaali,[21] M. Slupecki,[126] N. Smirnov,[144] R. J. M. Snellings,[63] T. W. Snellman,[126] J. Song,[18] F. Soramel,[29] S. Sorensen,[128] F. Sozzi,[104] I. Sputowska,[117] J. Stachel,[102] I. Stan,[68] P. Stankus,[94] E. Stenlund,[80] D. Stocco,[113] M. M. Storetvedt,[36] P. Strmen,[14] A. A. P. Suaide,[120] T. Sugitate,[45] C. Suire,[61] M. Suleymanov,[15] M. Suljic,[34,25] R. Sultanov,[64] M. Šumbera,[93] S. Sumowidagdo,[50] K. Suzuki,[112] S. Swain,[66] A. Szabo,[14] I. Szarka,[14] U. Tabassam,[15] J. Takahashi,[121] G. J. Tambave,[22] N. Tanaka,[131] M. Tarhini,[113] M. Tariq,[17] M. G. Tarzila,[47] A. Tauro,[34] G. Tejeda Muñoz,[44] A. Telesca,[34] C. Terrevoli,[29] B. Teyssier,[133] D. Thakur,[49] S. Thakur,[139] D. Thomas,[118] F. Thoresen,[88] R. Tieulent,[133] A. Tikhonov,[62] A. R. Timmins,[125] A. Toia,[69] N. Topilskaya,[62] M. Toppi,[51] F. Torales-Acosta,[20] S. R. Torres,[119] S. Tripathy,[49] S. Trogolo,[26] G. Trombetta,[33] L. Tropp,[38] V. Trubnikov,[2] W. H. Trzaska,[126] T. P. Trzcinski,[140] B. A. Trzeciak,[63] T. Tsuji,[130] A. Tumkin,[106] R. Turrisi,[56] T. S. Tveter,[21] K. Ullaland,[22] E. N. Umaka,[125] A. Uras,[133] G. L. Usai,[24] A. Utrobicic,[97] M. Vala,[115] J. W. Van Hoorne,[34] M. van Leeuwen,[63] P. Vande Vyvre,[34] D. Varga,[143] A. Vargas,[44] M. Vargyas,[126] R. Varma,[48] M. Vasileiou,[83] A. Vasiliev,[87] A. Vauthier,[78] O. Vázquez Doce,[103,116] V. Vechernin,[111] A. M. Veen,[63] E. Vercellin,[26] S. Vergara Limón,[44] L. Vermunt,[63] R. Vernet,[7] R. Vértesi,[143] L. Vickovic,[35] J. Viinikainen,[126] Z. Vilakazi,[129] O. Villalobos Baillie,[108] A. Villatoro Tello,[44] A. Vinogradov,[87] T. Virgili,[30] V. Vislavicius,[88,80] A. Vodopyanov,[75] M. A. Völkl,[101] K. Voloshin,[64] S. A. Voloshin,[141] G. Volpe,[33] B. von Haller,[34] I. Vorobyev,[116,103] D. Voscek,[115] D. Vranic,[104,34] J. Vrláková,[38] B. Wagner,[22] H. Wang,[63] M. Wang,[6] Y. Watanabe,[131] M. Weber,[112] S. G. Weber,[104] A. Wegrzynek,[34] D. F. Weiser,[102] S. C. Wenzel,[34] J. P. Wessels,[142] U. Westerhoff,[142] A. M. Whitehead,[124] J. Wiechula,[69] J. Wikne,[21] G. Wilk,[84] J. Wilkinson,[53] G. A. Willems,[142,34] M. C. S. Williams,[53] E. Willsher,[108] B. Windelband,[102] W. E. Witt,[128] R. Xu,[6] S. Yalcin,[77] K. Yamakawa,[45] S. Yano,[45] Z. Yin,[6] H. Yokoyama,[78,131] I.-K. Yoo,[18] J. H. Yoon,[60] V. Yurchenko,[2] V. Zaccolo,[58] A. Zaman,[15] C. Zampolli,[34] H. J. C. Zanoli,[120] N. Zardoshti,[108] A. Zarochentsev,[111] P. Závada,[67] N. Zaviyalov,[106] H. Zbroszczyk,[140] M. Zhalov,[96] X. Zhang,[6] Y. Zhang,[6] Z. Zhang,[6,132] C. Zhao,[21] V. Zherebchevskii,[111] N. Zhigareva,[64] D. Zhou,[6] Y. Zhou,[88] Z. Zhou,[22] H. Zhu,[6] J. Zhu,[6] Y. Zhu,[6] A. Zichichi,[27,10] M. B. Zimmermann,[34] G. Zinovjev,[2] J. Zmeskal,[112] and S. Zou[6]

(ALICE Collaboration)

[1]*A.I. Alikhanyan National Science Laboratory (Yerevan Physics Institute) Foundation, Yerevan, Armenia*

[2]*Bogolyubov Institute for Theoretical Physics, National Academy of Sciences of Ukraine, Kiev, Ukraine*

[3]*Bose Institute, Department of Physics and Centre for Astroparticle Physics and Space Science (CAPSS), Kolkata, India*

[4]*Budker Institute for Nuclear Physics, Novosibirsk, Russia*

[5]*California Polytechnic State University, San Luis Obispo, California, USA*

[6]*Central China Normal University, Wuhan, China*
[7]*Centre de Calcul de l'IN2P3, Villeurbanne, Lyon, France*
[8]*Centro de Aplicaciones Tecnológicas y Desarrollo Nuclear (CEADEN), Havana, Cuba*
[9]*Centro de Investigación y de Estudios Avanzados (CINVESTAV), Mexico City and Mérida, Mexico*
[10]*Centro Fermi - Museo Storico della Fisica e Centro Studi e Ricerche "Enrico Fermi," Rome, Italy*
[11]*Chicago State University, Chicago, Illinois, USA*
[12]*China Institute of Atomic Energy, Beijing, China*
[13]*Chonbuk National University, Jeonju, Republic of Korea*
[14]*Comenius University Bratislava, Faculty of Mathematics, Physics and Informatics, Bratislava, Slovakia*
[15]*COMSATS Institute of Information Technology (CIIT), Islamabad, Pakistan*
[16]*Creighton University, Omaha, Nebraska, USA*
[17]*Department of Physics, Aligarh Muslim University, Aligarh, India*
[18]*Department of Physics, Pusan National University, Pusan, Republic of Korea*
[19]*Department of Physics, Sejong University, Seoul, Republic of Korea*
[20]*Department of Physics, University of California, Berkeley, California, USA*
[21]*Department of Physics, University of Oslo, Oslo, Norway*
[22]*Department of Physics and Technology, University of Bergen, Bergen, Norway*
[23]*Dipartimento di Fisica dell'Università 'La Sapienza' and Sezione INFN, Rome, Italy*
[24]*Dipartimento di Fisica dell'Università and Sezione INFN, Cagliari, Italy*
[25]*Dipartimento di Fisica dell'Università and Sezione INFN, Trieste, Italy*
[26]*Dipartimento di Fisica dell'Università and Sezione INFN, Turin, Italy*
[27]*Dipartimento di Fisica e Astronomia dell'Università and Sezione INFN, Bologna, Italy*
[28]*Dipartimento di Fisica e Astronomia dell'Università and Sezione INFN, Catania, Italy*
[29]*Dipartimento di Fisica e Astronomia dell'Università and Sezione INFN, Padova, Italy*
[30]*Dipartimento di Fisica 'E.R. Caianiello' dell'Università and Gruppo Collegato INFN, Salerno, Italy*
[31]*Dipartimento DISAT del Politecnico and Sezione INFN, Turin, Italy*
[32]*Dipartimento di Scienze e Innovazione Tecnologica dell'Università del Piemonte Orientale and INFN Sezione di Torino, Alessandria, Italy*
[33]*Dipartimento Interateneo di Fisica 'M. Merlin' and Sezione INFN, Bari, Italy*
[34]*European Organization for Nuclear Research (CERN), Geneva, Switzerland*
[35]*Faculty of Electrical Engineering, Mechanical Engineering and Naval Architecture, University of Split, Split, Croatia*
[36]*Faculty of Engineering and Science, Western Norway University of Applied Sciences, Bergen, Norway*
[37]*Faculty of Nuclear Sciences and Physical Engineering, Czech Technical University in Prague, Prague, Czech Republic*
[38]*Faculty of Science, P.J. Šafárik University, Košice, Slovakia*
[39]*Frankfurt Institute for Advanced Studies, Johann Wolfgang Goethe-Universität Frankfurt, Frankfurt, Germany*
[40]*Gangneung-Wonju National University, Gangneung, Republic of Korea*
[41]*Gauhati University, Department of Physics, Guwahati, India*
[42]*Helmholtz-Institut für Strahlen- und Kernphysik, Rheinische Friedrich-Wilhelms-Universität Bonn, Bonn, Germany*
[43]*Helsinki Institute of Physics (HIP), Helsinki, Finland*
[44]*High Energy Physics Group, Universidad Autónoma de Puebla, Puebla, Mexico*
[45]*Hiroshima University, Hiroshima, Japan*
[46]*Hochschule Worms, Zentrum für Technologietransfer und Telekommunikation (ZTT), Worms, Germany*
[47]*Horia Hulubei National Institute of Physics and Nuclear Engineering, Bucharest, Romania*
[48]*Indian Institute of Technology Bombay (IIT), Mumbai, India*
[49]*Indian Institute of Technology Indore, Indore, India*
[50]*Indonesian Institute of Sciences, Jakarta, Indonesia*
[51]*INFN, Laboratori Nazionali di Frascati, Frascati, Italy*
[52]*INFN, Sezione di Bari, Bari, Italy*
[53]*INFN, Sezione di Bologna, Bologna, Italy*
[54]*INFN, Sezione di Cagliari, Cagliari, Italy*
[55]*INFN, Sezione di Catania, Catania, Italy*
[56]*INFN, Sezione di Padova, Padova, Italy*
[57]*INFN, Sezione di Roma, Rome, Italy*
[58]*INFN, Sezione di Torino, Turin, Italy*
[59]*INFN, Sezione di Trieste, Trieste, Italy*
[60]*Inha University, Incheon, Republic of Korea*
[61]*Institut de Physique Nucléaire d'Orsay (IPNO), Institut National de Physique Nucléaire et de Physique des Particules (IN2P3/CNRS), Université de Paris-Sud, Université Paris-Saclay, Orsay, France*
[62]*Institute for Nuclear Research, Academy of Sciences, Moscow, Russia*
[63]*Institute for Subatomic Physics, Utrecht University/Nikhef, Utrecht, Netherlands*

[64]*Institute for Theoretical and Experimental Physics, Moscow, Russia*
[65]*Institute of Experimental Physics, Slovak Academy of Sciences, Košice, Slovakia*
[66]*Institute of Physics, Homi Bhabha National Institute, Bhubaneswar, India*
[67]*Institute of Physics of the Czech Academy of Sciences, Prague, Czech Republic*
[68]*Institute of Space Science (ISS), Bucharest, Romania*
[69]*Institut für Kernphysik, Johann Wolfgang Goethe-Universität Frankfurt, Frankfurt, Germany*
[70]*Instituto de Ciencias Nucleares, Universidad Nacional Autónoma de México, Mexico City, Mexico*
[71]*Instituto de Física, Universidade Federal do Rio Grande do Sul (UFRGS), Porto Alegre, Brazil*
[72]*Instituto de Física, Universidad Nacional Autónoma de México, Mexico City, Mexico*
[73]*iThemba LABS, National Research Foundation, Somerset West, South Africa*
[74]*Johann-Wolfgang-Goethe Universität Frankfurt Institut für Informatik, Fachbereich Informatik und Mathematik, Frankfurt, Germany*
[75]*Joint Institute for Nuclear Research (JINR), Dubna, Russia*
[76]*Korea Institute of Science and Technology Information, Daejeon, Republic of Korea*
[77]*KTO Karatay University, Konya, Turkey*
[78]*Laboratoire de Physique Subatomique et de Cosmologie, Université Grenoble-Alpes, CNRS-IN2P3, Grenoble, France*
[79]*Lawrence Berkeley National Laboratory, Berkeley, California, USA*
[80]*Lund University Department of Physics, Division of Particle Physics, Lund, Sweden*
[81]*Nagasaki Institute of Applied Science, Nagasaki, Japan*
[82]*Nara Women's University (NWU), Nara, Japan*
[83]*National and Kapodistrian University of Athens, School of Science, Department of Physics, Athens, Greece*
[84]*National Centre for Nuclear Research, Warsaw, Poland*
[85]*National Institute of Science Education and Research, Homi Bhabha National Institute, Jatni, India*
[86]*National Nuclear Research Center, Baku, Azerbaijan*
[87]*National Research Centre Kurchatov Institute, Moscow, Russia*
[88]*Niels Bohr Institute, University of Copenhagen, Copenhagen, Denmark*
[89]*Nikhef, National institute for subatomic physics, Amsterdam, Netherlands*
[90]*NRC Kurchatov Institute IHEP, Protvino, Russia*
[91]*NRNU Moscow Engineering Physics Institute, Moscow, Russia*
[92]*Nuclear Physics Group, STFC Daresbury Laboratory, Daresbury, United Kingdom*
[93]*Nuclear Physics Institute of the Czech Academy of Sciences, Řež u Prahy, Czech Republic*
[94]*Oak Ridge National Laboratory, Oak Ridge, Tennessee, USA*
[95]*Ohio State University, Columbus, Ohio, USA*
[96]*Petersburg Nuclear Physics Institute, Gatchina, Russia*
[97]*Physics department, Faculty of science, University of Zagreb, Zagreb, Croatia*
[98]*Physics Department, Panjab University, Chandigarh, India*
[99]*Physics Department, University of Jammu, Jammu, India*
[100]*Physics Department, University of Rajasthan, Jaipur, India*
[101]*Physikalisches Institut, Eberhard-Karls-Universität Tübingen, Tübingen, Germany*
[102]*Physikalisches Institut, Ruprecht-Karls-Universität Heidelberg, Heidelberg, Germany*
[103]*Physik Department, Technische Universität München, Munich, Germany*
[104]*Research Division and ExtreMe Matter Institute EMMI, GSI Helmholtzzentrum für Schwerionenforschung GmbH, Darmstadt, Germany*
[105]*Rudjer Bošković Institute, Zagreb, Croatia*
[106]*Russian Federal Nuclear Center (VNIIEF), Sarov, Russia*
[107]*Saha Institute of Nuclear Physics, Homi Bhabha National Institute, Kolkata, India*
[108]*School of Physics and Astronomy, University of Birmingham, Birmingham, United Kingdom*
[109]*Sección Física, Departamento de Ciencias, Pontificia Universidad Católica del Perú, Lima, Peru*
[110]*Shanghai Institute of Applied Physics, Shanghai, China*
[111]*St. Petersburg State University, St. Petersburg, Russia*
[112]*Stefan Meyer Institut für Subatomare Physik (SMI), Vienna, Austria*
[113]*SUBATECH, IMT Atlantique, Université de Nantes, CNRS-IN2P3, Nantes, France*
[114]*Suranaree University of Technology, Nakhon Ratchasima, Thailand*
[115]*Technical University of Košice, Košice, Slovakia*
[116]*Technische Universität München, Excellence Cluster 'Universe', Munich, Germany*
[117]*The Henryk Niewodniczanski Institute of Nuclear Physics, Polish Academy of Sciences, Cracow, Poland*
[118]*The University of Texas at Austin, Austin, Texas, USA*
[119]*Universidad Autónoma de Sinaloa, Culiacán, Mexico*
[120]*Universidade de São Paulo (USP), São Paulo, Brazil*
[121]*Universidade Estadual de Campinas (UNICAMP), Campinas, Brazil*
[122]*Universidade Federal do ABC, Santo Andre, Brazil*

[123] *University College of Southeast Norway, Tonsberg, Norway*
[124] *University of Cape Town, Cape Town, South Africa*
[125] *University of Houston, Houston, Texas, USA*
[126] *University of Jyväskylä, Jyväskylä, Finland*
[127] *University of Liverpool, Liverpool, United Kingdom*
[128] *University of Tennessee, Knoxville, Tennessee, USA*
[129] *University of the Witwatersrand, Johannesburg, South Africa*
[130] *University of Tokyo, Tokyo, Japan*
[131] *University of Tsukuba, Tsukuba, Japan*
[132] *Université Clermont Auvergne, CNRS/IN2P3, LPC, Clermont-Ferrand, France*
[133] *Université de Lyon, Université Lyon 1, CNRS/IN2P3, IPN-Lyon, Villeurbanne, Lyon, France*
[134] *Université de Strasbourg, CNRS, IPHC UMR 7178, F-67000 Strasbourg, France, Strasbourg, France*
[135] *Université Paris-Saclay Centre dÉtudes de Saclay (CEA), IRFU, Department de Physique Nucléaire (DPhN), Saclay, France*
[136] *Università degli Studi di Foggia, Foggia, Italy*
[137] *Università degli Studi di Pavia, Pavia, Italy*
[138] *Università di Brescia, Brescia, Italy*
[139] *Variable Energy Cyclotron Centre, Homi Bhabha National Institute, Kolkata, India*
[140] *Warsaw University of Technology, Warsaw, Poland*
[141] *Wayne State University, Detroit, Michigan, USA*
[142] *Westfälische Wilhelms-Universität Münster, Institut für Kernphysik, Münster, Germany*
[143] *Wigner Research Centre for Physics, Hungarian Academy of Sciences, Budapest, Hungary*
[144] *Yale University, New Haven, Connecticut, USA*
[145] *Yonsei University, Seoul, Republic of Korea*

[a]Deceased.
[b]Dipartimento DET del Politecnico di Torino, Turin, Italy.
[c]M.V. Lomonosov Moscow State University, D.V. Skobeltsyn Institute of Nuclear, Physics, Moscow, Russia.
[d]Department of Applied Physics, Aligarh Muslim University, Aligarh, India.
[e]Institute of Theoretical Physics, University of Wroclaw, Poland.